DEVELOPMENT AND EXPERIMENTAL VERIFICATION OF DAMPING ENHANCEMENT METHODOLOGIES FOR SPACE STRUCTURES

by

NESBITT WARD HAGOOD IV

B.S., Massachusetts Institute of Technology
(1985)

SUBMITTED IN PARTIAL FULFILLMENT OF
THE REQUIREMENTS FOR THE DEGREE OF

MASTER OF SCIENCE
IN AERONAUTICS AND ASTRONAUTICS

at the

MASSACHUSETTS INSTITUTE OF TECHNOLOGY

September 1988

Signature of Author ____ _____
Department of Aeronautics and Astronautics
August 12, 1988

Certified by _____
Professor Edward F. Crawley
Thesis Supervisor

Accepted by _____
Professor Harold Y. Wachman
Chairman, Departmental Graduate Committee

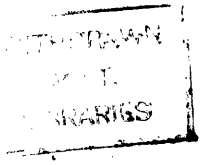

DEVELOPMENT AND EXPERIMENTAL VERIFICATION OF DAMPING ENHANCEMENT METHODOLOGIES FOR SPACE STRUCTURES

by

NESBITT WARD HAGOOD IV

Submitted to the Department of Aeronautics and Astronautics on
August 12, 1988
in partial fulfillment of the requirements for the
Degree of Master of Science in Aeronautics and Astronautics

ABSTRACT

A frequency domain system modelling technique is developed for mechanical systems. The technique is derived from Tellegen's Theorem for electrical networks and is applied to discrete mechanical systems. The elements are modelled in terms of their mechanical impedances. A global system model is assembled from the constitutive impedances. The global system model is used to determine the model exact pole locations and system energy dissipation and storage properties. An approximate method for finding modal frequencies and loss factors using the system impedance matrix and assumed modeshapes is developed. This method reduces to Rayleigh's Quotient in the case of an undamped system.

Impedance models for several damping enhancement mechanisms are presented. Among these are models for viscoelastic materials, the classical proof mass damper, and a new damping enhancement concept called the shunted piezoelectric. The shunted piezoelectric damping mechanism is based on a piezoelectric material which has its electroded surfaces shunted by an arbitrary electrical circuit. Methods are developed for analyzing this special damper and optimizing its damping properties in the case of shunting by a resister or by a resonant circuit. Parallels are drawn between the resistive shunted piezoelectric and viscoelastic materials and between the resonant shunted piezoelectric and the classical proof mass damper.

Experiments were conducted on a 5 meter, 10 bay box truss with a quasi free-free 3 dimensional suspension. A tunable, linear electromechanical driver was implemented for use as a proof mass damper. Electrical feedback of the proof mass position and velocity enabled accurate tuning of the dampers resonant frequency and internal damping. Piezoelectric truss members were designed and constructed for implementation of the shunted piezoelectric damping concepts. These members could replace the standard aluminum

truss members. In the resonant shunted piezoelectric experiments the tuning of the piezoelectrics was accomplished by creation of an "active" variable inductor.

Experiments were conducted to test truss structure dynamics and the damping enhancement concepts. These tests were compared to the analytical results obtained from the frequency domain system modelling technique. The proof mass damper implementation was found to increase system damping from 0.6% of critical to 6.4% of critical with a system mass increase of 2.7%. The resonant shunted piezoelectric increase system damping to 6.0% with a similar mass penalty. These resonant dampers were found to have negligible effect on the system modes other than the mode to which they were tuned. The analytical model was found to be capable of predicting the global system damping with these two concepts.

Thesis Supervisor: Dr. Edward Crawley

Title: Associate Professor of Aeronautics and Astronautics

Acknowledgements

I would like to thank my advisor, Professor Edward Crawley, for giving me the opportunity to conduct this research and for his guidance and time along the way. I would also like to thank Professor Andreas von Flotow for his support, advice, and humor when nothing seemed to work.

I owe much of the substance of this report to the graduate students in the Facility for Experimental Structural Dynamics with whom I spent countless hours hacking out sticky problems or escaping from them. I am also in debt to the undergraduate assistants who helped me build my Monument to Engineering.

Finally, it is with love that I dedicate this work to my wife, Meredith, whose unwavering support and sacrifice enabled its completion.

Nesbitt W. Hagood
August 12, 1988

Table of Contents

Nomenclature

a	=	number of independent forces
b	=	number of system branches
$\vec{B}_{PMD}$	=	magnetic field in gap of proof mass damper (Tesla)
C	=	generic damper or capacitance
C_{eq}	=	equivalent viscous damper for PMD
C_p	=	inherent capacitance of the piezoelectric
E	=	Young's modulus of material
E_{dis}	=	energy dissipated in a cycle
E_{oc}	=	open circuit modulus of the piezoelectric material
E_{sc}	=	short circuit modulus of the piezoelectric material
F	=	generic force
F_c	=	force through the mechanical side of the piezoelectric transformer
F_e	=	vector of elemental forces
F_p	=	vector of port forces
F_G	=	vector of global point forces
$F_{G\text{-}P}$	=	vector of global port point forces
$F_{G\text{-}NL}$	=	vector of global point forces due to nonlinear elements
F_α	=	vector of branch forces
F_β	=	vector of independent branch forces
g	=	real nondimensional frequency ratio = ω/ω_n
g_{31}	=	piezoelectric stress constant = strain /charge per unit area
I	=	current
I_e	=	current flowing through the electrical side of the piezoelectric transformer
K	=	generic stiffness
k_{31}	=	material electromechanical coupling coefficient
K_{31}	=	Generalized Electromechanical Coupling Coefficient (GECC)
L	=	piezoelectric bar length
L	=	system Lagrangian (T - U) or shunting inductance
M	=	generic mass
n	=	equivalent turns ration of piezoelectric transformer

n_t = number of system nodes

P = real power

$\bar{P}$ = average power dissipation over a cycle

q_e = charge on the piezoelectric's electrodes

r = resonant damper dissipation tuning parameter (has units of η)

R = shunting resistance

s = number of independent networks or Laplace parameter

t = time

T = piezoelectric bar thickness

T = system kinetic energy or period

$\mathbf{T}$ = transformation matrix from elemental to global coordinates = $[T_P\ T_L\ T_{NL}]^T$

U = system potential energy

v = velocity

v_c = velocity across equivalent piezoelectric transformer

$\mathbf{v}_e$ = vector of elemental velocities

$\mathbf{v}_G$ = vector of global point velocities

v_p = velocity across the piezoelectric

$\mathbf{v}_p$ = vector of port velocities

$\mathbf{v}_\alpha$ = vector of branch velocities

V = voltage

V_e = voltage across the equivalent piezoelectric transformer

w = piezoelectric bar width

X = reactive power

$\mathbf{x}_G$ = vector of global point positions

x_{st} = static displacement of a system = F/K

Z = generic impedance, mechanical or electrical

Z_{eff} = effective mechanical impedance of the shunted piezoelectric

Z_{elec} = electrical impedance of the piezoelectric transformer consisting of the shunting impedance parallel to the inherent capacitance

$\mathbf{Z}_G$ = global impedance matrix

$Z^{sc}_{mech}(s)$ = short circuit mechanical impedance of the piezoelectric

α_m, β_n = viscoelastic material parameters

β = mass ratio, proof mass/system mass

$\beta_{\alpha\beta}$ = Loop Matrix

γ = complex nondimensional frequency = s/ω_n

δ = resonant damper frequency tuning parameter = ω_d/ω_n

ε = strain

ζ = damping ratio

η = loss factor

η_{eff} = effective equivalent loss factor for PMD

Λ^F = force operator

Λ^v = velocity operator

ρ = nondimensional resistance (or frequency) = $RC_p\omega$

σ = stress = Force/Area

ω = frequency (radians/sec)

ω_n = natural frequency

Subscript

C = viscous damper

CO = conservative

d = part of a resonant damper

e,E = element

elec = electrical

G = global

I = imaginary

IN = inertial

K = stiffness

L = linear

M = mass

mech = mechanical

NC = non-conservative

NL = non-linear

opt = optimal

p,P = port or piezoelectric

PP = optimal by pole placement criteria

R = real

TF = optimal by transfer function criteria

visc = viscoelastic

α = branch

β = independent branch force

Superscript

^{H}	=	Hermetian
^{oc}	=	open circuit quantity
^{sc}	=	short circuit quantity
^{T}	=	transpose
$\mathbf{A}^{ij}$	=	element in the i^{th} row and j^{th} column of matrix, A
*	=	complex conjugate
$^{\sim}$	=	Laplace transformed quantity

Operations

Imag{ }	=	take the imaginary part of a complex quantity
Real{ }	=	take the real part of a complex quantity
$\|\mathbf{A}\|$	=	determinant of matrix A
$\delta( )$	=	variational

Chapter 1
Introduction

The design of future space structures poses some interesting problems for the structural dynamicist. The structures must be lightweight yet stiff. The most common structural form envisioned is typically a lattice truss structure in its various manifestations. This type of structure is central to designs such as the proposed NASA space station or polar orbiting earth observation platforms. Most designs for large or precision space structures entail some variation of a trusswork skeleton linking the vital system components. For applications involving antenna or observation equipment pointing, it is important for this skeleton to provide a solid support for the critical surface or device. Structural vibration can add noise to the sensitive systems causing intolerable performance reduction.

The structures themselves are inherently susceptible to vibration because of their light weight and extent. Structural mass conservation produces a flexible structure which is typically very lightly damped due to its isolation from any external contact. This combination of flexibility and light damping contribute greatly to a vibration problem for space structures.

As a solution to this vibration problem and in an attempt to control the shape of a structure in the presence of external disturbances, the engineering discipline of structural control has arisen. Active control of a structure can be designed to compensate for the inherently vibratory dynamics to allow achievement of attitude changes or other performance goals while minimizing structural system vibration.

Difficulty arises in the control of space structures due to their densely spaced undamped modal nature. These difficulties center around the interaction between the resonant modes and the control system. Potentially some of these flexible modes fall within the bandwidth of the control system. These must be included in the model of the dynamics of the controlled structure. Since the actual system modes are rarely in complete agreement with the model even these modelled modes pose some threat to the stability of the closed loop system. In addition to this robustness consideration, lightly damped modes can exist in the rolloff region of the control system. These modes are not included in the model but are subject to control authority

which has not yet rolled off. The rolloff modes pose another threat of instability to the control designer. As a partial solution to these two control problems, structural passive damping is important to the control designer both in the accurate modelling of the structure and in the stability of unmodelled modes.

The need for passive damping in space structures is presented in numerous sources such as Ashley [1] or Sarver [2]. Passive damping of the structural system can lead to great benefits for the control design and stability of the closed loop system. It tends to displace the structural poles towards the left in the typical s-plane representation giving more margin for displacement toward the right hand plane stability boundary. This pole movement is illustrated in Figure 1.1. This "extra room" gives the passively damped system more robustness to modelling error in the control system and helps alleviate the problems associated with structural modes in the rolloff region of the controller.

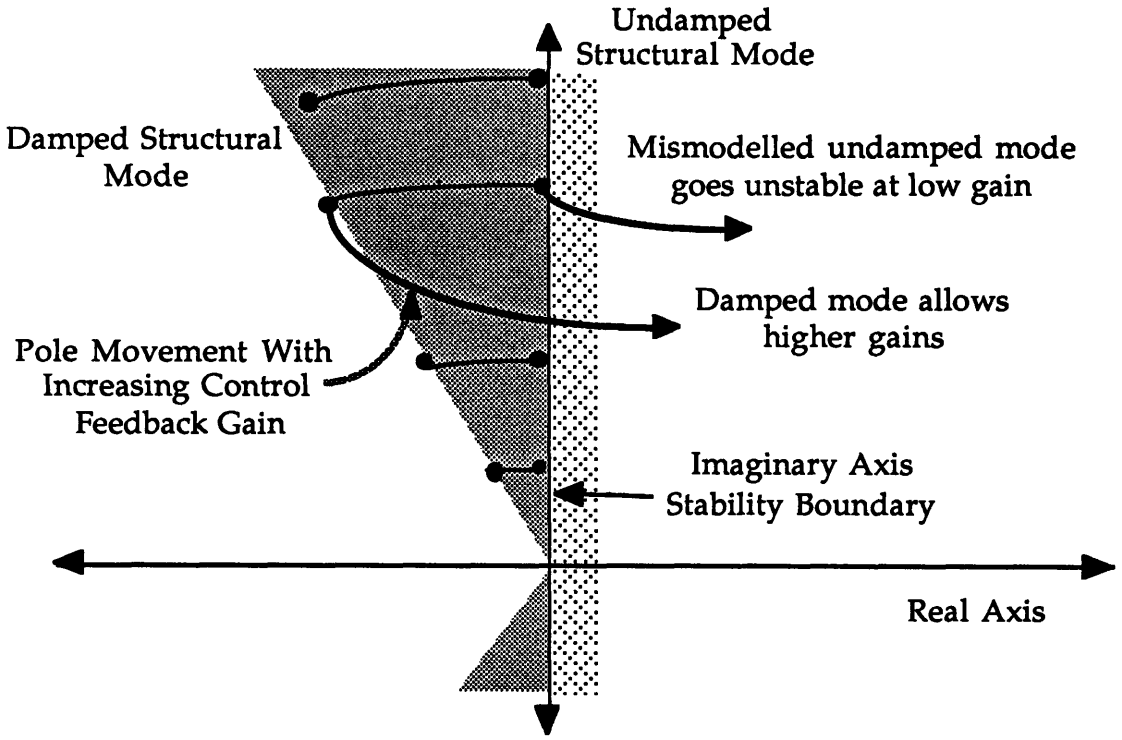

Figure 1.1 The Effect of Feedback on Both Lightly and Heavily Damped Mismodelled System Poles Showing the Increased Gain Margin Offered by Passive Damping.

There are several sources of passive damping on space structures. The most prevalent is material damping by which structural strain energy is dissipated. Damping is also inherent in the friction and impacting which occur in the structural joints. The structural and material damping is typically very small.

The inherent damping in a truss can be increased by using damping enhancement schemes. These typically involve the the addition of damping materials or devices to the structure. In this report, several methods of damping enhancement will be examined. They will then be implemented on a lightly damped truss structure. Those damping schemes that will be examined most closely involve the use of resonant subsystems, both mechanical, as in the proof mass damper, and electrical, as in the resonant shunted piezoelectric. These concepts will then be implemented on a realistic structure, and their effectiveness rated.

1.1 Motivation

The impetus of this report stems from a number of factors. Of primary concern is the necessity for increasing structural damping for automatic control systems. Congruent to this is the need to effectively model system passive damping in a framework suitable for control design or system trades. In light of this need, there has until now been little formalism in the design of damping enhancement for structures. Passive damping design has for the most part been an empirical "black art" with the design and assessment resting heavily on structural testing and iterative techniques. Since accurate 1-G ground vibration testing is difficult for space structures as noted by Sigler [3], an accurate design methodology using component information must be developed.

The tight performance criteria which drive the design of space structures has led to more complex system trade studies between system components. The current disarray in damping enhancement analysis makes it difficult to evaluate the relative effectiveness of a damping mechanism in relation to other potential damping candidates. To effectively preform the design trades, all the damping mechanisms must be expressed in the same analysis/modelling framework.

Several damping techniques are applicable to space structures. Some viscoelastic techniques have been developed for trusses in Reference [4]. An implementation of the proof mass damper technique on a model space structure can be found in Crawley and Miller's Ref. [5]. This report will attempt to unify these methods within a single modelling framework.

1.2 Objective

The intention of this report is to provide a systematic methodology for the analysis of damped structures. It is intended to give the damping designer increased flexibility by providing the analytical tools necesarry to quickly evaluate the preformance of competing damping mechanisms in structures. The investigation is also designed to provide experimental verification of some promising damping enhancement mechanisms for structures. The experiments were designed to provide data on the realistic application of both conventional and non-conventional dampers. As a consequence, some useful information on the practical aspects pertaining to system trades with the various damping schemes is presented in the following chapters.

1.3 Background

In order to develop a framework for the analysis of damped structures which was sufficiently general to embrace the sundry damping devices, it was necessary to parallel techniques used in the analysis of dissipative electrical circuits. The core of this report is drawn from research conducted on electrical circuit analysis. It will be shown that the theory for power flow in electrical networks, known as Tellegen's Theorem, can be applied to structural systems as well. This theory is presented in Reference [6] along with associated theories on network sensitivities. The design of electrical networks with resisters or nonlinear capacitors can be paralleled with the design of structural systems with dampers and nonlinear elements. The design of highly damped systems is not unusual for the electrical designer and it is useful to draw on experience gained in this field. The key to the usefulness of the electrical techniques lies in the parallel between mechanical

and electrical systems which has been expressed in such discussions of systems analysis as Ref. [7] and Ref. [8]. In these parallels, force is compared to current, and velocity compared to voltage. This comparison preserves both the dynamic nature and connective topology of the systems. With these definitions a vast array of research on complex systems analysis opens to the structural designer.

The frequency domain method used for modelling damped systems in this report is rooted in the parallels of electrical circuit impedance and structural impedance. The use of complex electrical impedances greatly simplifies the determination of steady state performance for electrical systems. The use of structural impedance can give the same result for determining the performance and response of complex damped structural systems. The structural impedance is the frequency dependant relationship between an applied force and the resulting response at a point. It relies on the Laplace or Fourier transform to create a compact frequency dependant expression of system properties such as the stiffness or mass of a structural element. Structural impedance is a well known concept to the dynamicist, it being widely employed in complex system design in the 1950 and 1960, Ref. [8]. The intent of this report is to exploit the parallels between electrical impedance and electrical network analysis and mechanical impedance and network analysis to provide a systematic method of analysis for damped structural systems.

1.4 Approach

In this report, a frequency domain approach to damped structural system design will be presented. First, the frequency domain results for electrical systems will be generalized to discrete mechanical systems. The frequency domain relations will be examined to determine some simple approximate methods to quickly determine the effect of a damping mechanism on a system by virtue of its impedance. To complement this, several damper impedances will be derived. A set of experiments were conducted to test this frequency domain modelling scheme and also to test the relative merits of the various damping mechanisms.

Chapter 2 is devoted to the development of frequency domain modelling of damped structural systems based on Tellegen's Theorem. First the framework for a structural network is introduced along with the concept of structural impedance. Approximate expressions are developed to enable the designer to easily evaluate the effectiveness of damping schemes. Finally, an example of the frequency domain modelling technique is examined.

Chapter 3 presents the frequency domain impedances of various key damping systems. Of particular import are the derivations done for the optimum tuning of resonant damping devices in both their physical (proof mass dampers) and electrical (resonant shunted piezoelectrics) manifestations. The models of arbitrarily shunted piezoelectrics are developed and applied to maximizing structural damping. Of particular importance is a model for the effective impedance of a piezoelectric material linked to an electrical "shunting" circuit. This piezoelectric element can be applied to damping enhancement if the shunting circuit is appropriately chosen.

Chapter 4 outlines the main design challenges of the experiment. In it are presented the three major design projects involved with the experiments. The first project entailed the design of the experimental testbed for the damping experiments. This testbed was a freely suspended truss structure. The second project involved the implementations of the damping devices under investigation. These devices where a linear proof mass damper/actuator and a piezoelectric truss member. Finally, the electrical support circuitry which allowed efficient and easy tuning of the dampers is described.

Chapter 5 presents the results of the experimental investigation. The experimental results for the dynamics of truss structures with various damping mechanisms are presented and compared to the analytical results obtained from the frequency domain modelling. Some interesting work in the sensitivities of these resonant dampers is presented showing the effect of parameter variation on the total system damping levels. This can be useful in determining the effects of mismodelling on the expected truss response. The conclusions concerning the effectiveness of the frequency domain modelling technique for damped structures are presented in this chapter.

Chapter 2
Frequency Domain Analysis of Mechanical Systems

2.1 Overview

In this chapter the fundamental relations involved with frequency domain modelling and analysis of structural systems will be presented, and the tools used in subsequent chapters developed. The structural system will be modelled as a discretized network of elements obeying force equilibrium and displacement compatibility. All networks obeying these constraints exhibit certain properties that can be exploited in system analysis. One such property is a form of energy conservation throughout the network, an expression of which is known as Tellegen's Theorem.

Tellegen's Theorem has been widely used for analysis of electrical networks and here will be applied to mechanical networks. It relates the energy flowing into a system to the energy flow within the system elements. The frequency domain expression of Tellegen's Theorem is then coupled with the traditional concept of structural impedance to derive an impedance energy expression. In order to relate it to the conventional formulation for mechanical system dynamics, this impedance energy expression will be used to derive Hamilton's Theorem for dynamic systems. It will also be used to derive expressions for system resonant frequencies and damping. Finally, the sensitivity of system dynamic characteristics to variations in key system parameters will be evaluated. These tools will be used for analysis and design of complex damped systems in subsequent chapters of this report.

2.2 Structural Networks and Tellegen's Theorem

2.2.1 Definitions of Branches, Elements, and Ports

Any mechanical system can be modelled with varying degrees of accuracy as a network of discrete elements. A network is defined to be a collection of interconnecting branches which join at discrete nodes. The branches are the components of the system and can represent a wide variety

of mechanical, electrical, or thermal devices. In this chapter only mechanical networks will be dealt with, although the equations can be easily generalized to other types of system elements. A node is merely a reference point that serves as a junction between branches of the network.

The branches will be divided into two groups which are called elements and ports. The elements are the physical pieces of the system. The ports are the branches through which external forces and displacements can be imposed on the system. These concepts can be demonstrated with a simple structural system in Figure 2.1:

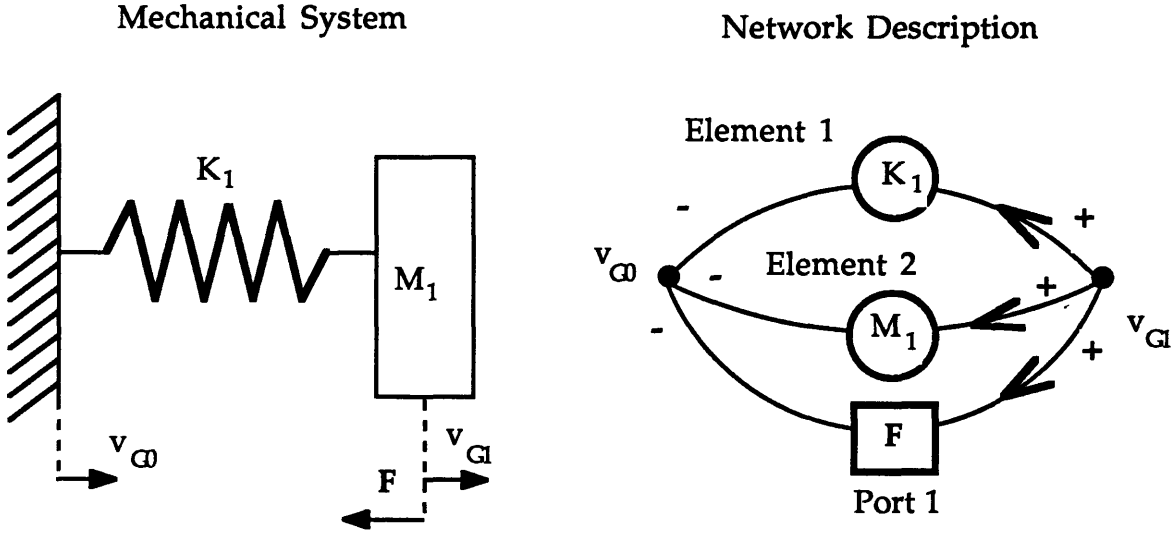

Figure 2.1 Network Description of a Simple Mechanical System

This single degree of freedom (DOF) system can be modelled as having 2 nodes, and 3 branches. The 3 branches are composed of 2 elements and 1 port. It is important to note that the structural mass element has been modeled as an element between the moving node, v_{G1}, and the ground node, v_{G0}. All masses are modelled as elements to the ground node. This is due to the dependence of inertial force on the absolute acceleration of the mass.

The two structural members, the mass and the spring can be thought of as two branches of a network between the moving node, v_{G1}, and the fixed node, v_{G0}. The applied force is represented by another branch through which an external force acts between the nodes. It is said that the system has a port through which F acts.

In such generalized networks, every branch has two attributes known as the *through* and *across* variables of the branch. In mechanical systems these are the force that acts *through* the branch and the velocity that exists *across* the branch. Thus, in mechanical systems, force is the *through* variable and velocity is the *across* variable. The sign conventions are such that the product of the force and velocity in an element is positive when work is being done on the element. The positive velocity across the element is usually associated with an increase in some physical dimension of the element but can be an arbitrary assignment. The positive force assignment is made in accordance with the power flow convention and the velocity assignment. For ports the power flow convention will for now be taken as for elements. This means that the product of force and velocity is defined to be positive when work is being done on the port.

In electrical systems the *through* variable is commonly taken to be the current, and the *across* variable is taken to be the voltage. This establishes a correspondence between electrical and mechanical systems that can be stated:

Variable	Mechanical	Electrical
Through	Force	Current
Across	Velocity	Voltage

This convention is one of the two commonly used in comparing the behavior of electrical circuits and mechanical systems, the other being the comparison of force with voltage (the "effort" variables) and velocity with current (the "flow" variables) as in Paynter [9]. Purely from the perspective of comparing differential equations, both conventions are valid analogies. But as is shown in Fig. 2.2, the correspondence used here preserves both the dynamic behavior and the topology of the network, and is used in such general discussions of system dynamics as Penfield, Ref. [6], and Cannon, Ref. [7]. By choosing the through/across correspondence the rules for mechanical network reduction follows the same rules as those more widely known for electrical networks. This correspondence will be explained and exploited in a later sections.

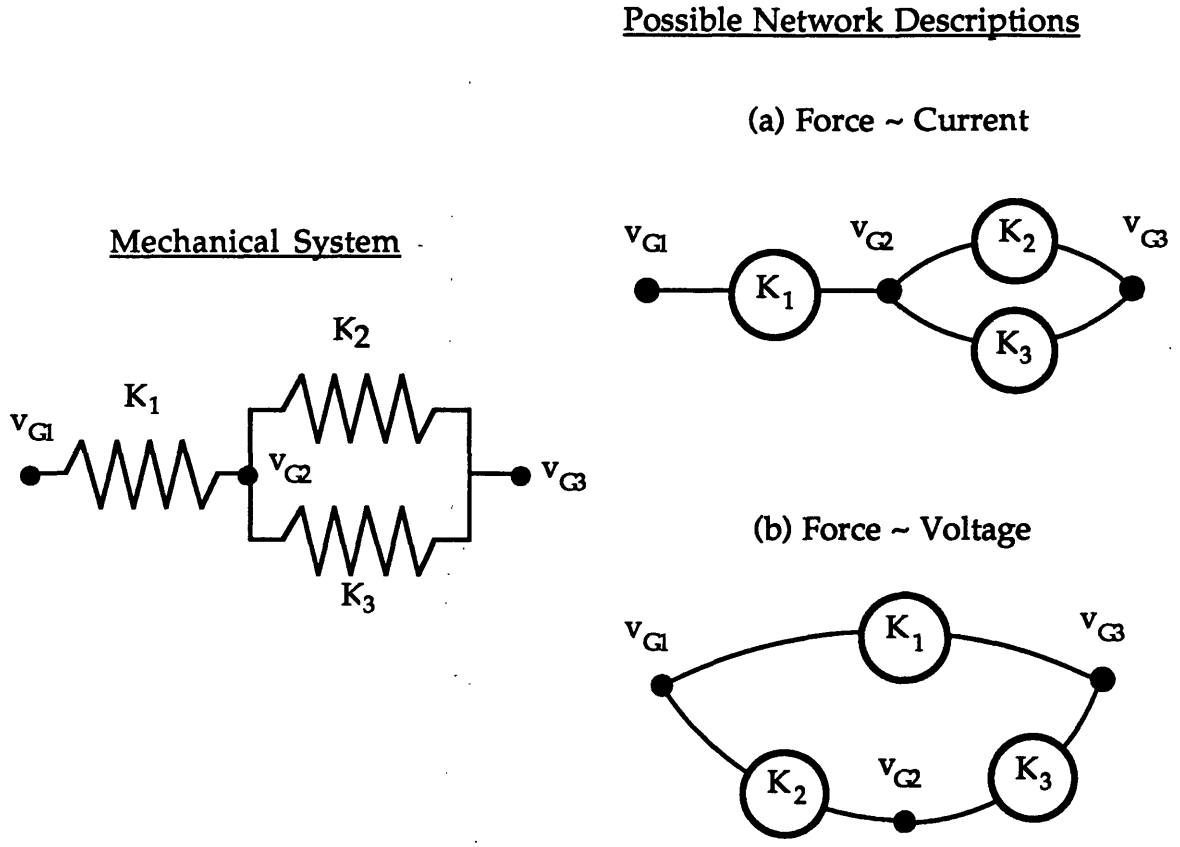

Figure 2.2 Possible Network Descriptions of a Simple Mechanical System Showing the Networks Which Result from Comparing Force to Current (a) or Voltage (b)

2.2.2 Force Equilibrium and Displacement Compatibility

There are constraint conditions that apply among the through and across variables. As demonstrated in Ref. [10], these constraints are known as force equilibrium at the nodes and displacement compatibility for the branches in mechanical systems. In electrical systems, they are known as Kirchoff's current and voltage laws respectively.

Force equilibrium is the statement that all the forces acting on a node must sum to zero. This is true because inertial reactions have been represented by D'Alembert forces acting through the mass elements. Force equilibrium corresponds to Kirchoff's current law in electrical systems, and the mathematical expressions of these constraints are identical. For

mechanical systems, force equilibrium can be expressed by defining the vector which contains the forces in all the branches (elements and ports) known as the Branch Force Vector, $\mathbf{F}_\alpha$, in terms of a set of independent forces in the Independent Force Vector, $\mathbf{F}_\beta$.

$$\mathbf{F}_\alpha = \mathbf{B}_{\alpha\beta}\mathbf{F}_\beta \tag{2.1}$$

Where $\mathbf{F}_\alpha$ is the Branch Force Vector, and $\mathbf{F}_\beta$ is the Independent Force Vector. The matrix, $\mathbf{B}_{\alpha\beta}$, called the loop matrix in electrical circuit analysis, defines the relationship between the independent and dependent forces. The independent force vector can be composed of any group of port or element forces which are not linearly related.

The number of independent forces can be found from network analysis (Ref. [6]) to be:

$$a = b - n_t + s \tag{2.2}$$

where a is the number of independent forces, b is the number of system branches (elements and ports), n_t is the number of system nodes, and s is the number of separate networks. The loop matrix, **B**, has the dimensions b by a. The loop matrix is very useful in network analysis. An example of system analysis where the loop matrix is derived is shown in Section 2.8. As can be seen, it is directly attributable to the linear relationships which exist among any system with redundant load paths.

The second constraint on the network variables is velocity compatibility. In mechanical systems, it is the statement of the geometric constraints of the system: that all the branches connecting two nodes must have the same velocities across them. It's electrical analogy is Kirchoff's voltage law. Mathematically, velocity compatibility can be expressed:

$$\mathbf{B}^{T}_{\alpha\beta}\mathbf{v}_\alpha = \mathbf{0} \tag{2.3}$$

Where **B** is found to be the same loop matrix as was used in the statement of force equilibrium (Ref. [6]). These two expressions for force equilibrium and displacement compatibility, (2.1) and (2.3), can be combined to derive Tellegen's Theorem

2.2.3 Tellegen's Theorem

Tellegen's Theorem is a convenient expression for the force and velocity constraints on a system. Pre-multiplying equation (2.1) by $\mathbf{v}_\alpha^T$ we obtain:

$$\mathbf{v}_\alpha^T \mathbf{F}_\alpha = \mathbf{v}_\alpha^T \mathbf{B}_{\alpha\beta} \mathbf{F}_\beta \tag{2.4}$$

This can be simplified by noting that the right hand side of (2.4) is zero due to (2.3). This reduction gives the simplest form of Tellegen's theorem.

$$\mathbf{v}_\alpha^T \mathbf{F}_\alpha = 0 \tag{2.5}$$

Equation (2.5) represents a summation over all the network branches. The branches can be divided into elements and ports. The ports can be separated out to the right hand side of (2.5) leaving the summation over the elements on the left. The sign convention for the ports will also be changed so that now the product is positive if the port is doing work on the remainder of the system. This yields:

$$\mathbf{v}_e^T \mathbf{F}_e = \mathbf{v}_p^T \mathbf{F}_p \tag{2.6}$$

Where the subscript, e, represents the system elements; and the subscript, p, represents the system ports. This equation represents summations over the elements and ports of the system and relates the work done by the ports on the system to the work done on the elements within the system.

Equation (2.6) can be generalized by introducing linear operators to act on the forces and velocities. A justification for this generalization is presented in Ref. [6]. The linear operators acting on the forces must be the same for all the forces and the linear operators for the velocities must be likewise the same for the velocities though not necessarily the same as those for the forces. Some allowable operators are: integration, differentiation, multiplication by a constant, Fourier or Laplace transforms, and complex conjugation. By applying the linear operators to Equation (2.6) the general form of Tellegen's Theorem is obtained.

$$\Lambda^v \mathbf{v}_e^T \Lambda^F \mathbf{F}_e = \Lambda^v \mathbf{v}_p^T \Lambda^F \mathbf{F}_p \tag{2.7}$$

This equation exhibits several properties useful for the analysis of systems obeying the force and velocity constraints. The first property is a result of the fact that nowhere in the derivation of the equation was it assumed that the forces and velocities belong to the same load case. Thus

forces and velocities from unrelated applications can be used to satisfy Equation (2.7). The consistent elemental forces from some arbitrary loading case can be combined with the consistent velocities from some unrelated loading. When that unrelated load is applied at a node where the velocity resulting from a complex loading are desired, this technique becomes the dummy load method of elementary structural analysis as presented in Ref. [10]. Being able to use unrelated cases can simplify the analysis of a system greatly.

Another property arises from the fact that none of the constitutive properties of the elements have been included in Equation (2.7). The only required common point between the loading and velocity cases is that they are from networks with the same topology and therefore have the same loop matrix. Tellegen's Theorem is based on network properties and is independent of the type of elements which make up that network. The actual makeup of the network from which the consistent forces are taken and the network from which the compatible velocities are taken need not be similar. Dampers in the network to which the forces belong can be replaced by springs in the network to which the velocities belong. Nonlinear elements can be replaced by linear ones and Equation (2.7) will still hold. This property opens options for system analysis and has been applied fruitfully to electrical systems.

Since the constitutive relations for the elements were not used in the derivation, Tellegen's Theorem is valid for arbitrary systems including structures with time varying, non-linear, and frequency dependent elements. In fact it is frequently used to analyze electrical systems with nonlinear capacitors or transistors as elements. For these systems it can be used to establish bounds on the energy that is transferred to higher harmonics by nonlinear elements (Ref. [11]). In this report, advantage will be taken of this property to model and analyze the energy dissipation characteristics of systems with frequency dependent elements or subsystems.

Specializing the general statement of Tellegen's Theorem, Equation (2.7), by using the Laplace operator on the forces and velocities, a frequency domain expression for Tellegen's Theorem can be obtained. Letting Λ^V select the complex conjugate of the Laplace transform and Λ^F select only the Laplace transform, Equation (2.7) becomes:

$$\tilde{\mathbf{v}}_e^H(s)\tilde{\mathbf{F}}_e(s) = \tilde{\mathbf{v}}_p^H(s)\tilde{\mathbf{F}}_p(s) \tag{2.8}$$

Where the tilde, ~, represents the Laplace transformed variable. From this point forward all forces and velocities will be in the frequency domain and the tilde will be omitted for simplicity.

If we consider the system to be operating in sinusoidal steady state ($s = i\omega$), then the Laplace transform can be thought of as the Fourier coefficients representing the amplitude and phase of the sinusoidal signal. Throughout the rest of the report, the Laplace transformed variables will be used. The explicit dependence on the Laplace variable, s, may be omitted for simplicity but the frequency dependence will be implicit.

2.3 Structural Impedance and System Modelling

At this point the relationships for the topology, ie. displacement compatibility and force equilibrium, have been expressed by Tellegen's Theorem; and it is desirable to introduce the constitutive relations for the individual elements. Since Tellegen's Theorem will be employed in the frequency domain, the constitutive relations will be introduced by using the frequency dependent ratio of the velocity and force to eliminate the elemental forces from Equation (2.8). The equations will then be converted from elemental to global coordinates to give the system equations in their final form.

In a mechanical system various names are given for the ratio between the force in a system and various output variables. These names from have been compiled by Ewins [12] and presented in Table (2.1). In this report, the concept of mechanical impedance will be utilized for system modelling and analysis since it relates the force and velocity in a system element. It is expressed as the ratio of the Laplace transformed force over the Laplace transformed velocity. For nonlinear systems, it may be amplitude dependent. The mechanical impedance for a mass, spring, and damper are:

$$Z_M(s) = M\,s \tag{2.9a}$$

$$Z_C(s) = C \tag{2.9b}$$

Response Parameter R	R / F	F / R
Displacement	Receptance, Admittance, Compliance	Dynamic Stiffness
Velocity	Mobility	Mechanical Impedance
Acceleration	Inertance, Accelerance	Apparent Mass

Table 2.1 Possible Frequency Domain Constitutive Properties

$$Z_K(s) = \frac{K}{s} \tag{2.9c}$$

The impedance can be a more complicated function of frequency as in the case with elements with resonant subsystems or viscoelastic behavior. For general elements with connections to more than 2 system nodes the concept of a impedance matrix can be used to relate the forces and velocities associated with the element. Thus in general for the linear elements, the constitutive relations can be written

$$\mathbf{F}_L(s) = \mathbf{Z}_L(s)\, \mathbf{v}_L(s) \tag{2.10}$$

where $\mathbf{F}_L$ is the vector of linear elemental forces, $\mathbf{v}_L$ is the vector of linear elemental velocities and $\mathbf{Z}_L$ is the linear elemental impedance matrix.

The elemental impedances can be substituted into equation (2.8) to eliminate the explicit reference to the forces of the linear elements.

$$\mathbf{v}_L^H\, \mathbf{Z}_L \mathbf{v}_L + \mathbf{v}_{NL}^H \mathbf{F}_{NL} = \mathbf{v}_P^H \mathbf{F}_P \tag{2.11}$$

A few moments should be taken to examine the structure of Equation (2.11). The system described above will be defined to have b branches where b is the sum of the number of linear elements, n, the number of nonlinear elements, m, and the number of ports, k. The first term on the left is a summation over the linear elements of the systems. For a system with n linear elements, it can be represented

$$\begin{bmatrix} v_{L1} & v_{L2} & \cdots & v_{Ln} \end{bmatrix}^* \begin{bmatrix} Z_{L1} & 0 & \cdots & 0 \\ 0 & Z_{L2} & & \vdots \\ \vdots & & \ddots & \vdots \\ 0 & \cdots & & Z_{Ln} \end{bmatrix} \begin{bmatrix} v_{L1} \\ v_{L2} \\ \vdots \\ v_{Ln} \end{bmatrix} = \mathbf{v}_L^H \mathbf{Z}_L \mathbf{v}_L \qquad (2.12)$$

Where the superscript, *, represents the complex conjugation. The elemental impedance matrix is diagonal; and, when pre and post multiplied by the elemental velocities, it represents a summation over the linear elements of the system. The second term of (2.11) can be represented as a summation over m non-linear elements

$$\begin{bmatrix} v_{NL1} & v_{NL2} & \cdots & v_{NLm} \end{bmatrix}^* \begin{bmatrix} F_{NL1} \\ F_{NL2} \\ \vdots \\ F_{NLm} \end{bmatrix} = \mathbf{v}_{NL}^H \mathbf{F}_{NL} \qquad (2.13)$$

Likewise the third term can be represented as a summation over k system ports

$$\begin{bmatrix} v_{p1} & v_{p2} & \cdots & v_{pk} \end{bmatrix}^* \begin{bmatrix} F_{p1} \\ F_{p2} \\ \vdots \\ F_{pk} \end{bmatrix} = \mathbf{v}_p^H \mathbf{F}_p \qquad (2.14)$$

These summations can be condensed and simplified if it is noted that the elemental velocities, the relative velocities across the elements, can be represented as linear combinations of the absolute velocities of the system nodes relative to inertial space. The velocities at the nodes will be called the global velocities which exist in the inertial frame in the global coordinate system of the nodes. Fist a transformation between the global "point" velocities and the elemental "across" velocities must be defined. The velocity across the element can be thought of as the difference between the velocities of the nodes of that element after an appropriate coordinate rotation. Thus a transformation matrix can be defined:

$$\begin{bmatrix} \mathbf{v}_P \\ \mathbf{v}_L \\ \mathbf{v}_{NL} \end{bmatrix} = \begin{bmatrix} \mathbf{T}_P \\ \mathbf{T}_L \\ \mathbf{T}_{NL} \end{bmatrix} \mathbf{v}_G = \mathbf{T}\mathbf{v}_G \tag{2.15}$$

where $\mathbf{v}_G$ is the vector of absolute nodal velocities and $\mathbf{v}_P$, $\mathbf{v}_L$ and $\mathbf{v}_{NL}$ have been previously defined. The various partitions of the transformation matrix, T, can be used to convert the elemental forces and impedances of Equation (2.11) into more easily conceptualized point forces and impedances. Substituting the appropriate partitions of (2.15) into (2.11) gives us Tellegen's Theorem in terms of point quantities

$$\mathbf{v}_G^H \mathbf{Z}_{G\text{-}L} \mathbf{v}_G + \mathbf{v}_G^H \mathbf{F}_{G\text{-}NL} = \mathbf{v}_G^H \mathbf{F}_{G\text{-}P} \tag{2.16}$$

where:

$$\mathbf{F}_{G\text{-}P} = \mathbf{T}_P^T \mathbf{F}_P \tag{2.17a}$$

$$\mathbf{F}_{G\text{-}NL} = \mathbf{T}_{NL}^T \mathbf{F}_{NL} \tag{2.17b}$$

$$\mathbf{Z}_{G\text{-}L} = \mathbf{T}_L^T \mathbf{Z}_L \mathbf{T}_L \tag{2.17c}$$

Tellegen's Theorem is now in a form dependent only on the velocities of the nodes, the global impedance matrix, $\mathbf{Z}_{G\text{-}L}$, which contains the elemental constitutive relations in the global coordinate system, and the forces due to the ports and nonlinear elements. At this point either the driving forces or the nonlinear forces could also be eliminated by defining the appropriate port or non-linear impedance matrix. For the nonlinear elements, the forces can be described by state dependant impedances

$$\mathbf{F}_{G\text{-}NL} = \mathbf{Z}_{G\text{-}NL}(\mathbf{v}_G, s)\, \mathbf{v}_G \tag{2.18}$$

This nonlinear impedance can be used to replace the nonlinear forces in Equation (2.16) to obtain a global impedance matrix for the system.

$$\mathbf{v}_G^H \mathbf{Z}_G(\mathbf{v}_G, s)\, \mathbf{v}_G = \mathbf{v}_G^H \mathbf{F}_{G\text{-}P} \tag{2.19}$$

were:

$$\mathbf{Z}_G(\mathbf{v}_G, s) = \mathbf{Z}_{G\text{-}L}(s) + \mathbf{Z}_{G\text{-}NL}(\mathbf{v}_G, s) \tag{2.20}$$

The size of the resulting frequency domain system matrix might be quite large for a system with many degrees of freedom. There are, however, many techniques for reducing the sometimes cumbersome size of the global impedance matrix. The ones described here are drawn from techniques used for reduction of discrete time domain models. The first and probably most useful is the elimination of degrees of freedom with no external forcing at them by using static condensation on the global impedance matrix. Static condensation is usually employed in the reduction of system stiffness matrices and is customarily thought of as a quasi-static condensation for dynamic systems. If, however, the frequency dependant system impedance matrix is reduced using this method then the reduction is an exact dynamic reduction since the mass information is included in the impedances. The equations for the static condensation technique can be found in Ref. [13]. When the impedance matrix is reduced, a lower order but more complicated frequency dependent matrix is the result. This matrix contains all the information inherent to the larger model and the condensed information can be recaptured if necessary.

The second reduction method is the assumed mode technique. The global set of degrees of freedom is reduced to a smaller set of generalized coordinates by assuming a linear relation among the global set. An example of an application of this method is the assumption of rigid body motion for some set of the boundary nodes or a conversion to modal coordinates common in dynamics. This type of reduction is not guaranteed to be exact but can result in problem simplification. It usually does not greatly complicate the frequency dependence of the impedance matrix. These two techniques can be used to great advantage in complex system reduction and analysis.

2.4 Comparison of Tellegen's and Hamilton's Theorems

A version of Hamilton's Theorem can be derived from Tellegen's Theorem for discrete systems. The derivation serves to highlight the relationship between the various power products in Tellegen's Theorem and the conventional kinetic and potential energies. The derivation will also help place Tellegen's Theorem on more familiar ground for system dynamicists. The key to the derivation lies in the proper choice of the linear

operators in the general form of Tellegen's Theorem. If we recall the form of the theorem presented in Equation (2.5):

$$\mathbf{v}_\alpha^T \mathbf{F}_\alpha = 0 \tag{2.21}$$

This form of Tellegen's Theorem has not yet been specialized to the frequency domain by use of the Laplace operator nor have the branches been separated into elements and ports by the sign convention. This form of Tellegen's Theorem represents a summation over all the branches of a system.

The coordinate system of Equation (2.21) can be transformed from elemental to global using the transformation technique outlined in the previous section for Equation (2.15). The equation can also be generalized just as was Equation (2.7) to allow operators on the forces and velocities. The result is a generalized product of the nodal forces and velocities of the system.

$$\Lambda^v \mathbf{v}_G^T \Lambda^F \mathbf{F}_G = 0 \tag{2.22}$$

Any linear (and some nonlinear) operator or sets of operators may be chosen as the Λ's of Equation (2.22) as is explained in the appendix of Ref. [6]. If Λ^v is defined as the variational of an integral with respect to time then Equation (2.22) becomes:

$$\delta \mathbf{x}_G^T \Lambda^F \mathbf{F}_G = 0 \tag{2.23}$$

Furthermore, taking the transpose of (2.23) and integrating from t_1 to t_2, a variational equation emerges:

$$\int_{t_1}^{t_2} \left[\mathbf{F}_G^T \delta \mathbf{x}_G \right] dt = 0 \tag{2.24}$$

At this point it is necessary to consider the makeup of the nodal forces. The global force vector, $\mathbf{F}_G$, represents at each degree of freedom the sum of the elemental forces (for elements such as masses or stiffnesses) as well as the externally applied forces at that particular degree of freedom. It is convenient to divide the global force vector into its component parts: the conservative forces such as spring forces or gravitation; the inertial forces due to the mass elements; and the non-conservative forces arising from energy dissipation elements and external forcing.

$$\int_{t_1}^{t_2}\left[\mathbf{F}_{IN}^{T}\,\delta\mathbf{x}_G + \mathbf{F}_{CO}^{T}\,\delta\mathbf{x}_G + \mathbf{F}_{NC}^{T}\delta\mathbf{x}_G\right]dt = 0 \tag{2.25}$$

Each of these groups of terms has a specific relationship to the energy in the system. The inertial forces relate to the kinetic energy and the conservative forces relate to the potential energy. To determine exactly how these terms relate to their respective energies, variational calculus must be employed. If we assume that the conservative force can be associated with a possibly time varying stiffness matrix and that the inertial force or D'Alembert force can be associated with a mass matrix, we can obtain:

$$\left[-\mathbf{K}_G(t)\,\mathbf{x}_G\right]^{T}\delta\mathbf{x}_G = -\frac{1}{2}\,\delta\left[\mathbf{x}_G^{T}\mathbf{K}_G(t)\,\mathbf{x}_G\right] = -\delta U \tag{2.26a}$$

$$\left[-\mathbf{M}_G(t)\ddot{\mathbf{x}}_G\right]^{T}\delta\mathbf{x}_G = \frac{1}{2}\,\delta\left[\dot{\mathbf{x}}_G^{T}\mathbf{M}_G(t)\dot{\mathbf{x}}_G\right] = \delta T \tag{2..26b}$$

Substituting these expressions into Equation (2.25) and separating out the non-conservative part gives us the well-known form of Hamilton's Principle:

$$\int_{t_1}^{t_2}\delta[T - U]\,dt + \int_{t_1}^{t_2}\left[\mathbf{F}_{NC}^{T}\delta\mathbf{x}_G\right]dt = 0 \tag{2.27}$$

Thus, a version of Hamilton's Principle for discreet dynamic systems can be derived from Tellegen's Theorem. The subtlety is in the choice of appropriate linear operators to be used in the general form of Tellegen's Theorem and in the recognition of the various contributions to the nodal forces.

Many other variation expressions for dynamic systems can be developed by starting with the general form of Tellegen's Theorem and using alternate linear operators. In this work, the Laplace transform was chosen, which has the effect of transforming the system equations into the frequency domain. The choice of the linear operator in no way affects the amount of information about the system that is contained in the equations. The frequency domain representation of dynamic systems thus contains the same fundamental information as the more common Hamilton's Principle and is equally valid for dynamic systems.

2.5 Conservation of Real and Reactive Power

In this section an attempt will be made to determine the nature of the energy expressions inherent in the frequency domain statement of Tellegen's Theorem. In Equation (2.8) both the force vector and the velocity vector for the elements and the ports have real and imaginary parts. The product of force and velocity is power. This product can also be divided into real and imaginary parts. The real part is termed the real power, and the imaginary part is termed the reactive power. Since the force/velocity product must be equal for the ports and the elements, Tellegen's Theorem in the frequency domain is sometimes referred to as the conservation of real and reactive power.

Power is a time domain quantity and is calculated from the time domain product of the instantaneous force and velocity. The terms of Equation (2.19) are frequency domain products. Strictly speaking, the Laplace transform of the time domain power would involve a convolution integral of the transformed force and velocity since time domain multiplication corresponds to frequency domain convolution. Therefore the product of the transformed force and velocity does not represent the Laplace transformed instantaneous power but rather some related quantity. The nature of this relationship will be examined in the following section.

Two approaches will be taken to gain insight into the frequency domain product of force and velocity. First a relationship will be derived between the average energy dissipated in the elements during a cycle and the real part of the frequency domain product of force and velocity. In the second approach, a simple form will be assumed for the mechanical impedance and the resulting contributions to the real and reactive power will be analyzed. The forms of these contributions will be related to system energy terms and used to derive approximate formula for system natural frequencies and loss factors.

To begin the analysis of the physical significance of the real and imaginary parts of the frequency domain system model proposed in Equation (2.19), the various contributions of the terms of (2.19) to the real and reactive power must be determined. Multiplying Equation (2.19) by a half and dividing the products into their real and imaginary parts, Equation (2.19) can be put in the form:

$$(P_P + iX_P) = (P_E + iX_E) \tag{2.28}$$

where P_P and X_P are the real and imaginary parts of:

$$P_P + iX_P = \mathrm{Re}\left\{\frac{1}{2}\mathbf{v}_G^H \mathbf{F}_{G\text{-}P}\right\} + i\ \mathrm{Im}\left\{\frac{1}{2}\mathbf{v}_G^H \mathbf{F}_{G\text{-}P}\right\} \tag{2.29}$$

and P_E and X_E are the real and imaginary parts of:

$$P_E + i\,X_E = \mathrm{Re}\left\{\frac{1}{2}\mathbf{v}_G^H \mathbf{Z}_G(\mathbf{v}_G, s)\mathbf{v}_G\right\} + i\ \mathrm{Im}\left\{\frac{1}{2}\mathbf{v}_G^H \mathbf{Z}_G(\mathbf{v}_G, s)\mathbf{v}_G\right\} \tag{2.30}$$

These terms are all frequency dependant; and in the case of the system impedance matrix, they can be amplitude dependant also.

At this point, it is desirable to gain some physical insight into the source of these frequency domain power terms. To make this easier, some simplifying assumptions will be made for the system in Equation (2.28). It will be assumed now that the system is in steady state and the complex forces and velocities of Equations (2.28) to (2.30) represent the magnitude and phase of sinusoidal signals. It will also be assumed that the system is linear and reciprocal. This means that the system can be represented by a symmetric impedance matrix. This assumption will not limit the derivations applicability for damped structural systems since systems with material damping or internal resonances still maintain reciprocity.

We will examine the time domain expression for power dissipated in a cycle first and relate this to the real part of the frequency domain product, P_E. The forces due to the system elements can be represented as a function of the system velocity vector and the system impedance matrix using Equation (2.10). For a linear system being forced at frequency, ω, this frequency domain force can be expressed in the time domain

$$\mathbf{F}_{G\text{-}L}(t) = \mathbf{F}_R \cos\omega t + \mathbf{F}_I \sin\omega t \tag{2.31}$$

and likewise the velocity can be expressed

$$\mathbf{v}_G(t) = \mathbf{v}_R \cos\omega t + \mathbf{v}_I \sin\omega t \tag{2.32}$$

Using these time domain expressions for the elemental forces and velocities, the energy dissipated in the elements in a cycle of period T would be written:

$$E_{dis} = \int_0^T \left[\mathbf{v}_G^T(t) \cdot \mathbf{F}_{G\text{-}L}(t)\right] dt \tag{2.33}$$

When evaluating the integral, the terms containing a product of sine and cosine integrate to zero leaving only terms with squares of sines or cosines. These terms integrate to 1/2 T over one cycle leaving

$$\frac{E_{dis}}{T} = \bar{P} = \frac{1}{2}\left[\mathbf{v}_R^T \cdot \mathbf{F}_R + \mathbf{v}_I^T \cdot \mathbf{F}_I\right] = \text{real}\left\{\frac{1}{2}\mathbf{v}_G^H \cdot \mathbf{F}_{G\text{-}L}\right\} \tag{2.34}$$

Since **F** can be expressed in terms of the impedances of the system and its velocities, Equation (2.34) can be put into a quadratic form for the average power dissipation in a cycle

$$\frac{E_{dis}}{T} = \text{Real}\left\{\frac{1}{2}\mathbf{v}_G^H(s)\mathbf{Z}_G(s)\mathbf{v}_G(s)\right\} \tag{2.35}$$

The right hand side of Equation (2.35) is identical in form to the first term on the right hand side of (2.30). Therefore we can conclude that for linear systems

$$P_E = P_P = \frac{E_{dis}}{T} \tag{2.36}$$

Thus the real part of the product of the Laplace transformed forces and velocities is numerically equal to the average power dissipation in a cycle. This explains why this term is named the real power when in fact its relation to that time domain quantity was not obvious. This frequency domain expression for energy dissipation will be used in developing an approximate method for calculating the system loss factor in the next section.

Equation (2.35)'s validity for nonlinear systems is limited to the degree that the elemental forces and velocities can be expressed as simple phase shifted sinusoids with a single frequency component. If the nonlinearities introduce higher order harmonics or other coupling which results in a more complex time history, then Equation (2.32) and consequently (2.35) are not strictly valid. If however the nonlinearities introduce only small perturbations to the otherwise linear response, then Equation (2.35) can be said to be approximately valid.

The nature of the complex part of the product, X_E, is more subtle. It represents the product of the forces and velocities that are in quadrature. These power terms integrate to zero over a period of the system, although the intermediate integrals can have some finite value.

The physical significance of the reactive power will be interpreted in terms of the contributions from the real and imaginary parts of the system velocity vector and impedance matrix. As before, the system will be assumed to be linear and reciprocal. A simple dynamic system impedance model will be assumed in order to relate the components of the reactive power to kinetic and potential energies. First, the real and reactive power in the elements can be expressed for general systems in terms of the quadratic form involving the system impedance matrix:

$$P_E + iX_E = \frac{1}{2}v_G^H Z_G v_G = \frac{1}{2}\left(v_R - iv_I\right)^T \left(Z_R + iZ_I\right)\left(v_R + iv_I\right) \qquad (2.37)$$

expanding,we obtain

$$P_E = \frac{1}{2}\left(v_R^T Z_R v_R + v_I^T Z_I v_R - v_R^T Z_I v_I + v_I^T Z_R v_I\right) \qquad (2.38a)$$

and

$$X_E = \frac{1}{2}\left(v_R^T Z_I v_R + v_R^T Z_R v_I - v_I^T Z_R v_R + v_I^T Z_I v_I\right) \qquad (2.38b)$$

If the previous assumption of a symmetric impedance matrix is applied, then P_E and X_E reduce to

$$P_E = \frac{1}{2}\left(v_R^T Z_R v_R + v_I^T Z_R v_I\right) \qquad (2.39a)$$

$$X_E = \frac{1}{2}\left(v_I^T Z_I v_I + v_R^T Z_I v_R\right) \qquad (2.39b)$$

Notice that P_E and X_E involve only the real and imaginary parts of the global impedance matrix respectively. This leads to some conclusions concerning damping in structural systems. Since, by (2.36), P_E is equivalent to the average power dissipation in a cycle, we discover that the system's energy dissipation at a particular frequency is dependant on two factors, the size of the real portion of the system impedance matrix and its placement in relation to the system modeshape at that frequency. Both factors are important in maximizing the energy dissipation product in (2.39a).

At this point a form for the system impedance matrix must be assumed in order to gain further insight into the nature of the reactive power. Although the actual system impedance can be a complicated function of the complex frequency, within a narrow frequency band the complicated

expressions can be represented with varying degrees of accuracy by a simple impedance model containing equivalent mass, stiffness, and damping matrices. In this simple structural model, the global impedance matrix has the form:

$$\mathbf{Z}_G(s) = \mathbf{Z}_R(s) + i\mathbf{Z}_I(s) = \mathbf{C} + \left(\mathbf{M}s + \frac{\mathbf{K}}{s}\right) = \mathbf{C} + i\omega\left(\mathbf{M} - \frac{\mathbf{K}}{\omega^2}\right) \tag{2.40}$$

where **C** is the equivalent damping matrix, **M** is the equivalent mass matrix , and **K** is the equivalent stiffness matrix. Substituting Equation (2.40) into the expression for real and reactive power, Equation (2.39) leads us to several conclusions. The first is that the real power dissipated, P_E, depends solely on the complex modeshape and the equivalent system damping matrix, **C**. With a more general form for the impedance, the dissipated power could also depend on any complex part of the mass or stiffness matrix. These complex parts can result from the complex modulus representation of material damping or viscoelastic materials or from internal system resonances. They contribute to the real part of the impedance matrix and thus to the power dissipation as is demonstrated in equation (2.39).

Secondly, the reactive power in the elements, X_E, is a function of the effective mass and stiffness matrices and the complex velocity modeshapes. This dependence on the mass and stiffness matrix is of a very specific form. If the system modeshapes are assumed to be primarily real, then the first term of Equation (2.39b) can be neglected and

$$X_E = \frac{1}{2}\mathbf{v}_R^T\mathbf{Z}_I\mathbf{v}_R \cong \frac{1}{2}\omega\left(\mathbf{v}_R^T\mathbf{M}\mathbf{v}_R - \mathbf{v}_R^T\frac{\mathbf{K}}{\omega^2}\mathbf{v}_R\right) = \frac{2\pi}{T}(KE - PE) \tag{2.41a}$$

$$X_E = \frac{2\pi}{T}L \tag{2.41b}$$

Where L is the well-known system Lagrangian. So for linear, reciprocal systems which can be represented by the effective impedance of the form of Equation (2.40) and which have predominantly real modeshapes, the imaginary reactive power represents the average difference between kinetic and potential energy at a given frequency. Systems with predominantly real modeshapes are those with symmetric matrices and light damping. For systems with very complex modeshapes (ie, highly damped) the definitions of potential and kinetic energy become clouded since at no time in the cycle is all

the energy either potential or kinetic. This is the result of different parts of the structure being out of phase with each other in very complex modeshapes. Expression (2.40) will be used to derive the effective mass and stiffness matrix for a frequency dependent system as will be shown in Section 2.6

At this point the quadratic product of the frequency dependent modeshapes and the system impedance matrix has been analyzed and understood in terms of the energies in predominantly linear, lightly damped, reciprocal systems. For such systems, the quadratic expression can be written:

$$\frac{1}{2}\mathbf{v}_G^H \mathbf{Z}_G \mathbf{v}_G = \frac{1}{T}\left(E_{dis} + i2\pi L\right) \tag{2.42}$$

This compact form is very useful in determining properties of the system such as modal frequencies and loss factors as will be discussed in the next section.

2.6 Quadratic Approximations of Frequency and Loss Factor

In this section approximate methods for calculating natural frequency and damping from the global impedance matrix will be developed. These methods involve using approximate mode shapes in a manner similar to the way in which they are used in the Rayleigh Quotient for natural frequencies. These forms can be very useful for finding approximate poles of a system, since finding the exact poles for the frequency dependent system can be difficult (These difficulties are outlined by Anderson in Ref. [14]).

In general a natural mode of the system occurs when the determinant of the impedance matrix equals zero, Ref [15].

$$\left|\mathbf{Z}_G(s)\right| = 0 \tag{2.43}$$

The process of finding the values of s in the complex plane is complicated by several factors and usually requires a numerical procedure. The procedure used in this report is presented in Appendix A, Section A.4. One complicating factor is that Z is very often a complicated, non-linear function of the complex frequency, s. It can involve transcendental expressions or other nonlinear forms. Another complicating factor is that for higher order systems the determinant of the impedance matrix can become extremely large

and thereby cause computational difficulties. In the exact calculation of the eigenvalues of the system, a good approximate initial value helps to circumvent these difficulties. In this section, expressions will be derived for these approximate values.

One common way of finding the approximate natural frequencies of an undamped system is to employ the Rayleigh Quotient, Ref. [16]. The quotient is expressed as the ratio of two quadratic forms, that of strain to reduced kinetic energy:

$$\omega_n^2 \cong \frac{\frac{1}{2}x_G^T K_G x_G}{\frac{1}{2}x_G^T M_G x_G} \tag{2.44}$$

In practice, it makes no difference whether displacement or velocity modeshapes are used in (2.44) since in steady state the frequency constant will cancel out. Thus (2.44) can equally well be written in terms of velocity modeshapes:

$$\omega_n^2 \cong \frac{\mathrm{Re}(\frac{1}{2}v_G^T K_G v_G)}{\mathrm{Re}(\frac{1}{2}v_G^T M_G v_G)} \tag{2.45}$$

and corresponds exactly to the condition that the L in Equation (2.41b) equals zero.

Now we are going to try to find a way to calculate the stiffness and mass matrices used in (2.45) from the system or elemental impedance matrices. This method is also presented in Appendix A. The impedance matrix is a complex, non-linear function of frequency which can be obtained from a simple dynamic test of a structure, whereas the stiffness and mass matrices for complicated sub-structures with internal resonances or frequency varying properties are sometimes difficult to model. The goal is to derive a simple method for finding the equivalent system stiffness and mass matrices for systems which contain elements with frequency variable properties and high damping. This method will also be useful in analysis of lower order system models which contain resonant subsystems due to the reduced out degrees of freedom.

One way to accomplish this is to assume that in a given frequency range the system impedance matrix can be modelled using equivalent mass,

stiffness, and damping matrices in the form presented in Section 2.5 in Equation (2.40)

$$Z_G(s) = Z_R(s) + iZ_I(s) = C + \left(Ms + \frac{K}{s}\right) \tag{2.46}$$

The values for the equivalent matrices are dependant on the frequency range in which the approximation is desired to be valid since the properties of the impedance matrix do not necessarily have the same frequency dependance as the assumed model.

To find these equivalent matrices from the impedance, the impedance must be evaluated at $s = i\omega$, where ω is a frequency within the desired range, and again at $s = \omega$. The resulting system of equations

$$Z_G(i\omega_1) = C_G + i\omega_1\left(M_G - \frac{K_G}{\omega_1^2}\right) \tag{2.47a}$$

$$Z_G(\omega_1) = C_G + \omega_1\left(M_G + \frac{K_G}{\omega_1^2}\right) \tag{2.47b}$$

can be solved to find the values of the equivalent mass and stiffness matrices at the initial assumed frequency.

$$M_G \cong \frac{\mathrm{Re}\left\{Z_G(\omega_1)\right\} - \mathrm{Re}\left\{Z_G(i\omega_1) + i\,Z_G(i\omega_1)\right\}}{2\omega_1} \tag{2.48a}$$

$$K_G \cong \frac{\omega_1\left(\mathrm{Re}\left\{Z_G(\omega_1)\right\} + \mathrm{Re}\left\{i\,Z_G(i\omega_1) - Z_G(i\omega_1)\right\}\right)}{2} \tag{2.48b}$$

For accurate approximations, the frequency, ω_1, in (2.48a) and (2.48b) should be close to the mode of interest. It can be chosen by visual inspection of the system transfer function as done in the procedure outlined in Appendix A Section A.3. The value for the mass and stiffness matrices can then be substituted into Rayleigh's Quotient to obtain a closer approximation for the resonant frequency to which that modeshape belongs using Equation (2.45)

Now that an approximate natural frequency has been found using (2.45), that frequency can be used for calculating the system loss factor. The

loss factor is proportional to the ratio of energy dissipated in a cycle divided by the maximum strain energy in the system.

$$\eta \equiv \frac{E_{dis}}{2\pi U} \tag{2.49}$$

where U is the maximum strain energy in the system. As shown before in Equation (2.35), the energy dissipated in a cycle, E_{dis}, can be represented by a quadratic form. This expression along with the expression for the strain energy derived in both (2.41) and (2.26) gives a simple approximate expression for the system loss factor:

$$\eta \cong \frac{\text{Real}\left\{\frac{1}{2}\mathbf{v}_G^H\left(\mathbf{Z}_G(i\omega_2)\right)\mathbf{v}_G\right\}}{\text{Imag}\left\{\frac{1}{2}\mathbf{v}_G^H\left(\frac{i\,\mathbf{K}_G}{\omega_2}\right)\mathbf{v}_G\right\}} \tag{2.50}$$

where ω_2 is the approximate natural frequency calculated from Equation (2.45).

The collection of terms on the bottom represents the strain energy portion of the Lagrangian derived from the system impedance matrix in Equation (2.41). The period of the vibration cancels on the top and the bottom and the extra 2π factor is accounted for by Expression (2.49). Equation (2.50) allows the designer to make a quick estimate of the system loss factor once a mode shape is assumed. Assumed or experimentally determined impedances or modeshapes can be used in Equation (2.50) to determine system loss factor. The modeshapes used in (2.50) can be complex but the imaginary part must be small since the expression for strain energy is inaccurate for very complex modeshapes as is explained for (2.41). Equation (2.50) is also valid for systems with slight nonlinearities using the nonlinear impedances defined in Equation (2.18). In the special case of a proportionally damped, linear, reciprocal system, Equation (2.50) is valid for large amounts of damping.

Since Equation (2.50) is not constrained to linear viscous or proportional damping, it is very useful in evaluating unusual damping schemes such as resonant dampers or viscoelastic materials.

2.7 Frequency and Loss Factor Sensitivities

In this section, the sensitivities of various system properties to variations of the network constitutive properties or mode shapes will be examined. A good source for a more in depth exposure to network sensitivities is Ref. [6]. This section will not attempt to derive the formulas but merely apply the formulas already developed for electrical networks to mechanical systems. The first items considered will be the frequency and loss factor sensitivities to variations in the system impedance matrix. Later the port impedance matrix sensitivities to variations of the system parameters will be analyzed using Cohn's Theorem, a derivative of Tellegen's Theorem and presented in Ref. [6].

The quadratic forms used in Rayleigh's Quotient, Equation (2.45) and in the approximate expression for the system loss factor, Equation (2.50) possess sensitivity properties that make them useful for approximate analysis. The frequency and loss factor obtained through this method is insensitive to first order variations in the modeshapes (Ref. [16]). This gives some freedom in the choice of modeshape that still give accurate results for the quantity. An approximate modeshape such as one derived from an undamped model can be used with confidence. In particular for loss factor calculation, this implies that the complete complex modeshape need not be used in Equation (2.50). Instead the real part of a slightly complex modeshape can be used to obtain a reasonable estimate of modal damping.

The frequency and loss factor are very sensitive, however, to variations of the system properties. The sensitivity depends on how the variation is weighted by the mode shape, e.g. in areas of high strain, changes in stiffness can produce large chances in frequency and damping. The sensitivities can be useful for determining the best placement of damping treatments and devices.

To determine the sensitivities of the system frequencies and loss factors to variations in the system properties, we will first examine a general variation for any ratio of quadratics and apply this general form to the quotients for loss factor and frequency in Equations (2.45) and (2.50) respectively. If we assume a general form

$$y = \frac{\mathbf{x}^T \mathbf{A}\, \mathbf{x}}{\mathbf{x}^T \mathbf{B}\, \mathbf{x}} \tag{2.51}$$

then letting

$$y = y_0 + \delta y\,,\ A = A_0 + \delta A\,,\ \text{and}\ B = B_0 + \delta B \tag{2.52}$$

a solution for δy can be obtained.

$$\delta y = y \cdot \left[\frac{x^T \delta A\, x}{x^T A_0\, x} - \frac{x^T \delta B\, x}{x^T B_0\, x} \right] \tag{2.53}$$

Applying this general formula to the approximate quadratic expressions for system loss factor and frequency leads to the sensitivities of these parameters to changes in the system properties. The variation of the loss factor for system parameters variation can be derived from (2.50) using (2.53) as

$$\delta\eta = \eta \cdot \left[\frac{\text{Real}\left\{ v_G^H \delta Z_G(s) v_G \right\}}{\text{Real}\left\{ v_G^H Z_G(s) v_G \right\}} - \frac{\text{Imag}\left\{ v_G^H \delta Z_{stif}(s) v_G \right\}}{\text{Imag}\left\{ v_G^H Z_{stif}(s) v_G \right\}} \right] \tag{2.54}$$

where Z_{stif} is defined:

$$Z_{stif}(s) = -\frac{K_G}{s} \tag{2.55}$$

Variations of frequencies can be found in a like manner from (2.45).

$$\delta\omega_n^2 = \omega_n^2 \cdot \left[\frac{\text{Re}\left\{ v_G^H\, \delta K_G\, v_G \right\}}{\text{Re}\left\{ v_G^H\, K_G\, v_G \right\}} - \frac{\text{Re}\left\{ v_G^H\, \delta M_G\, v_G \right\}}{\text{Re}\left\{ v_G^H\, M_G\, v_G \right\}} \right] \tag{2.56}$$

where K_G and M_G are defined from Equation (2.48).

The form of (2.53) is interesting because all the variations appear as ratios over the unvaried quantity. The expression for the variation of loss factor is also insensitive to first order variations of the modeshapes just as is the expression for the loss factor.

An expression can also be derived for the sensitivity of the port impedance of a system to variations of the internal elements of the system. This expression can be quite useful in system analysis where one would like the driver and port impedances to be matched for maximum power flow at the junction. This impedance matching concept is very applicable to actuator placement and structural design for ease of control - concepts found in intelligent structures. By determining the sensitivities of the port impedances to changes of the system properties, these properties can be

designed to maximize the imaginary part of the port impedance matrix and thus maximize the real power flow in that particular port.

The port impedance is defined like the elemental impedances as the ratio of complex force to velocity at the ports. A global port impedance matrix can be defined just as the elemental impedance matrix to describe the external forces at the nodes in terms of the nodal velocities of the system. Therefore, a global port impedance matrix can be defined to replace the vector of port forces in Equation (2.19)

$$\mathbf{F}_{G\text{-}P}(s) = \mathbf{Z}_{G\text{-}P}(s)\,\mathbf{v}_G \tag{2.57}$$

Replacing these port forces, Tellegen's Theorem expressed in Equation (2.19), becomes:

$$\mathbf{v}_G^H \mathbf{Z}_{G\text{-}P}(s)\mathbf{v}_G = \mathbf{v}_G^H \mathbf{Z}_G(s)\mathbf{v}_G \tag{2.58}$$

Now a sensitivity theorem used in electrical network analysis, Cohn's Theorem, Ref. [6], can be applied to the system in (2.58) to determine the relationships between changes in the elemental impedance matrix and changes in the port impedance matrix. For a given element of the global impedance matrix, $Z^{\alpha\beta}$, the change in port element, $Z^{\sigma\gamma}$, can be evaluated:

$$\delta Z_{G\text{-}P}^{\sigma\gamma} = \delta Z_G^{\alpha\beta} \cdot \left(\frac{\tilde{v}_\alpha \cdot \hat{v}_\beta}{\tilde{v}_\sigma \cdot \hat{v}_\gamma} \right) \tag{2.59}$$

The ~ and ^ symbols specify velocity modeshapes from two different experiments. The ~ signifies the velocity modeshape which results with only the port at node σ free to move, all other ports are fixed. Likewise the ^ velocity modeshape is taken with only the port at node γ free and all other ports fixed.

2.8 Mechanical System Example

In this section the global impedance matrix for a simple dynamic mechanical system will be derived. The purpose of this derivation is to provide some insight into the techniques described in the previous sections. The dynamic system modelled in this example is presented using the

traditional symbology in Figure 2.3a. This dynamic system can be represented by the network in Figure 2.3b which contains 4 nodes and 7 branches.

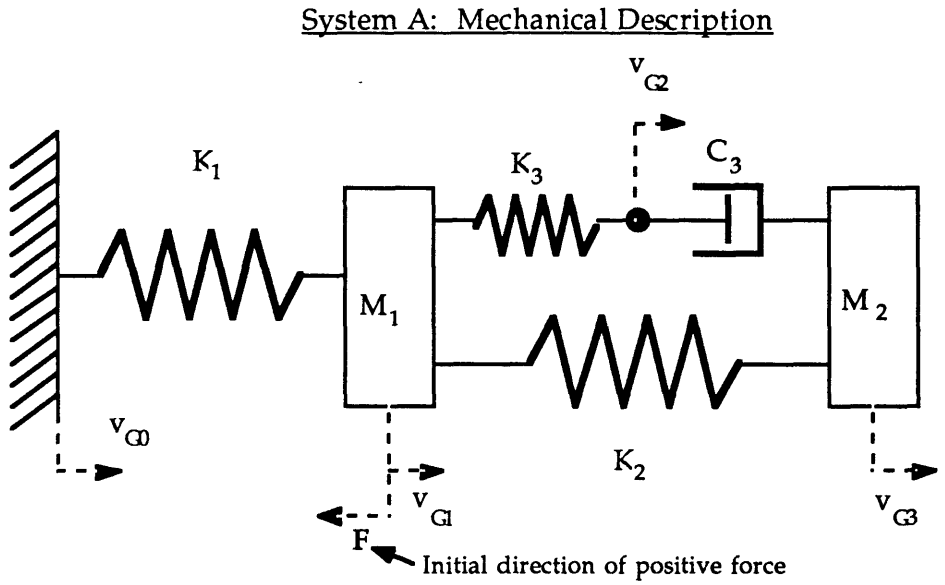

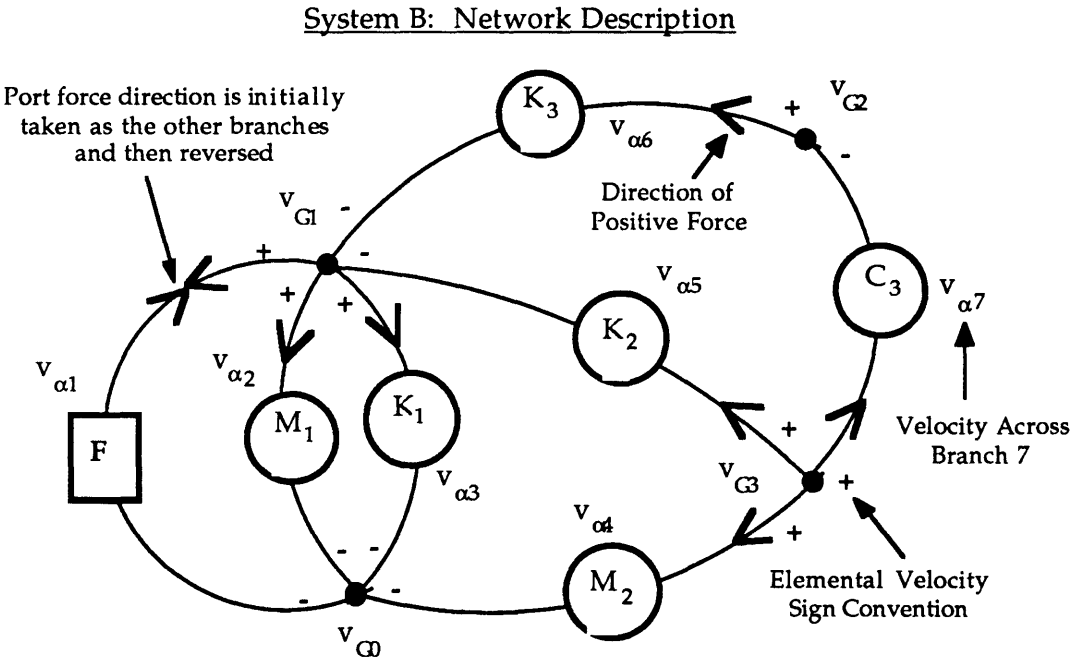

Figure 2.3a & b Sample Mechanical System (a) and its Network Counterpart (b) Showing the Sign Conventions for Forces and Velocities

There are some interesting points to consider in the conversion from the dynamic system in Figure 2.3a to the network in Figure 2.3b. The first point is that all the masses correspond to branches to ground as was described in Section 2.2.1. The second point is that the force (on mass-1) is represented as a port between the node-1 and the ground node-0. For each branch there is a positive velocity differential defined by the signs at the nodes. The positive force is represented as an arrow in the direction from the positive node to the negative node of the element. This symbol represents a restorative force through the element. The port has been represented in Figure 2.3b as having the same sign convention as the other branches just as it was in the initial derivation of Tellegen's Theorem. This convention will later be reversed when the ports are separated from the elements of the system.

The force compatibility relations can be calculated in a manner exactly analogous to the calculation of the currents in an electrical network. The sum of the forces going into and out of a node must equal zero. Those leaving a node are counted as negative, and those going into a node are taken as positive. It is important to notice that the absolute direction of the force is not important to the expression of force compatibility only the force flow relative to the node is important. Thus, only the topology, the interconnections between the nodes, is important to the network diagram and not the specific layout of the diagram.

From Equation 2.2 in Section 2.2.2, there are 4 independent forces in the network in Figure 2.3b. This number can be derived by noting that there are 7 branches, 4 nodes and just one separate network (7 - 4 + 1 = 4). This means there must be 3 linear relations relating the branch forces. These can be found by taking the force balance at 3 nodes. The force summation at the first node, v_{G1}, can be written

$$- F_{\alpha 1} - F_{\alpha 2} - F_{\alpha 3} + F_{\alpha 5} + F_{\alpha 6} = 0 \qquad (2.60a)$$

Likewise for node 2,

$$F_{\alpha 7} - F_{\alpha 6} = 0 \qquad (2.60b)$$

and node 3,

$$- F_{\alpha 4} - F_{\alpha 5} - F_{\alpha 7} = 0 \qquad (2.60c)$$

If we take the force in the port at branch-1 and the forces at branches 2, 5, 6 to be the independent forces, then the loop matrix can be found in the form of Equation 2.1

$$\begin{bmatrix} F_{\alpha 1} \\ \cdot \\ \cdot \\ \cdot \\ \cdot \\ \cdot \\ F_{\alpha 7} \end{bmatrix} = \begin{bmatrix} 1 & 0 & 0 & 0 \\ 0 & 1 & 0 & 0 \\ -1 & -1 & 1 & 1 \\ 0 & 0 & -1 & -1 \\ 0 & 0 & 1 & 0 \\ 0 & 0 & 0 & 1 \\ 0 & 0 & 0 & 1 \end{bmatrix} \begin{bmatrix} F_{\alpha 1} \\ F_{\alpha 2} \\ F_{\alpha 5} \\ F_{\alpha 6} \end{bmatrix} \tag{2.61}$$

The relationship for velocity compatibility, Equation (2.3), can be derived by taking the transpose of the loop matrix and multiplying it by the vector of branch velocities.

$$\begin{bmatrix} 1 & 0 & -1 & 0 & 0 & 0 & 0 \\ 0 & 1 & -1 & 0 & 0 & 0 & 0 \\ 0 & 0 & 1 & -1 & 1 & 0 & 0 \\ 0 & 0 & 1 & -1 & 0 & 1 & 1 \end{bmatrix} \begin{bmatrix} v_{\alpha 1} \\ \cdot \\ \cdot \\ \cdot \\ \cdot \\ \cdot \\ v_{\alpha 7} \end{bmatrix} = \begin{bmatrix} 0 \\ 0 \\ 0 \\ 0 \end{bmatrix} \tag{2.62}$$

Each row of the transposed loop matrix can be seen to represent a looped path over certain branches in the network around which the velocities across the branches must sum to zero. The sign of the velocities is taken with respect to the orientation of the positive and negative nodes of a branch. At this stage, the first form of Tellegen's Theorem, Equation (2.5), can be expressed for this system as a summation over the branches. In matrix form this summation becomes

$$\begin{bmatrix} v_{\alpha 1} & \cdot & \cdot & \cdot & v_{\alpha 7} \end{bmatrix} \begin{bmatrix} F_{\alpha 1} \\ \cdot \\ \cdot \\ \cdot \\ F_{\alpha 7} \end{bmatrix} = \mathbf{v}_{\alpha}^{T} \mathbf{F}_{\alpha} = 0 \tag{2.63}$$

Now by redefining the port at branch-1 to have the opposite sign convention from the elements at the other branches, the port can be separated to the right hand side of the equality.

$$\begin{bmatrix} v_{\alpha 2} & \cdot & \cdot & \cdot & v_{\alpha 7} \end{bmatrix} \begin{bmatrix} F_{\alpha 2} \\ \cdot \\ \cdot \\ \cdot \\ F_{\alpha 7} \end{bmatrix} = v_{\alpha 1} F_{\alpha 1} \tag{2.64}$$

Until this point, the fact that some of the branches are springs and other are masses or dampers has not been introduced. We can now define the elemental impedance matrix, Z_L based on the constitutive relations of the various branches in accordance with Equation 2.10.

$$\begin{bmatrix} F_{\alpha 2} \\ F_{\alpha 3} \\ F_{\alpha 4} \\ F_{\alpha 5} \\ F_{\alpha 6} \\ F_{\alpha 7} \end{bmatrix} = \begin{bmatrix} \frac{K_1}{s} & 0 & 0 & 0 & 0 & 0 \\ 0 & M_1 s & 0 & 0 & 0 & 0 \\ 0 & 0 & M_2 s & 0 & 0 & 0 \\ 0 & 0 & 0 & \frac{K_2}{s} & 0 & 0 \\ 0 & 0 & 0 & 0 & \frac{K_3}{s} & 0 \\ 0 & 0 & 0 & 0 & 0 & C_3 \end{bmatrix} \begin{bmatrix} v_{\alpha 2} \\ v_{\alpha 3} \\ v_{\alpha 4} \\ v_{\alpha 5} \\ v_{\alpha 6} \\ v_{\alpha 7} \end{bmatrix} \tag{2.65}$$

This matrix can be reduced if it is transformed from an element by element representation to the global coordinate system of the nodes. This is accomplished using the transformation matrix, T, defined in Equation (2.15). The transformation matrix is constructed by noting that the velocity across

the elements is the difference of the absolute velocities at the end nodes of the elements. The transformation matrix can thus be defined:

$$\begin{bmatrix} v_{\alpha 1} \\ \cdots \\ v_{\alpha 2} \\ \cdot \\ \cdot \\ \cdot \\ v_{\alpha 7} \end{bmatrix} = \begin{bmatrix} v_P \\ \cdots \\ v_L \end{bmatrix} = \begin{bmatrix} -1 & 1 & 0 & 0 \\ \cdots & \cdots & \cdots & \cdots \\ -1 & 1 & 0 & 0 \\ -1 & 1 & 0 & 0 \\ -1 & 0 & 0 & 1 \\ 0 & -1 & 0 & 1 \\ 0 & -1 & 1 & 0 \\ 0 & 0 & -1 & 1 \end{bmatrix} \begin{bmatrix} v_{G0} \\ v_{G1} \\ v_{G2} \\ v_{G3} \end{bmatrix} \tag{2.65}$$

Since v_{G0} is always equal to zero, the first column of the transformation matrix can be eliminated to produce a 7 by 3 matrix. The upper partition of the transformation matrix represents T_P from Equation (2.17a). The lower partition of the reduced transformation matrix, T_L can be used to determine the global impedance matrix for the system by employing Equation (2.17a). This yields

$$Z_{G\text{-}L} = \begin{bmatrix} M_1 s + \dfrac{K_1 + K_2 + K_3}{s} & -\dfrac{K_3}{s} & -\dfrac{K_2}{s} \\ -\dfrac{K_3}{s} & C_3 + \dfrac{K_3}{s} & -C_3 \\ -\dfrac{K_2}{s} & -C_3 & M_2 s + C_3 + \dfrac{K_2}{s} \end{bmatrix} \tag{2.67}$$

Finally, we shall illustrate one of the reduction techniques discussed in Section 2.3, known as static condensation. Using this technique, we can eliminate the massless degree of freedom at node-2 by noting that no external force is applied at that node. Static condensation reduces a system in the form

$$\begin{bmatrix} F_{RET} \\ \cdots \\ 0 \end{bmatrix} = \begin{bmatrix} Z_{RET} & Z_{RET\text{-}RED} \\ Z_{RED\text{-}RET} & Z_{RED} \end{bmatrix} \begin{bmatrix} v_{RET} \\ v_{RED} \end{bmatrix} \tag{2.68}$$

to one in the form

$$F_{RET} = \bar{Z}_{RET} v_{RET} \tag{2.69}$$

where

$$\bar{Z}_{RET} = Z_{RET} - Z_{RET\text{-}RED} Z_{RED}^{-1} Z_{RED\text{-}RET} \tag{2.70}$$

Applying static condensation to eliminate node-2, the final reduced form of the global impedance matrix is obtained

$$Z_{G\text{-}L}(s) = \begin{bmatrix} M_1 s + \frac{K_1 + K_2}{s} + \frac{C_3 K_3}{C_3 s + K_3} & -\frac{K_2}{s} - \frac{C_3 K_3}{C_3 s + K_3} \\ -\frac{K_2}{s} - \frac{C_3 K_3}{C_3 s + K_3} & M_2 s + \frac{K_2}{s} + \frac{C_3 K_3}{C_3 s + K_3} \end{bmatrix} \tag{2.71}$$

This reduced global impedance matrix can be used in the frequency domain form of Tellegen's Theorem expressed in Equation (2.19) once the forces and velocities have been transformed to the Laplace domain.

2.9 Summary

In this chapter the fundamental relations for frequency domain analysis of mechanical systems have been presented based upon Tellegen's Theorem. The analysis of a structural system as a network of impedances was presented. Using the force equilibrium and displacement compatibility conditions for the system, a network power theorem, Tellegen's Theorem was derived. This theorem was applicable for general non-linear, time varying systems. The constitutive relations for the elements of the network were incorporated into Tellegen's Theorem in the frequency domain. The resulting terms were analyzed for their relation to common power quantities of a mechanical system. These quantities such as energy storage and dissipation were then used to form approximate expressions for the system frequencies and loss factor. The frequency domain analysis can be useful for complex damped systems such as for viscoelastic materials and resonators where properties of the system vary with frequency. The approximate methods allow efficient evaluation of the most common damping techniques for comparison and system damping enhancement design.

Chapter 3
Damping Mechanisms for Structural Systems

3.1 Overview

In this chapter models will be developed for some common damping enhancement methodologies applicable to space structures. The damping schemes of interest include viscoelastic surface treatments, tuned mechanical resonators called Proof Mass Dampers (PMDs), and a new resonant damping technique for structures which employs piezoelectric materials. Frequency domain models will be developed for these three methodologies, which can be incorporated into the system framework developed in the previous chapter.

Viscoelastic materials can be used to add damping to structures due to their high inherent loss factor. Their low stiffness, however, tend to limit their usefulness to non-structural surface treatments. A trade must be conducted between inherent loss factor and stiffness for determination of the optimum damping treatment for a given system. In addition to viscoelastic damping treatments, models of resonant dampers have been developed in this report. The resonant dampers discussed here are the classical proof mass damper and a unique application of shunted piezoelectrics which involve shunting the piezoelectric with a resonant circuit. Parallels will be drawn between these two resonant damping methods. Optimal tuning criteria for maximum energy dissipation will be derived for the resonant dampers and discussed in terms of their effect on the total system loss factors.

These two systems can be thought of as complementary since the proof mass damper appears as a point impedance in system modeling and thus damps out only the available kinetic energy. On the other hand, shunted piezoelectrics are modeled as multi-port impedances which derive their dissipation from the relative motion of two system nodes. Thus they can be thought of as dissipating structural strain energy. This differences will reflect on the optimum placement of the actual dampers.

3.2 Viscoelastic Material Damping

One method of increasing the damping in structural systems is to employ viscoelastic materials. Viscoelastic materials typically have a high material loss factor, and can be employed in high strain areas of the structure to increase the total structure loss factor, Ref. [17]. The relation between the high loss factor of a structural component and the loss factor of the total structure can be represented as an average of the system component loss factors weighted by the strain energy in the respective members (Ref. [17])

$$\eta_{tot} = \frac{\sum_{elements} U_{element}\eta_{element}}{\sum_{elements} U_{elements}} \tag{3.1}$$

Where U is the peak strain energy in the element of the structure. Techniques for improving structural damping with viscoelastics typically employ the viscoelastics in areas of high strain energy to take advantage of this weighting. The stiffness and loss factor of viscoelastic materials is also typically frequency and temperature dependent making a complete analysis of the system difficult. The use of frequency domain modelling of the viscoelastic greatly simplifies the analysis.

The form of the frequency dependence of the viscoelastic can be seen in Fig 3.1 for a typical damping material. The peak loss factor occurs in a narrow frequency range where the viscoelastic is in transition from its rubbery state to its glassy state. The stiffness of a viscoelastic material can be represented as a frequency dependant generalization of the complex material modulus:

$$E(\omega) = E_0(\omega).[1 + i\eta(\omega)] \tag{3.2}$$

A typical model of the frequency dependence can be determined by examining one of the models for viscoelastics, the Standard Linear Model (Figure 3.2).

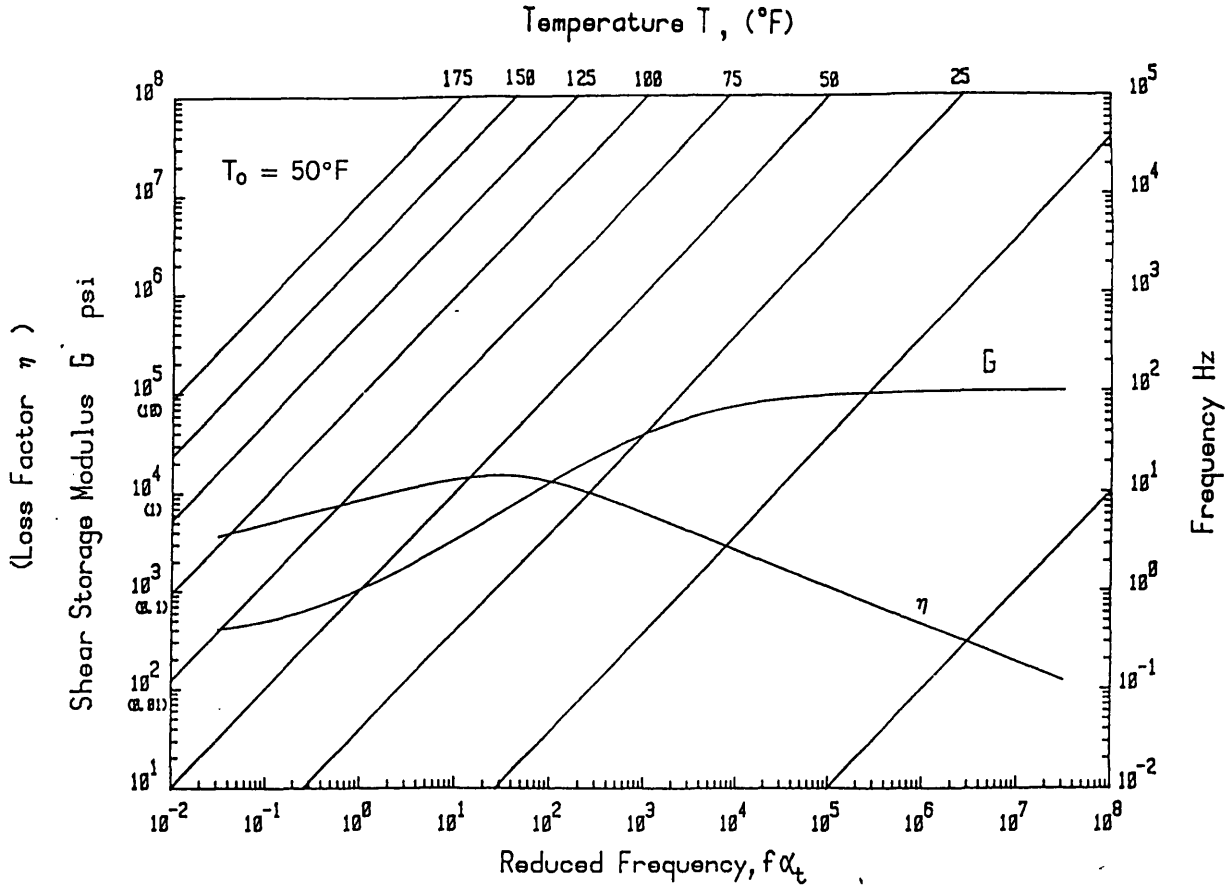

Figure 3.1 Viscoelastic Damping Material Design Monograph for Antiphon-13 Showing the Dependance of the Material Properties on Temperature and Frequency

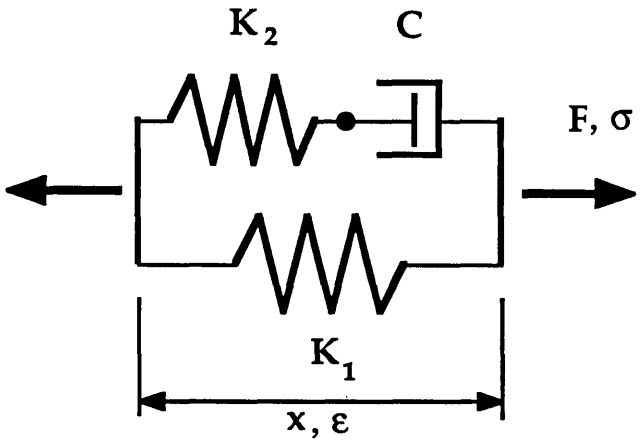

Figure 3.2 Standard Linear Model of a Viscoelastic Material

This mechanical model can be represented by a differential equation relating stress and strain, Ref [17]

$$\sigma + \alpha\dot{\sigma} = E\varepsilon + \beta E\dot{\varepsilon} \tag{3.3}$$

Taking the Laplace transform of the above equation leads to the expression for the frequency dependent ratio of stress to strain:

$$\frac{\sigma}{\varepsilon} = E(s) = \frac{E(1+ s\beta)}{(1 + s\alpha)} \tag{3.4}$$

This expression can be put in a form comparable to (3.2) to arrive at the frequency dependent expressions for stiffness and loss factor:

$$E_0(\omega) = \frac{E\omega\,(\beta - \alpha)}{1 + \omega^2\alpha^2} \tag{3.5a}$$

$$\eta(\omega) = \frac{\omega\,(\beta - \alpha)}{1 + \omega^2\alpha\beta} \tag{3.5b}$$

The constants α, β, and E are commonly found by regression analysis of experimental data. Often three regression variables do not adequately reflect the frequency variation of the material properties. In Ref [17], Equation (3.4) was generalized using higher order derivatives of stress and strain than those in (3.3). The stress strain relationship has been further generalized by incorporating techniques from fractional calculus into Equation (3.3) to allow more complicated variations of the modulus with frequency. The generalized expression for the frequency dependent stiffness of a viscoelastic is:

$$E(s) = \frac{E(1+ \sum_{n} \beta_n s^{b_n})}{1+\sum_{m} \alpha_m s^{a_m}} \tag{3.6}$$

Where the α_n and β_m are not necessarily integers. Equation (3.6) can also be divided into real and imaginary parts and compared to (3.2) to give the frequency dependant stiffness and damping.

Equation (3.6) presents an almost insurmountable problem for time domain analysis because it entails non-integer order derivatives. The equation lends itself very well to the Laplace domain system analysis outlined

in the previous chapter. Equation (3.6) can be converted to an impedance for a viscoelastic system element

$$Z_{visc}(s) = \frac{K_{visc}(E_{visc}(s),\text{geometry})}{s} \tag{3.7}$$

where E_{visc} is from (3.6). The impedance of the viscoelastic element can then be assembled into the global impedance matrix of the system. The global system loss factor can then be found using the techniques presented in (2.50) This equation can be shown to be analogous to Equation (3.1) above. The matrix multiplications takes the place of the summations over the elements. Frequency domain techniques can thus help model a useful damping technique which would otherwise be intractable.

3.3 Proof Mass Dampers

Another commonly used damping enhancement mechanisms is the classical Proof Mass Damper (PMD). This technique involves attaching a resonant mechanical device to a structure at points of high absolute motion of the structure. The resonant device is tuned both in its frequency and damping to one of the modes of the base system. The tuning of the device is done in such a way as to optimally damp the mode of the base structure. Other modes derive smaller damping benefits from the tuned damper. The PMD is very effective in damping the mode to which it is tuned. To determine just how effective, the classical model of a resonant mechanical system with an attached PMD will be examined. The model is shown schematically in Fig 3.3.

This model can be placed in the frequency domain and analyzed using the techniques outlined in Ref [18] and [19]. Using the structural impedances and the system structure outlined in the previous chapter, the equations of motion of this system can be represented:

$$\begin{bmatrix} sM + C_d + \frac{K + K_d}{s} & -C_d - \frac{K_d}{s} \\ -C_d - \frac{K_d}{s} & sM_d + C_d + \frac{K_d}{s} \end{bmatrix} \begin{bmatrix} v_1 \\ v_2 \end{bmatrix} = \begin{bmatrix} F \\ 0 \end{bmatrix} \tag{3.8}$$

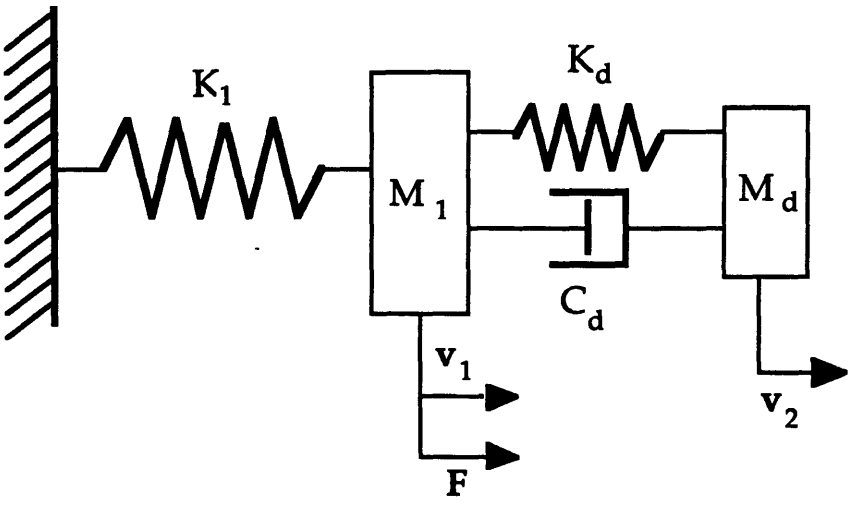

Figure 3.3 Diagram of a Simple 1-DOF System with Attached PMD

Since there is no external force on the degree of freedom (DOF) associated with the PMD, this node can eliminated from the vector of retained degrees of freedom using static condensation. This leads to a single effective point impedance relating the response of the main system to the forcing:

$$\left[sM + \frac{K}{s} + \frac{sM_d (C_d s + K_d)}{M_d s^2 + C_d s + K_d} \right] v_1 = Z_{eff}(s) v_1 = F \tag{3.9}$$

This reduced impedance can be seen to have terms which are related to the main system elements, K and M, and a complicated, complex term related to the resonant damping system. This term is the effective point impedance of the PMD at the system node and can be normalized using the traditional terms found in Ref. [18].

$$\frac{Z_{PMD}(s)}{sM} = \frac{\beta (\delta r \gamma + \delta^2)}{\gamma^2 + \delta^2 + \delta r \gamma} \tag{3.10}$$

where,

$$\beta = \frac{M_d}{M}, \quad \delta = \frac{\omega_d}{\omega_n}, \quad r = \frac{C_d}{M_d \omega_d}, \quad \gamma = \frac{s}{\omega_n} \tag{3.11}$$

Thus the PMD can be represented as a complex, frequency dependent point impedance at its connection to a system. The difficulty is determining the values of the non-dimensional parameters, δ and r, (given the mass ratio of

the damper β) which minimize the response of the structure to the forcing. The δ parameter represents the ratio of damper frequency tuning to system target modal frequency and the r parameter is related to the damping of the resonant subsystem.

The determination of the optimum parameter values is outlined in great detail by Miller, Ref. [5] and Juang, Ref. [20]. The optimum damper frequency ratio is found by examining two limiting cases for the system, the one with no damper in the PMD and the one with an infinite damper in the PMD. In the case with no damper there are two undamped resonances of the system as shown in Fig. 3.4. In the case with infinite damping value (r = infinity), the PMD is effectively locked to the base system and no energy is dissipated. This results in a single mode system. The transfer functions for these two systems intersect at two points , called the S and T points, which can be found by equating the two transfer functions. Equating the magnitudes of the transfer functions at these intersection points leads to a value of δ which can be shown to be optimum:

$$\delta_{opt} = \frac{1}{1+\beta} \tag{3.12}$$

Since the mass ratio β is always positive, this relation implies that the PMD will always be tuned to a frequency below the main structure's resonance. In the case of multi-mode systems, the system mass used in the mass ratio is the effective modal mass of the system normalized to the point at which the PMD is attached (Ref. [5]).

Having determined the optimum tuning ratio, the optimal damping for the PMD must be found. The limiting cases of no damping in the PMD or infinite damping in the PMD both produce system transfer functions with infinite amplitudes. The objective is to find an optimum damper value, C_d, between these two extremes which minimizes the maximum amplitude of the system transfer function. This is called a min-max criteria. The effect of damper values on the system transfer function can be seen in Fig. 3.5. The traditional manner of achieving a min-max is to set the slope of the system transfer function to zero at the S or T point. This produces the double humped transfer function of the optimally tuned PMD. The expression for r, though complicated, involves only β.

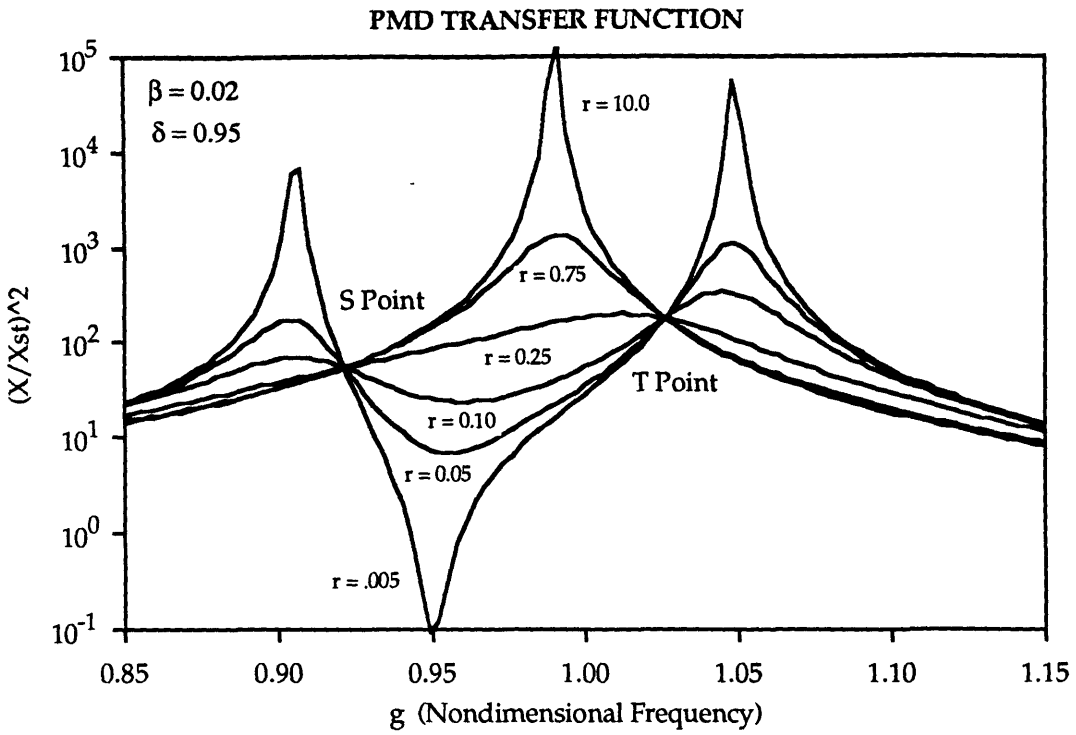

Figure 3.4 Transfer Function for a 1-DOF System with a PMD Attached Showing the Effect of Varying the PMD Dashpot from 0 to Infinity at Non-optimal Tuning

$$r_{opt}^2 = \left(\frac{4}{\delta_{opt}^2}\right)\frac{N - Q(X/X_{st})^2}{P(X/X_{st})^2 - M} \tag{3.13a}$$

where:

$$M = \frac{4\left[1 + \sqrt{\frac{\beta}{2+\beta}}\right]}{1+\beta} \tag{3.13b}$$

$$N = \left[\frac{\beta + (1+\beta)\sqrt{\frac{\beta}{2+\beta}}}{(1+\beta)^2}\right]^2 \tag{3.13c}$$

$$P = \frac{4\beta\left[1 + \sqrt{\frac{\beta}{2+\beta}}\right]}{(1+\beta)^2(2+\beta)} \tag{3.13d}$$

$$Q = \left[\frac{\beta\left[(2+\beta)\sqrt{\frac{\beta}{2+\beta}} + (1+\beta)\right]}{(1+\beta)^2(2+\beta)}\right]^2 \tag{3.13e}$$

$$\left(\frac{X}{X_{st}}\right)^2 = \frac{2+\beta}{\beta} \tag{3.13f}$$

This expression for r_{opt} and the previous one for δ_{opt} define the system with minimum steady state response for a given value of the mass ratio, β. The larger the mass ratio the more damping the PMD can introduce into the system. The cost is obviously additional system mass.

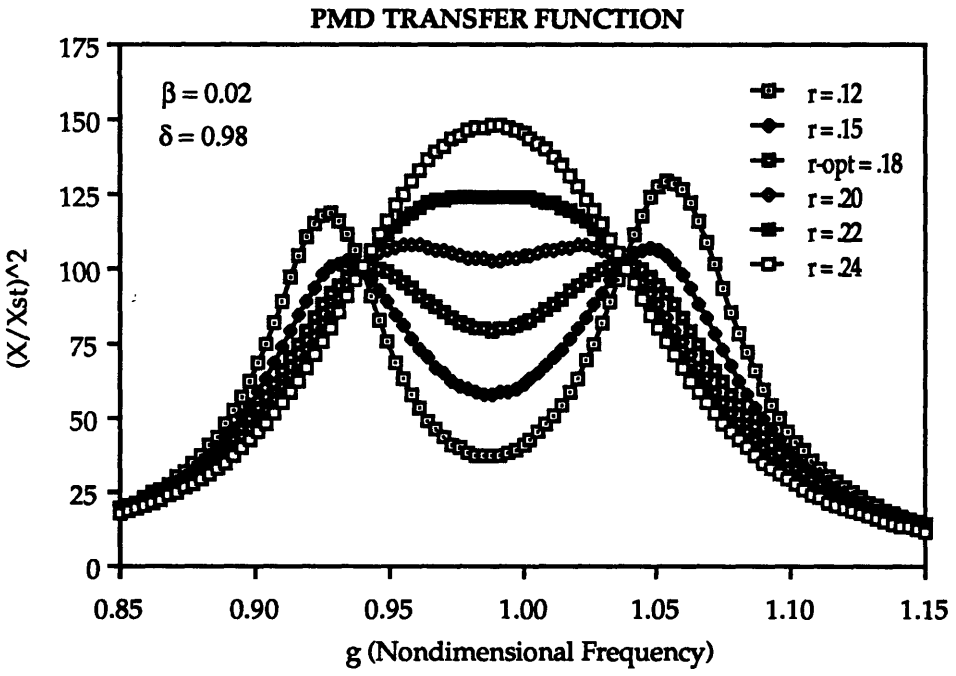

Figure 3.5 Transfer Function of PMD Damped System at the Optimum Tuning Ratio and Various Values of the PMD Internal Dissipation

An alternative method for determining the optimum PMD damping is described in Ref [5]. It entails finding the value of the damping which is associated with the coalescence of the two system modes, i.e. the point of furthest left excursion for the system poles in the s-plane. This technique yields a higher steady state system response. The optimal damping parameter in this respect is expressed as

$$r^2_{opt\text{-}pp} = \left[\frac{4}{\delta^2_{opt}}\right]\left[\frac{\beta}{(1+\beta)^3}\right] \tag{3.14}$$

There are thus two alternatives for choosing the "optimal" damping value for the PMD. The differences in the values tends to be small and so the second, simpler Equation (3.14) is often used.

As a summary, the PMD can be modelled as a complex point impedance which can be optimally tuned to give maximum energy dissipation to a mode of the base structure. The PMD is effective at damping over a very narrow bandwidth, and its effectiveness depends on 1) its mass relative to the mass of the structure and 2) the relative tuning of the spring and damper to the base structure.

3.3.1 Energy Based Reductions of Proof Mass Dampers

In this section an attempt will be made to model the amount of damping that resonant subsystem dampers actually introduce into the system modes. This modelling is complicated because the addition of resonant subsystems alters the frequency response of the system, introducing new modes and shifting the frequencies of others. Of course, these new system modes can be identified for their individual damping ratios, but this requires a complete analysis of the system with closely spaced modes every time a resonant damper is introduced. It would be useful to be able to simply evaluate the effect of the damper on the important modes of the system. With resonant dampers, difficulty can arise in evaluating the effects of mistuning on the damping levels of the modes since typically neither the system nor the damper parameters are known with certainty. It would

therefore also be useful to be able to evaluate the effects of mistuning on the performance of the PMD.

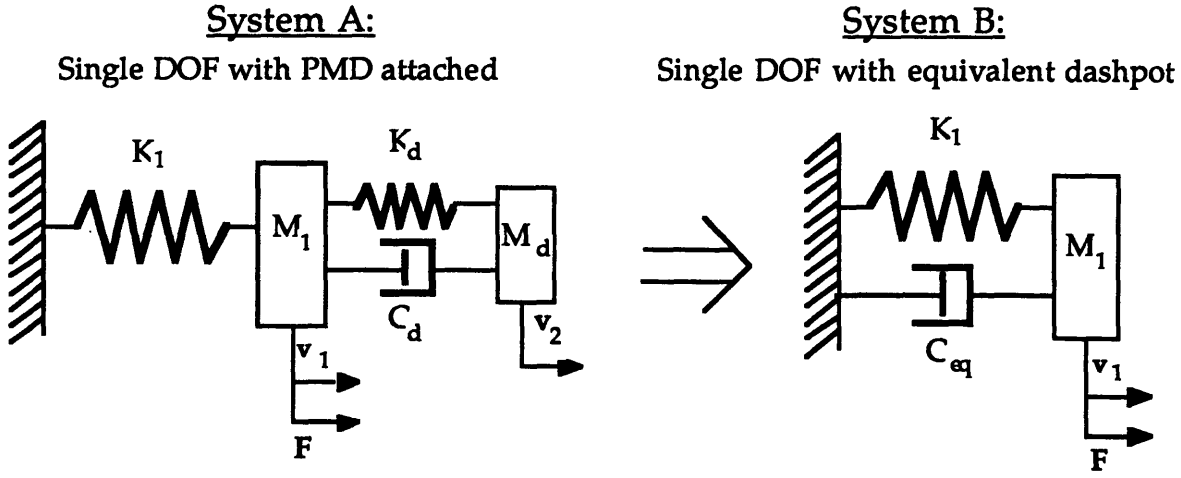

Figure 3.6 Standard Model of a 1-DOF System with an Attached PMD (A) and the Equivalent System with an Equivalent Dashpot (B)

One method of accomplishing these objectives is to model the resonant PMD in terms of the structural energy that it dissipates rather than the details of its effect on system response. This method involves conceptually replacing the PMD shown in System A of Figure 3.6 with a simple dashpot shown in System B which would dissipate the same amount of energy as the PMD. The dashpot damping will have frequency dependance but the natural frequency of the base system will remain unchanged. To do this, the energy dissipated in the PMD can be evaluated using Equation (2.35). Noting that only the dashpot built into the PMD in System A dissipates any energy, the average power dissipation in a cycle for an undamped system with a PMD as shown in System A of Figure 3.6 can be calculated using Equation (2.35).

$$\frac{E_{dis}}{T} = (v_1 - v_2)^* C_d (v_1 - v_2) \tag{3.15}$$

Where the superscript, *, denotes the complex conjugation. Since there was no external force on node-2, an expression can be found which was employed in the static condensation used to derive Equation (3.9) relating v_1 to v_2:

$$v_2 = \left[\frac{C_d + \frac{K_d}{s}}{sM_d + C_d + \frac{K_d}{s}} \right] v_1 \tag{3.16}$$

This expression can be substituted into (3.15) to give an expression for the energy dissipation in System A.

$$\frac{E_{dis}^{A}}{T} = C_d |v_1|^2 \left| \frac{sM_d}{sM_d + C_d + \frac{K_d}{s}} \right|^2 \tag{3.17}$$

In System B there is only a single dashpot in the base structure. Again using (2.35), the energy dissipated in System B can be written:

$$\frac{E_{dis}^{B}}{T} = C_{eq} |v_1|^2 \tag{3.18}$$

Now equating the energy dissipated in A to the energy dissipated in B and cancelling the amplitude of v_1 from both sides of the equation, the equivalent dashpot value can be found.

$$C_{eq} = C_d \left| \frac{sM_d}{sM_d + C_d + \frac{K_d}{s}} \right|^2 \tag{3.19a}$$

After nondimensionalizing in accordance with Equation (3.11)

$$C_{eq} = C_d \left| \frac{\gamma^2}{\gamma^2 + \delta^2 + \delta r \gamma} \right|^2 \tag{3.19b}$$

This equation exhibits the dependencies of the system damping on the PMD parameter values. For large values of C_d, the C_{eq} goes as $1/C_d$ since $r = C_d/M_d\omega_d$. For large values of the dashpot internal to the PMD, the total system damping actually decreases. This effect is evident in Fig. 3.5 which shows the dependance of system amplitude on the value of r. The equivalent dashpot in System B can be expressed as a system loss factor using the equivalence between loss factor and damping ratio for a single degree of freedom system

$$\eta_{1\text{-DOF}} = 2\,\zeta_{1\text{-DOF}}\,g \tag{3.20}$$

Where $g = \omega/\omega_n$ and ζ is traditionally defined

$$\varsigma = \frac{C}{2 M \omega_n} \tag{3.21}$$

Using these equations and the nondimentionalizations of Equation (3.11), Equation (3.19b) can be expressed as an effective loss factor for the base system. This expression gives some important insight into the frequency dependant effectiveness of the PMD.

$$\eta_{eff} = \beta r \delta g \left[\frac{g^4}{(\delta^2 - g^2)^2 + (r\delta g)^2} \right] \tag{3.22}$$

The effective loss factor of the PMD reflects the system energy that the PMD dissipates for frequencies which do not necessarily correspond to the tuning frequency of the PMD. The expression for the effective loss factor can thus provide information about the energy dissipation that the PMD provides to modes to which it is not properly tuned or which have resonant frequencies above or below the primary damped mode. The effective loss factor of the PMD is plotted as a function of frequency in Figure 3.7 for optimal values of the parameters to show the sensitivity of the PMD effectiveness to mistuning. Several things can be seen from Figure 3.7. First, η is very dependent on β, the mass ratio. The more massive the proof mass damper the more damping that can be introduced into the base system mode. This suggests a damping-added mass trade in designing damped systems. Secondly, the effect of the PMD drops off to zero very quickly with frequency below the damper tuning frequency. This implies that the modes below the PMD's tuning frequency will derive almost no benefit from its presence. Thirdly, the effectiveness of the PMD as a damper drops off rapidly to a small residual level for frequencies above the damper tuning. Thus there is some residual damping effect for modes above the damper tuning.

Some key values can be taken from (3.22). The first is the value of the damping at base system resonance, $g = 1$:

$$\eta_{eff\text{-}res} = \frac{\beta r \delta}{(\delta^2 - 1)^2 + (r\delta)^2} \cong \frac{\beta}{r\delta} \quad \text{for small } \beta \tag{3.23}$$

This formula is useful for preliminary damping estimates for systems with PMDs.

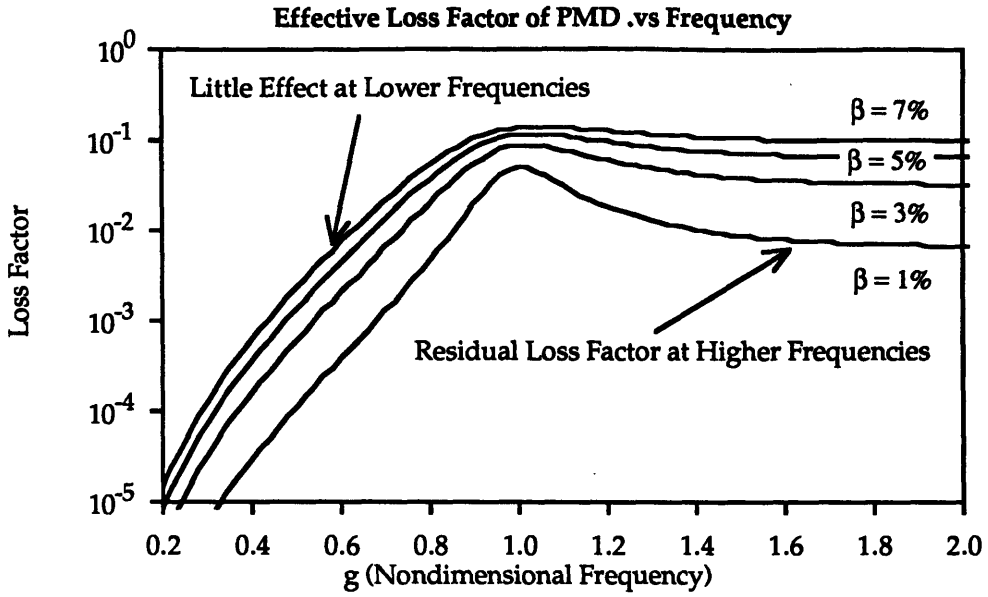

Figure 3.7 The Effective System Loss Factor vs. Nondimensional Frequency at Various Mass Ratios for an Optimally Tuned PMD

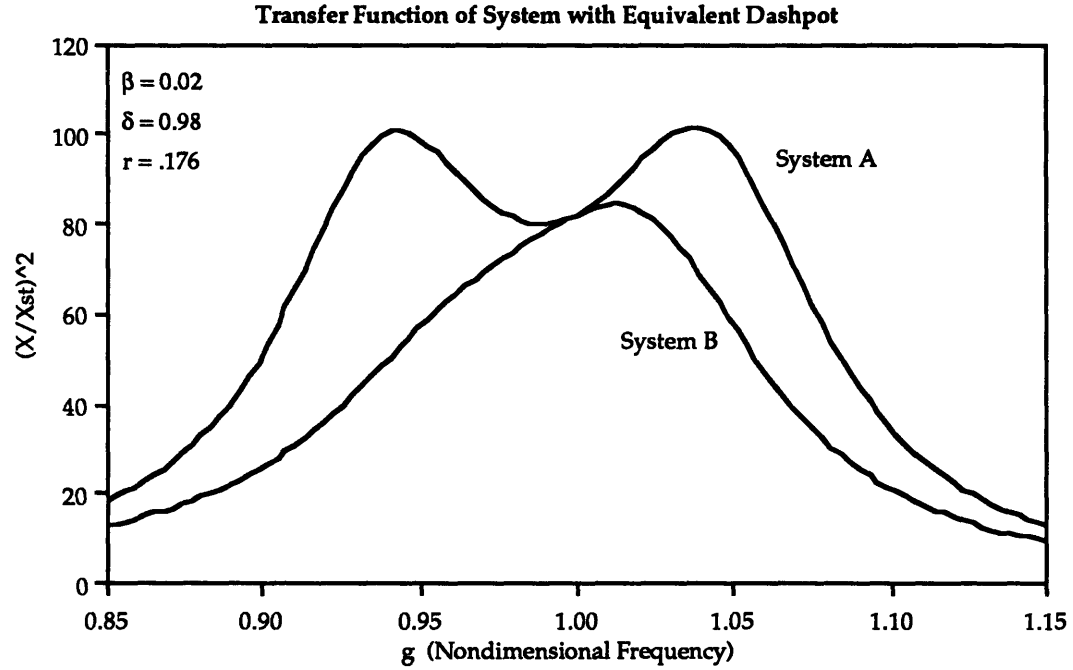

Figure 3.8 Transfer Function of a 1-DOF System with Attached PMD at Optimal Tuning (System A) Compared to the 1-DOF System with Equivalent Dashpot (System B)

The second value is the residual loss factor at frequencies much higher than the PMD tuning:

$$\eta_{residual} = \beta r \delta g \tag{3.24}$$

The optimally tuned response of System A and B are shown in Fig. 3.8. The equivalent energy reduction gives good estimates for the maximum amplitude of the system if not for the total system transfer function. This technique is because the transfer function value at resonance is typically determined only by the system damping. This technique of using an equivalent energy dissipation element for a resonant subsystems can be used as an approximate method for estimating the transfer function and damping of systems with attached PMDs or other resonant dampers.

3.4 Shunted Piezoelectric Dampers

3.4.1 Introduction

Another type of damping mechanism for structural systems uses piezoelectric materials within a passive network. Piezoelectric materials posses certain properties which make them useful as dampers or control elements for structures. The first is that they strain when an electrical field is applied across them. This property makes them well suited as actuators for control systems where the control signal is typically some voltage. The second is that they produce a voltage when they are strained. This property makes them well suited for sensing strain in structural systems. In general, piezoelectrics have the ability to efficiently transform mechanical energy to electrical energy and vice-versa. It is this transformational ability which makes them useful as elements in a damping network.

A typical piezoelectric and its constitutive relations is shown in Fig. 3.9. The fundamental constitutive relations are the relation between strain and applied field, known as the d constants, and between the charge density and the applied strain known as the g constants. Another fundamental property is the electromechanical coupling coefficient, k, which governs the energy transformation properties of a piezoelectric. The constants are explained in Ref. [21].

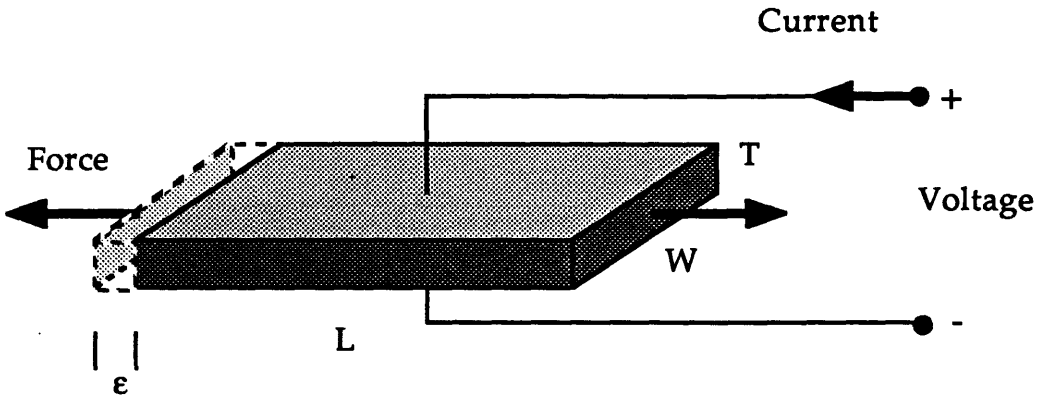

Figure 3.9 Assumed Geometry for a Typical Piezoelectric Material with the Top and Bottom Surfaces Electroded

In passive energy dissipation applications, the electrodes of the piezoelectric are shunted with some electrical impedance. Hence the term shunted piezoelectrics is used. The electrical impedance is designed to dissipate the electrical energy which has been converted from mechanical energy by the piezoelectric. If the shunting impedance is a resistor, the piezoelectric material exhibits frequency varying structural properties very similar to viscoelastic materials. If the shunting circuit is resonant, then the piezoelectric exhibits optimal tuning properties similar to the PMD. The advantage of using the piezoelectric and resonant circuit is that resonance is achieved with lightweight electronics instead of complex mechanical devices.

In the following sections the shunted piezoelectric's interaction with external circuits will be modeled, and the benefits that can be derived by passive circuit shunting of piezoelectrics will be quantified. First, the equivalent effective impedance of the shunted piezoelectric will be derived. This expression will then be applied to the cases of resistive and resonant circuit shunting. Expressions for the system damping will be derived, and parameters will be found which maximize this damping.

3.4.2 Modelling of Generally Shunted Piezoelectric Materials

Within the framework of systems analysis presented in Chapter 2, both mechanical and electrical systems can be represented as networks of frequency dependent impedances. The standard definitions of mechanical and electrical impedances and the correspondence between these used in the previous chapter:

Mechanical		Electrical
force	<=>	current
velocity	<=>	voltage

can be employed to derive the equivalent network model of the piezoelectric shown in Figure 3.10. The first step in the modelling is to note that the piezoelectric in Figure 3.10 is a two port element. There is one mechanical port and one electrical port. In parallel with the mechanical port through which the external forces act on the piezoelectric, there is the inherent mechanical impedance of the piezoelectric which consists primarily of the piezoelectrics stiffness. In parallel to the electrical port through which applied voltages act, there is an electrical impedance which consists primarily of the piezoelectrics inherent capacitance and any impedance shunted across the piezoelectric's electrodes.

The electrical and mechanical networks are linked by the piezoelectric effect. The core of the piezoelectric can be modeled as a transformer (more precisely, a gyrator since it converts an across variable, velocity, into a through variable, current) converting electrical energy into mechanical and vice-versa, Ref. [21]. The lossless transformation is defined by an equivalent "turns ratio", n, for the piezoelectric:

$$v_c(\omega) \cdot n = I_e(\omega) \tag{3.25a}$$

$$F_c(\omega) \frac{1}{n} = V_e(\omega) \tag{3.25b}$$

where v_c is the velocity across the mechanical side of the transformer, F_c is the force through the mechanical side of the transformer, I_e is the current through the electrical side of the transformer and V_e is the voltage across that electrical side. The turns ratio, n, is defined using the piezoelectric relation relating charge per unit area to strain, Ref [21]

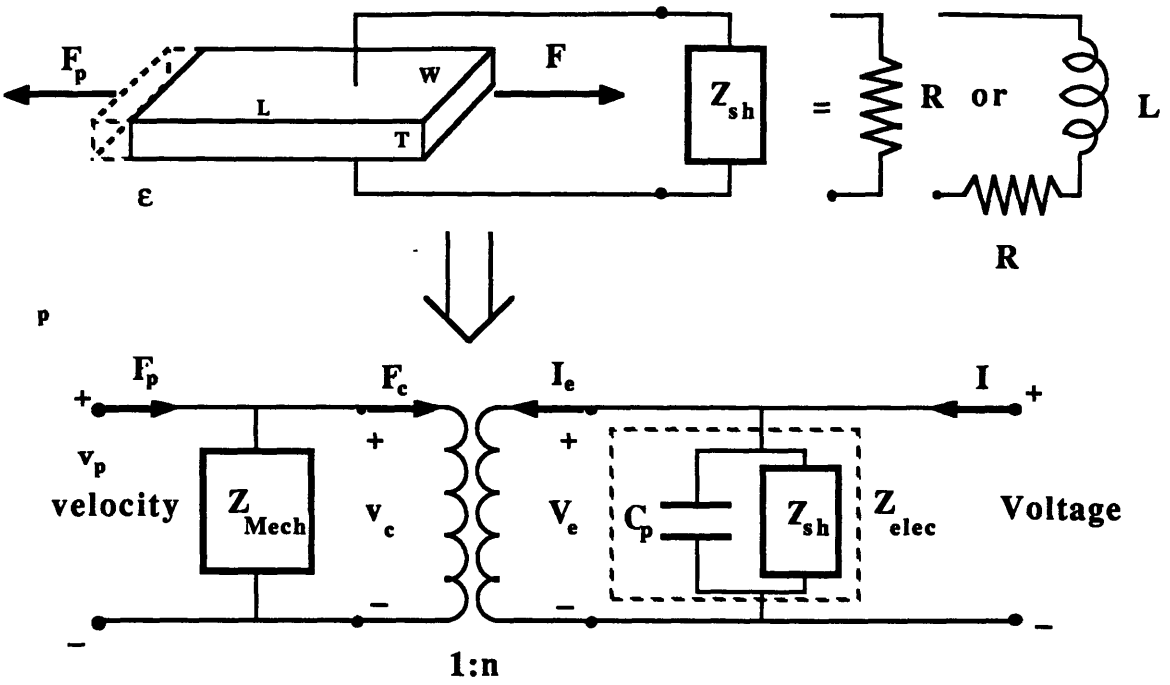

Figure 3.10 Physical Model of a Shunted Piezoelectric and its Network Analog Showing the Electrical/Mechanical Duality of a Piezoelectric and its Ability to Transform Energy from One System to Another

$$\frac{q_e}{LW} = \frac{1}{g_{31}} \varepsilon_1 \tag{3.26}$$

where q_e represents the charge on the piezoelectrics electrodes which is produce by a strain, ε_1; W is the width of the piezoelectric bar; and L is it's length. In the case shown in Fig. 3.10, the strain is in a direction perpendicular to the poling axis, the 1 direction, while the charge is developed such that the resulting field is parallel to the poling axis, the 3 direction. The g_{31} constant is the piezoelectric constant relating charge per unit area on the open circuit piezoelectric (not shunted) to the strain in the piezoelectric.

Equation (3.26) can be differentiated and compared to Equation.(3.25a) to give the "turns ratio" for the piezoelectric

$$n = \frac{W}{g_{31}} \tag{3.27}$$

At this point, an equivalent impedance for the piezoelectric shunted by any electrical circuit can be derived by applying Tellegen's Theorem to the

system in Fig. 3.10. The network which represents the piezoelectric consists primarily of two elements. The first is the element which represents the inherent mechanical impedance of the piezoelectric. Ignoring inertia terms, the mechanical impedance of the piezoelectric can be represented by the short circuited stiffness of the piezoelectric

$$Z^{sc}_{mech}(s) = E_{sc}\frac{TW}{LS} \tag{3.28}$$

where Z^{sc}_{mech} is the short circuit mechanical impedance of the piezoelectric which is based on the short circuit stiffness, E_{sc}. The short circuit stiffness is used to separate the effects of the electrical circuit from the inherent stiffness of the piezoelectric.

The second important element in the network that represents the piezoelectric is the equivalent electrical impedance of the circuit on the electrical side. Since the piezoelectric's surfaces are coated with a conducting layer, it will always posses some inherent capacitance which depends on the geometry and dielectric properties of the piezoelectric. The electrical impedance of the piezoelectric consists of this inherent capacitance combined with the electrical impedance of other components shunted across the piezoelectrics electrodes. Thus an expression for the total electrical impedance used in the network analysis is written:

$$Z_{elec}(s) = \frac{\frac{Z_{sh}(s)}{C_p s}}{\frac{1}{C_p s} + Z_{sh}(s)} \tag{3.29}$$

where C_p represents the inherent piezoelectric capacitance. Throughout the remainder of this chapter the subscript, $()_p$, will signify *piezoelectric* and not *port* as in Chapter 2.

The transformer does not appear in the system formulation using Tellegen's theorem because it neither stores nor dissipates energy. It therefore doesn't contribute to the summations over the elements. It will be useful to define a variable transformation, however. Finally, if the external force on the piezoelectric in Fig. 3.10, F_p, is thought of as an system port in parallel with the mechanical impedance, the network summation can be performed.

$$v_p{}^H F_p = v_p{}^H Z_{mech}(s) v_p + I_e^H Z_{elec}(s) I_e^H \tag{3.30}$$

where v_p, the velocity across the piezoelectric, is equal to v_c, the velocity across the transformer element, because the transformer is arranged in parallel with the mechanical impedance. The variable, I_e, which represents the current flowing through the electrical impedance is equivalent to the current generated by the piezoelectric under strain. It can therefore be eliminated using the transformer relation (3.25a). Finally, substituting the elemental impedances and cancelling v_p ,leads to an expression for the equivalent mechanical impedance of the piezoelectric

$$F_p(s) = \left[E_{sc} \frac{TW}{LS} + \left(\frac{W}{g_{31}} \right)^2 Z_{elec}(s) \right] \cdot v_p = Z_{eff}(s) \cdot v_p \tag{3.31}$$

The total electrical impedance is taken to be the shunting impedance in parallel with the piezoelectrics inherent capacitance, Equation (3.29). At this point, it is convenient to introduce the piezoelectric property known as the electromechanical coupling coefficient. It is defined as the ratio of the peak energy stored in the capacitor to the peak energy stored in the material strain with the piezoelectric electrodes open. Physically it represents the percentage of energy present in the mechanical strain which is converted into electrical energy and vice versa.

$$k_{31}^2 \equiv \frac{\frac{1}{2} q_e^2}{\frac{1}{2} E_{oc} \varepsilon_1^2 (LTW)} \tag{3.32}$$

Using Equation (3.26), this expression can be reduced to:

$$k_{31}^2 = \frac{LW}{E_{oc} g_{31}^2 C_p T} \tag{3.33}$$

Also, noting that :

$$Z_{elec}^{sc}(s) = \text{short circuit electrical impedence} = 0 \tag{3.34a}$$

$$Z_{elec}^{oc}(s) = \text{open circuit electrical impedance} = \frac{1}{C_p s} \tag{3.34b}$$

An expression to relate the open and short circuit stiffnesses of the piezoelectric can be derived by using (3.34b) and (3.31). First Equation (3.31) is

used to find the effective impedance of the piezoelectric when the electrodes are left open. The open circuit electrical impedance is substituted into (3.31) to give:

$$Z^{oc}_{eff}(s) = \frac{E_{oc}TW}{Ls} = \left[\frac{E_{sc}TW}{Ls} + \left(\frac{w}{g_{31}}\right)^2\left(\frac{1}{C_p s}\right)\right] \tag{3.35}$$

The expression for the electromechanical coupling coefficient, Equation (3.33) is then substituted into the electrical contribution to the impedance. Finally, the TW/Ls is cancelled from both sides of (3.35) to give the expression relating the open and short circuit impedances of the piezoelectric.

$$E_{sc} = \left(1-k_{31}^2\right)E_{oc} \tag{3.36}$$

This relation is the standard form for relating the short and open circuit stiffnesses (Ref. 3.8). It is directly derivable from the form of the effective impedance of the piezoelectric. Equations (3.28), (3.33), and (3.36) can be substituted into Equation 3.35 to give the final form for the piezoelectric effective impedance:

$$Z_{eff}(s) = Z^{sc}_{mech}(s)\left[1 + \frac{k_{31}^2}{1-k_{31}^2}\left(\frac{Z_{elec}(s)}{Z^{oc}_{elec}(s)}\right)\right] \tag{3.37a}$$

$$= Z^{sc}_{mech}(s)\left[1 + Z_{mod}(s)\right] \tag{3.37b}$$

where Z^{sc}_{mech} is defined in (3.28).

Thus, The impedance of the piezoelectric can be expressed as the product of its short circuit mechanical impedance (just a stiffness) and a nondimensional modifying term which reflects the effect of the electrical circuit shunting the piezoelectric's electrodes. The effects of the electrical circuits are modified by the electromechanical coupling coefficient, which limits the influence that the electrical portion of the circuit has on the effective impedance. The impedance derived in (3.37) can be thought of as an effective mechanical impedance since it relates velocity to force. The electrical terms therefore appear only as modifiers to the inherent mechanical stiffness of the piezoelectric. Since the impedance represented in (3.37) is

effectively only a stiffness, it can be expressed in the form commonly used for viscoelastic materials [Eq. (3.2)]:

$$E_{eff}(\omega) = E_0(\omega)[1 + i\eta(\omega)] \tag{3.38}$$

This reduction leads to frequency-dependent equations for the complex modulus of the shunted piezoelectric. Putting Equation (3.37) into the form of Equation (3.38) gives the frequency-dependant equivalent material properties for an arbitrarily shunted piezoelectric.

$$\eta(\omega) = \frac{\text{Imag}\left\{Z_{mod}(s)\right\}}{\text{Real}\left\{1 + Z_{mod}(s)\right\}} \tag{3.39a}$$

$$E_0(\omega) = E_{sc}\cdot \text{Real}\left\{1 + Z_{mod}(s)\right\} \tag{3.39b}$$

These equations, as well as (3.37), can be applied to arbitrary shunting conditions for parameter optimization of the material loss factor at a critical frequency. The expression for the effective impedance of the shunted piezoelectric can be used along with the impedances of the other damping devices in the frequency domain system analysis described in the previous chapter.

3.4.3 Resistive Shunting

One circuit which can be coupled to a piezoelectric is that of a resistor shunting the piezoelectric electrodes as shown in Figure 3.10. In this shunting geometry, the resister is placed in parallel with the inherent capacitance of the piezoelectric. The resistor provides a means of energy dissipation on the electrical side and thus should increase the total piezoelectric loss factor above the loss factor for the short or open circuited piezoelectric. Its exact effect on the stiffness and dissipation properties of the piezoelectric can be modelled by applying Equation (3.37). For the case of a resistor across the piezoelectrics electrodes, the total electrical impedance used in (3.37) is:

$$Z_{elec}(s) = \frac{R}{RC_p s + 1} \tag{3.40}$$

Inserting this into (3.37) gives the piezoelectric's effective mechanical impedance.

$$Z_{eff}(s) = \frac{E_{sc}TW}{sL}\left[1 + \frac{k_{31}^2}{1 - k_{31}^2}\left(\frac{RC_p s}{RC_p s + 1}\right)\right] \tag{3.41}$$

Since there are no internal resonances, it is convenient to use (3.39a) and (3.39b) to express (3.41) as a frequency dependent stiffness and loss factor. That is, the resistor can be thought of as changing the material properties of the piezoelectric into those of a lossy material similar to a viscoelastic in behavior. Using (3.39a) and (3.39b) to solve for nondimensionalized expressions for η and E gives

$$\eta_{res}(\omega) = \frac{k_{31}^2 \rho}{\left(1 - k_{31}^2\right) + \rho^2} \tag{3.42a}$$

$$E_0(\omega) = E_{sc}\left[1 + \left(\frac{k_{31}^2}{1-k_{31}^2}\right)\left(\frac{\rho^2}{1 + \rho^2}\right)\right] \tag{3.42b}$$

Where ρ is the nondimensional frequency.

$$\rho = RC_p\omega = \frac{\omega}{\omega_d}\text{, nondimensional frequency} \tag{3.42c}$$

These relations have been plotted versus ρ, the non-dimensional frequency (or the nondimensional resistance) in Figure 3.11 for k_{31} = 38%. These curves bear a marked similarity to the equivalent material curves for a standard linear solid. Two things are obvious from the graph. First, for a give resistance the stiffness of the piezoelectric changes from its short-circuit value at low frequencies to is open-circuit value at high frequencies. The location of this transition is determined by the shunting resistance. Secondly, the material exhibits a maximum loss factor at this transition point. By preforming an optimization, the location of this point of maximum loss factor can be found to be:

$$\rho_{opt} = R_{opt}C_p\omega = \sqrt{1 - k_{31}^2} \tag{3.43}$$

which yields:

$$\eta_{opt} = \frac{k_{31}^2}{2 \cdot \sqrt{1-k_{31}^2}} \tag{3.44}$$

Thus by appropriate choice of resistor, the peak of the loss factor curve can be moved to the desired frequency. It should be noted that the loss factor curve takes the same form as the Zener curve for material damping but can lead to material loss factors as high as 8.2% for commonly available piezoelectric materials with coupling coefficients as high as 38%. This compares favorably to the results obtained in Ref. [22] for the effective material loss factor for a resistive shunted piezoelectric. While these loss factor levels are not as high as those for viscoelastics, the piezoelectric material (typically a ceramic) is much more stiff than a viscoelastic and thus stores more strain energy. The net effect is that in most structural cases shunted piezoelectrics will provide higher total structural damping levels. These results for the resistive shunted piezoelectrics have been validated experimentally and will be presented in a later section.

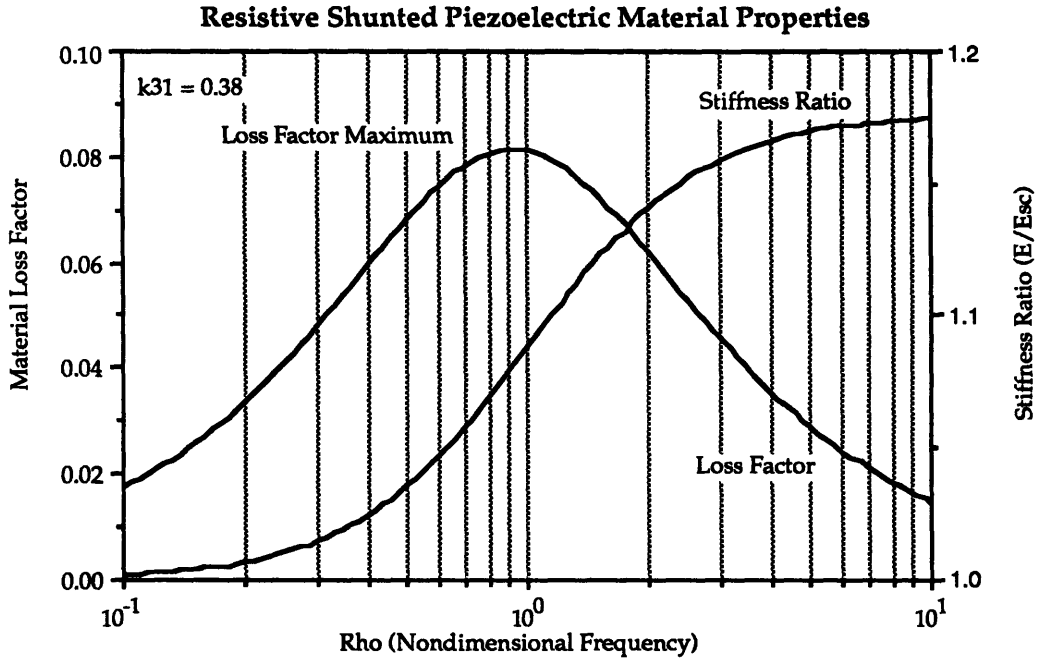

Figure 3.11 Effective Material Properties of a Resistive Shunted Piezoelectric

3.4.4 Resonant Circuit Shunting

Another case of interest is to create a resonant circuit by shunting the inherent capacitance of the piezoelectric with a resistor and inductor in series forming a LRC circuit for Z_{elec}. This circuit is shown in Fig. 3.10. This resonant electrical circuit can be tuned to a mode of the underlying mechanical system and thus greatly increase the attainable modal damping ratio in an effect similar to the classical proof-mass damper (PMD) presented previously.

With an inductor and a resistor in parallel with the piezoelectric's inherent capacitance, the total electrical impedance can be written:

$$Z_{el}(s) = \frac{Ls + R}{1 + RC_p s + LC_p s^2} \tag{3.45}$$

were L in the shunting inductance and R is the shunting resistance. This circuit is clearly resonant with some damping due to the resistance, R. Expression (3.45) can be substituted into (3.37a) and the resulting expression nondimensionalized to obtain:

$$Z_{eff}(s) = Z^{sc}_{mech}(s)\left[1 + \left(\frac{k_{31}^2}{1 - k_{31}^2}\right)\left(\frac{\gamma^2 + \delta r\gamma}{\gamma^2 + \delta r\gamma + \delta^2}\right)\right] \tag{3.46}$$

where the nondimensionalizations are defined relative to some arbitrary normalization frequency, ω_n

$$\omega_e = \frac{1}{\sqrt{LC_p}} = \text{electrical resonant frequency} \tag{3.47a}$$

$$\gamma = \frac{s}{\omega_n} \tag{3.47b}$$

$$\delta = \frac{\omega_e}{\omega_n} \tag{3.47c}$$

$$r = RC_p\omega_e \tag{3.47d}$$

Equation (3.46) is an expression of the effective mechanical impedance of a piezoelectric element shunted by a resonant circuit. This impedance can be included into the system framework described in the previous chapter for estimates of the total system loss factor. The key parameters of (3.46) are the

frequency tuning parameter, δ, and the damping parameter, r. These parameters are directly analogous to the ones used in the PMD nondimensionalization (Section 3.3, Equation 3.11). The δ parameter reflects the frequency to which the electrical circuit is tuned while the r parameter is an expression for the damping in that circuit.

There are several ways to determine the optimal parameters of (3.46) for energy dissipation. One of these involves treating the resonant shunted piezoelectric as a material with frequency dependant properties in a fashion analogous to the resistive shunting case. The expression for the effective impedance of the piezoelectric can be put into a complex modulus form such as (3.38). This leads to some very complex frequency dependant expressions for the material loss factor and stiffness.

$$E_{LRC}(\omega) = \frac{E_{sc}TW}{L}\left[1 + \left(\frac{k_{31}^2}{1-k_{31}^2}\right)\left(\frac{(\delta rg)^2 - g^2(\delta^2 - g^2)}{(\delta rg)^2 + (\delta^2 - g^2)^2}\right)\right] \tag{3.48a}$$

$$\eta_{LRC}(\omega) = \frac{k_{31}^2(\delta^3 rg)}{(\delta rg)^2 + (\delta^2 - g^2)^2 - k_{31}^2(\delta^2 - g^2)(1 + g^2)} \tag{3.48b}$$

where E_{LRC} and η_{LRC} are the effective material properties of the resonant shunted piezoelectric, and g is the real form of $\gamma(\omega/\omega_n)$. These expressions can be seen plotted in Fig. 3.12 for common values of the parameters. They can be useful in system modelling if the values of the parameters are already known. Both the effective material stiffness and the damping vary greatly with frequency and tuning parameter values, δ and r. This makes an optimization for energy dissipation difficult. The equations nonlinear dependance on the parameters also complicates matters. The actual energy dissipated is dependant on both E and η.

The problems associated with the parameter optimization can be greatly alleviated by observing certain key similarities between a system containing resonant shunted piezoelectrics (RSPs) and a system containing the previously analyzed PMD. The first step in this comparison involves an examination of the system topologies. Both systems are shown in Fig. 3.13 along with the equivalent impedance network for each. Both systems contain impedances for the mass and stiffness elements and both contain a single

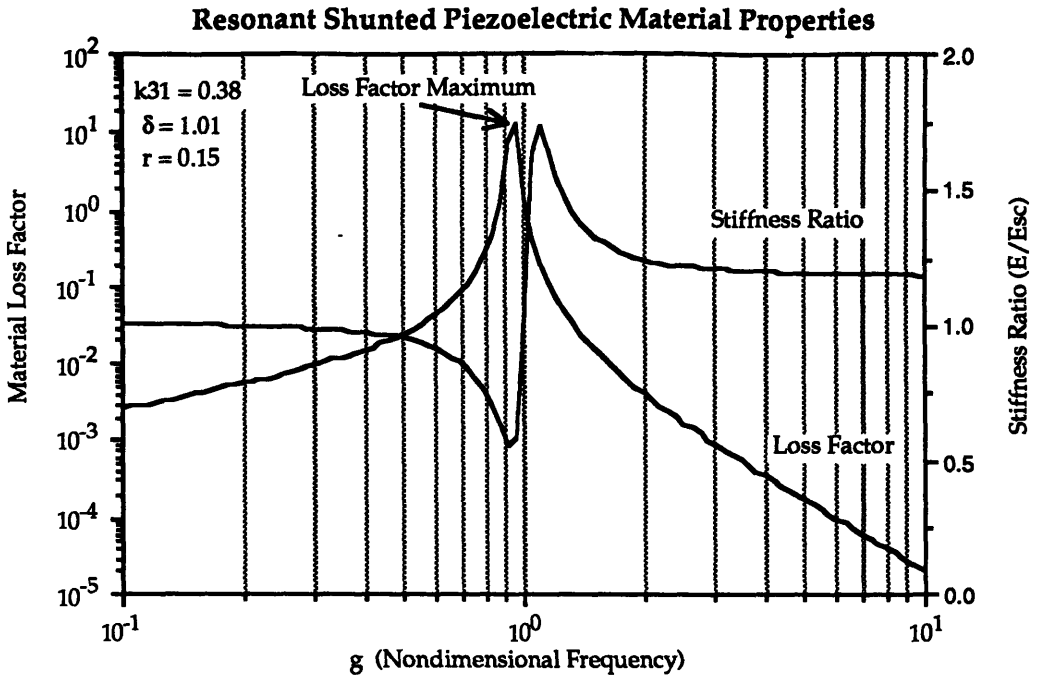

Figure 3.12 Effective Material Properties of a Piezoelectric Shunted by a Resonant LRC Circuit.

resonant impedance which acts as the damper. The damper impedances occupy corresponding locations in the network. This suggest that the method for obtaining the optimum parameters for the PMD can be applied to the RSP.

To determine the tuning and damping of the electrical subsystem which maximizes the damping in a mode of the piezoelectric's base structure, we must model the coupled system dynamics and draw analogies from the classical proof-mass damper. The derivation for optimal tuning and damping of the electrical circuit parallels the technique for determining the optimal tuning and damping ratio of a PMD as outlined in Ref. [18] and [19].

The mass and stiffness can be used to model the modal mass and stiffness of a multi-DOF system or any other equivalent system representation. Since the form of the impedance network for both the tuned piezoelectric and PMD cases is nearly identical, it is not surprising that the expressions for the system responses are similar. For the piezoelectric system the velocity at node-1 can be expressed

$$v_1(s) = \frac{F(s)}{Z_{mass}(s) + Z_{stif}(s) + Z_{RSP}(s)} \tag{3.49}$$

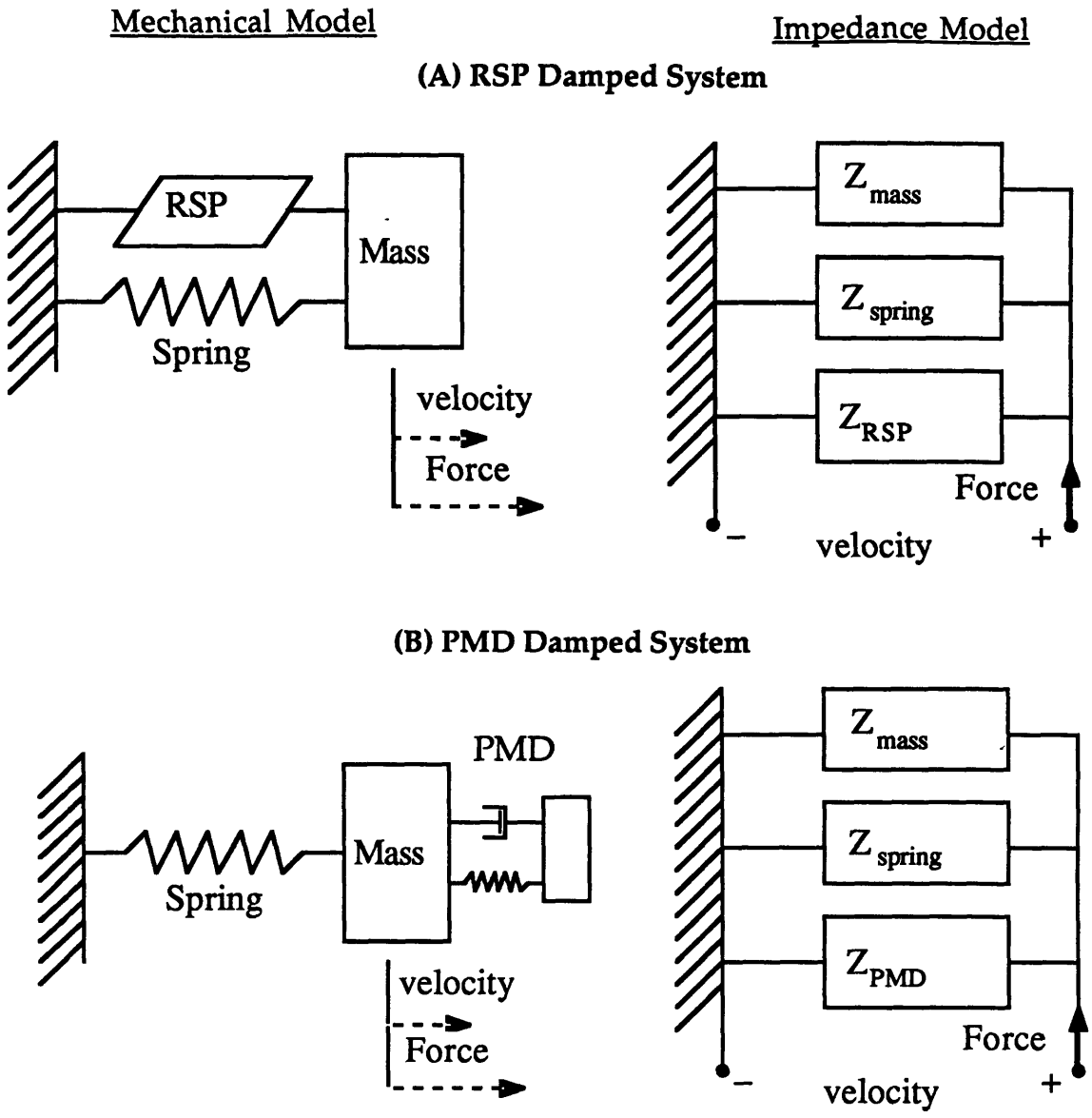

Figure 3.13 Comparison of Resonant Damper Topologies between an RSP Damped System (A) and a PMD Damped System (B)

Where Z_{mass} is the impedance associated with the base system mass; Z_{stif} is the impedance associated with the base system stiffness; and Z_{RSP} is the impedance associated with the resonant shunted piezoelectric. After reduction and nondimensionalization an expression for the position transfer function of a mechanical system with a RSP in parallel with the base system stiffness and a force acting on the mass can be found from (3.49):

$$\frac{x}{x_{st}} = \frac{\left(\delta^2 + \gamma^2\right) + \delta r\gamma}{\left(1+\gamma^2\right)\left(\delta^2+\gamma^2\right) + \left(1+\gamma^2\right)(\delta r\gamma) + K_{31}^2\gamma(\gamma+\delta r)} \tag{3.50}$$

where X_{st} is used for F/K_{tot}. The nondimensionalization is the same as that used in (3.47a) and (3.47b). with the substitution of the mechanical systems natural frequency for the normalization frequency used in (3.47). The generalized electromechanical coupling coefficient, K_{31}, is defined:

$$K_{31}^2 = k_{31}^2 \frac{K_{piezo}^{oc}}{K_{tot}} = k_{31}^2 \frac{K_{piezo}^{oc}}{K_{sys} + K_{piezo}^{sc}} \tag{3.51}$$

The generalized coupling coefficient reflects the fact that the piezoelectric is in parallel with some other stiffness. It is expressed as the normal electromechanical coupling coefficient multiplied by the ratio of piezoelectric open-circuit stiffness to total system stiffness with the piezoelectrics shorted.

For the tuned PMD, the transfer function expression equivalent to (3.50) is:

$$\frac{x}{x_{st}} = \frac{\left(\delta^2 + \gamma^2\right) + \delta r\gamma}{\left(1+\gamma^2\right)\left(\delta^2+\gamma^2\right) + \left(1+\gamma^2\right)(\delta r\gamma) + \beta\gamma^2\left(\delta^2 + \delta r\gamma\right)} \tag{3.52}$$

By comparing the form of these two equations, (3.50) and (3.52), it becomes clear that the generalized electromechanical coupling coefficient for the tuned piezoelectric case, K_{31}, serves the same function as the mass ratio, β, in the PMD case.

Two techniques for determining the "optimal tuning criteria will be presented. The first technique parallels the min-max criteria (presented in Ref. [18] for PMDs as well as Section 3.3 of this chapter) for minimizing the maximum of the system transfer function by appropriate choice of the RSP parameters. This technique will be referred to as transfer function optimization, and the optimal parameters will have the subscript, $()_{TF}$. The second technique will depend on pole placement techniques to choose system pole locations which maximize the magnitude of the real part of the system roots. The optimal parameters using this technique will bear the subscript, $()_{PP}$, to signify pole placement.

At this point the optimal tuning ratio using the first technique can be found by duplicating the argument for the PMD in Ref. [18]. The first step in this process is to find the magnitudes of the transfer functions which correspond to r = zero and r = infinity respectively. From (3.50) we can obtain for r = 0

$$\left|\frac{x}{x_{st}}\right|_{r=0} = \left|\frac{\delta^2 - g^2}{(1-g^2)(\delta^2 - g^2) - K_{31}^2 g^2}\right| \tag{3.53a}$$

and for r = infinity

$$\left|\frac{x}{x_{st}}\right|_{r=\infty} = \left|\frac{1}{(1 + K_{31}^2) - g^2}\right| \tag{3.53b}$$

These two transfer functions can be equated and a quadratic expression found for the intersection points, called the S and T points in the PMD analysis. This expression is

$$\delta^2\left(\frac{2 + K_{31}^2}{2}\right) - g^2\left[(1 + K_{31}^2) + \delta^2\right] + g^4 = 0 \tag{3.54}$$

From the quadratic formula, the sum of the roots of this equation can be found to be

$$g_S^2 + g_T^2 = \frac{-B}{A} = (1 + K_{31}^2) + \delta^2 \tag{3.55}$$

Equation (3.53b) can be solved for the magnitudes at the S and T points. This gives another expression for the sum of the two roots.

$$g_S^2 + g_T^2 = 2(1 + K_{31}^2) \tag{3.56}$$

Equating (3.55) and (3.56) leads to an expression for the tuning ratio which equalizes the magnitudes of the S and T points. This is the optimum tuning ratio.

$$\delta_{opt\text{-}TF} = \sqrt{1 + K_{31}^2} \tag{3.57}$$

Since K_{31} is always positive, this equation implies that the electrical resonator should always be tuned above the structural mode to be damped as opposed to tuning below as in the PMD case.

Once the optimal tuning has been found using the transfer function criteria, there are several methods for determining the "optimal" damping in the electrical circuit. One method entails setting the amplitude of the system transfer function at the frequency to which the resonant electrical circuit is tuned to the amplitude of the transfer function at the invariant frequencies, the S and T points. The frequency corresponding to the electrical tuning occurs at $g = \delta$. The amplitude of the S and T points can be found by first solving Equation (3.54) for the S and T frequencies. The roots of (3.54) are:

$$g_{S,T}^2 = (1 + K_{31}^2) \pm \sqrt{\left(\frac{K_{31}^2}{2}\right)\left(1 + K_{31}^2\right)} \tag{3.58}$$

This expression can be substituted into (2.53) to yield the amplitude at S or T.

$$\left|\frac{x}{x_{st}}\right|_{S,T} = \left| \frac{1}{\sqrt{\frac{K_{31}^2}{2}(1 + K_{31}^2)}} \right| \tag{3.59}$$

Evaluating the system transfer function, Equation (3.50), at $g = \delta$ and setting this amplitude equal to (3.59) gives an equation that can be solved for a simple expression for the "optimal " circuit damping:

$$r_{opt\text{-}TF} \cong \sqrt{\frac{2K_{31}^2}{1 + K_{31}^2}} \tag{3.60}$$

The subscript, opt-TF, signifies that this expression was derived from transfer function consideration. The effect of various circuit resistor values at optimal tuning is shown in Figure 3.14.

The second technique for determining the optimal tuning parameters is based on s-plane methods described in Ref. [5] for PMDs and outlined in Ref. [22] for piezoelectrics. The s-plane diagram in Figure 3.15 shows the root locus for the poles of the shunted piezoelectric system. Just as in the PMD case, as the damping parameter is increased the distinct poles can coalesce into double complex conjugate pairs *if* a special value of the frequency tuning parameter, δ, is chosen. This is the point of leftmost excursion in the s-plane described in Section 2.2. The method involves finding the value of the frequency tuning parameter, δ, and the damping parameter, r, which gives that point on the s-plane. The poles of the system are found from the

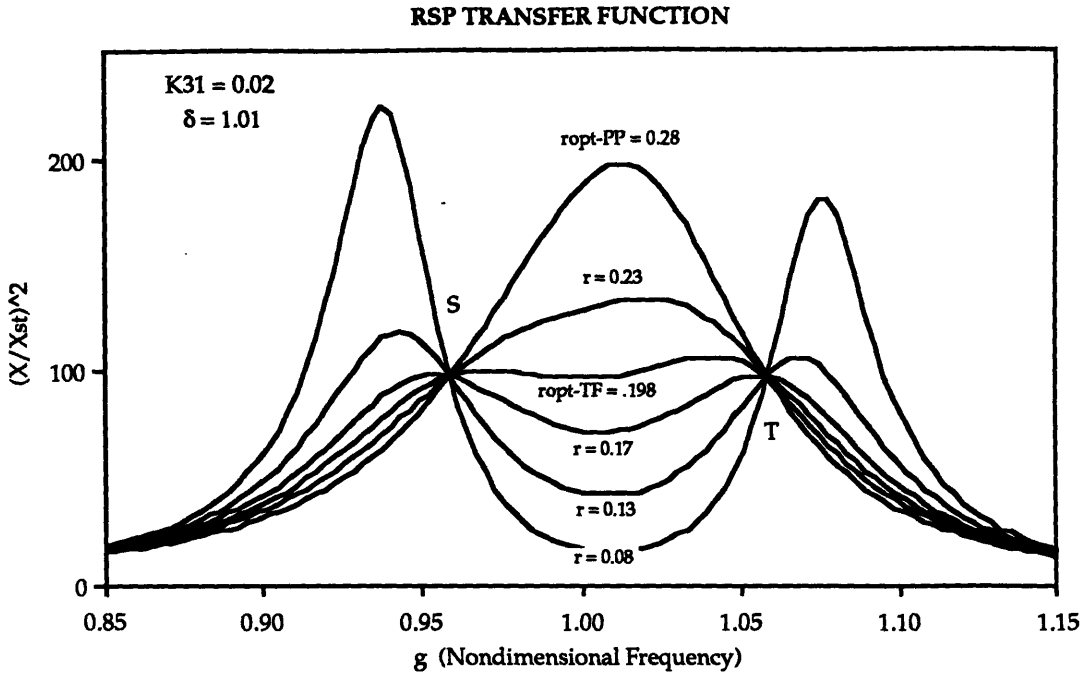

Figure 3.14 Transfer Function for a Single DOF System Containing a RSP at Various Values of the Damping Parameter, r

denominator of Equation (3.50). Assuming the coalesced poles are located at the coordinates, s = a + ib, a - ib, a series of equations for a and b can be found by equating corresponding terms of the characteristic polynomial found in the denominator of (3.50).

$$\delta r = -4a \tag{3.61a}$$

$$(1 + \delta^2) + K_{31}^2 = 6a^2 + 2b^2 \tag{3.61b}$$

$$\delta r\,(1 + K_{31}^2) = -4a\,(a^2 + b^2) \tag{3.61c}$$

$$\delta = a^2 + b^2 \tag{3.61d}$$

These equation can be solved for the parameters, r and δ, to give the value which results in the coalesced poles:

$$\delta_{opt\text{-}PP} = 1 + K_{31}^2 \tag{3.62a}$$

$$r_{opt\text{-}PP} = 2\sqrt{\frac{K_{31}^2}{1+K_{31}^2}} \qquad (3.62b)$$

The subscript, opt-PP, has been used to signify that the expressions were derived from pole-placement considerations. The transfer function corresponding to optimal tuning and this value of r is shown in Figure 3.14. This method tends to give higher steady state responses than the first method presented.

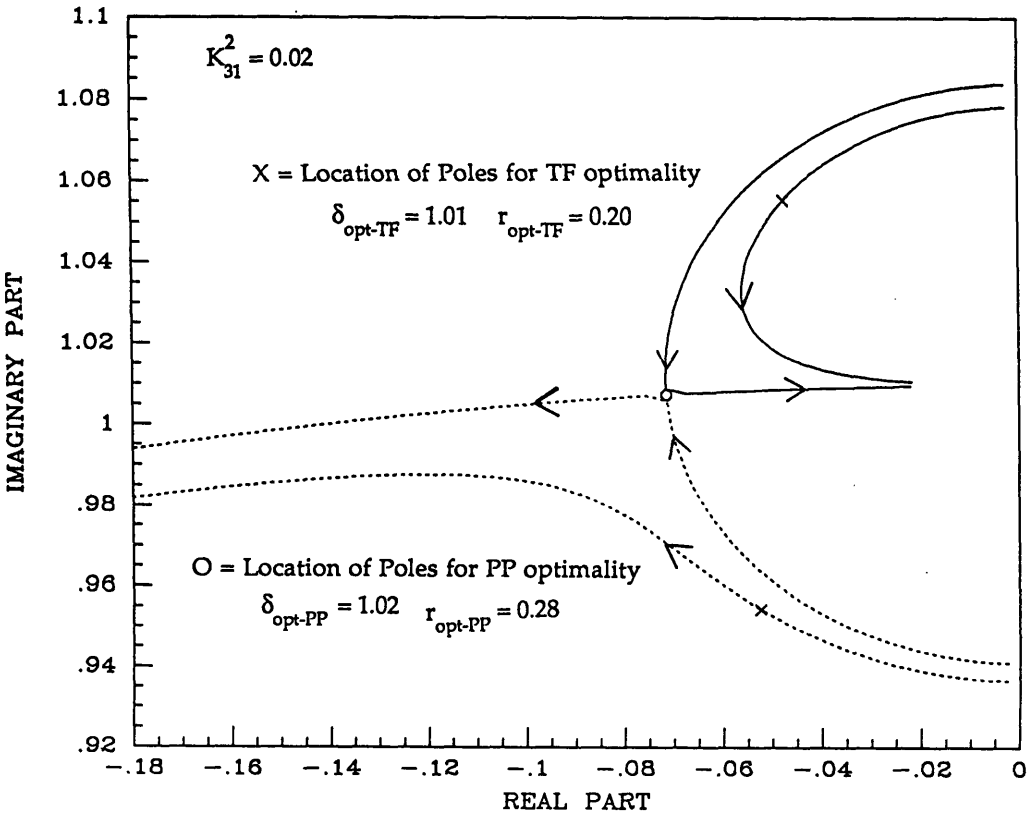

Figure 3.15 Root Locus for a RSP Damped System at 2 Values of δ as a Function of the Damping Parameter, r, Showing the Pole Locations for the Pole Placement (O) and Transfer Function (X) Optimal Tunings

As a practical point the various damper tuning criteria are indistinguishable in all but the most sensitive experimental setups. The ratios given for optimal tuning and electrical damping can now be used to add maximum damping to targeted structural modes in a fashion analogous to the PMD. Use of a tuned circuit can increase the structural mode damping

several orders of magnitude above simple resistive shunting. The discussion of the experimental validation of these concepts is presented in Chapter 5.

A technique has been developed to model piezoelectric materials shunted by an electrical circuit. A model for general shunting was developed and applied to the cases of resistive and inductive circuit shunting. The optimal parameters for maximizing total system loss factor (or damping ratio) were derived for these cases. Great benefits for base system energy dissipation can be attained by shunting the electrodes of the piezoelectric material. The energy transfer from the mechanical to electrical parts is governed by the generalized electromechanical coupling coefficient and can be enhanced by using tuned circuits.

3.5 Conclusions

In this chapter, the impedance models for three types of damping mechanisms where developed. Models were developed for viscoelastic materials, the classic proof mass damper, and shunted piezoelectric materials. These models were developed in the frequency domain for incorporation into the system models developed in Chapter 2. Expressions for the loss factor attainable for each method were developed as a basis for comparison of the three methods. These loss factors can be combined to determine the total system loss factors for systems incorporating these or various other types of damping methodologies. A typical system damping design methodology might include the following steps:

1) Develop the global impedance matrix for the system by assembling the system components using the framework described in the previous Chapter 2.
2) Select an approximate undamped system modeshape to be used in the approximate systems analysis.
3) Incorporate the selected damping impedances into the global system model. The damping impedances for the more common and effective damping methodologies are presented in this chapter.

4) Calculate the approximate system frequencies and damping using the undamped modeshape and Equations (2.45) and (2.50).
5) If the approximate values meet the desired design criteria preform a complete eigenanalysis on the damped system by solving (2.43) for the eigenvalues. If the design criteria are not met choose a new damping arrangement and repeat Step 3 above.

By examining this methodology it can be seen that all the necessary elements of a unified framework for evaluating and calculating the effect of various damping schemes on a structure have been developed. The damper impedance contains information necessary to calculate both the damper's effects on the structural damping and its effects on the structural natural frequencies. Therefore, the frequency domain system modelling is ideally suited for the analysis of damped systems.

Chapter 4
Experimental Design

4.1 Overview

In this chapter the hardware developed for the experimental program will be discussed. This hardware falls into three categories: the underlying structure to be tested, the actuators/dampers used to implement the damping schemes, and the electronics necessary to support these dampers and gather data for the investigation. The experiment had two main goals: to provide actual data on the implementation of damping enhancement schemes on a representative structure; and to test the utility of the frequency domain systems analysis in modelling damped structures.

To accomplish these goals, a representative test structure was constructed upon which damping enhancement schemes were implemented. The structure was designed to be representative of a general space structure and realistic enough to provide data on the practical aspects of damping enhancement. On the other hand, it had to be simple enough to make the results general and comparable to other structures. To meet these requirements, a dynamically isolated truss structure was constructed which provided the low inherent damping levels desirable for a damping enhancement testbed. The details of this testbed design will be presented in Section 4.2.

Two types of damping enhancement schemes were implemented on the experimental truss. They were both resonant damping systems. These systems are the classical proof mass damper and the resonant shunted piezoelectric described in Chapter 3. These methods were chosen because they provide the highest amount of damping for a given mass. The resonant damping methodologies are mass efficient in the mode to which they are tuned. The design for the hardware used to implement these schemes is presented in Section 4.3.1. The PMD was implemented with a linear electromechanical driver using materials and construction designed to minimize weight. The resonant piezoelectric method was implemented using a novel piezoelectric truss member which could be inserted in the truss

in place of the standard members. The design for the truss member is also described in Section 4.3.2.

In order to facilitate the experiments, electrical circuits were constructed which enabled the resonant dampers to be tuned in the vicinity of the structural modes of interest. For the PMD, this circuitry employed a position and velocity feedback loop to create electrical stiffness and damping. Thus, the PMD parameters could be changed simply by changing the electrical gains in the circuit. The PMD was driven by a current source to simplify the design of the tuning circuitry. For the piezoelectric, the ability to tune the resonant behavior of the device in the vicinity of a structural mode of interest was achieved with the aid of a variable resistor and a partially variable inductor. This enable tuning of the resonant electrical shunting circuit. The design for this circuitry as well as the circuitry for the PMD is presented in Section 4.4. The data acquisition network is also presented in this section.

These three elements, the truss structure, the resonant dampers, and the support electronics, are components of the experimental setup presented in Fig. 4.1. They were designed to achieve the dual goals set forth earlier of ascertaining the effectiveness of damping enhancement mechanisms on space structures and testing the ability of the framework presented earlier to model space structure damping.

4.2 Truss Design

A truss was designed and constructed for use as a test bed for the damping enhancement schemes examined. The truss had to meet several requirements. First, the truss had to exhibit stable, low inherent damping levels. This was necessary so that the increase in damping due to the damping schemes would be easily measurable. Secondly, it was desirable to have a simple, understandable test structure so that physical insight could be used to easily interpreted the results. Balancing this requirement was the desire to test the damping schemes on a realistic structure in order to obtain data applicable to actual large complex structures.

To meet these requirements, the truss structure presented in Fig. 4.2 was constructed. The truss was constructed from commercial hardware available from MERO-Raumstruktur GMBH & Company, a display hardware

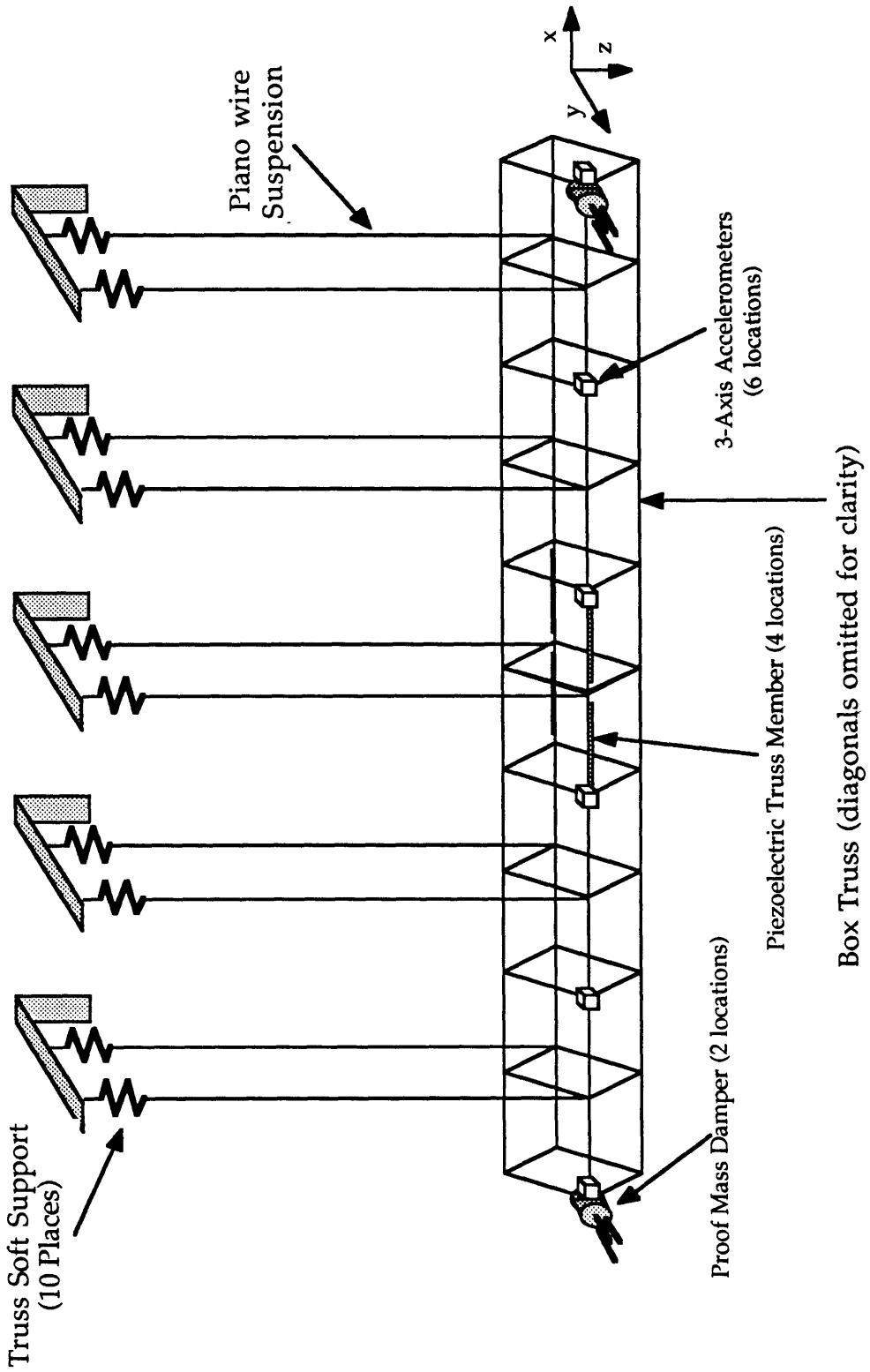

Figure 4.1 Truss Structure, Actuators, and Support Electronics

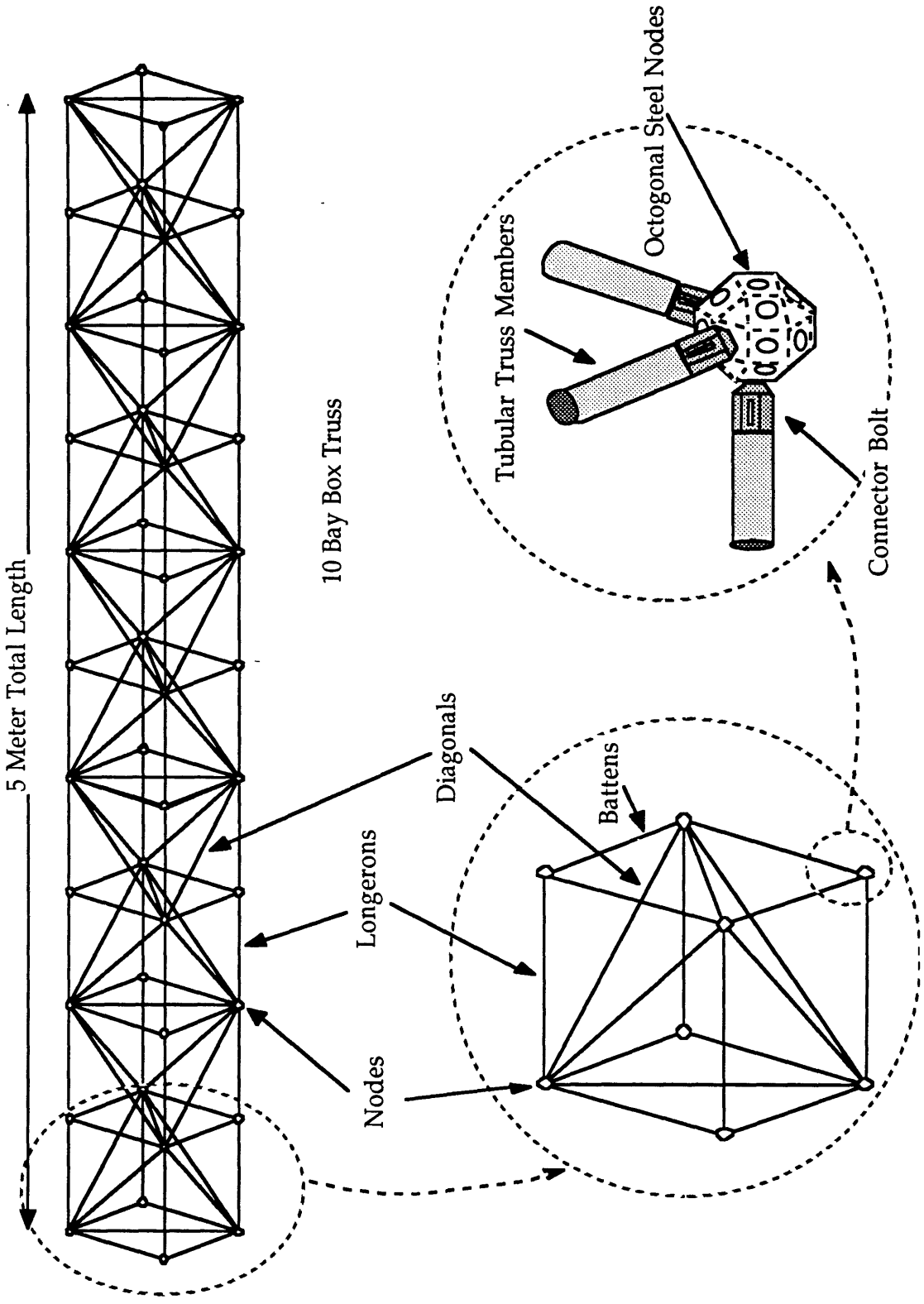

Figure 4.2 Truss Geometry Including Diagonal Arrangement and Member Connections

company headquartered in Wuerzburg, Germany. The total experimental truss length was 5 meters, consisting of 10 cubic bays of 0.5 meters. The bay geometry and internal diagonal positioning is shown in Fig. 4.2. The elements of the truss consisted of steel nodes and aluminum tubular members for the battens, diagonals, and longerons. The members bolt into the threaded nodes to create a tight, no-slop joint even under high excitation. The complete specifications of the test article can be found in Ref. [23]. The properties of the truss elements are presented in Table 4.1.

	Nodes	Battens & Longerons	Diagonals
Mass (Kg)	0.228	0.202	0.239
Stiffness, E (GPa)	See Note	68.8E9	68.8E9
Area (m^2)	NA	6.31E-5	6.31E-5
Total Length (m)	NA	0.500	0.707
Eff. Length (m)	NA	0.398	0.604

Note: The steel nodes were assumed to be rigid

Table 4.1 Properties of the Truss Elements

There were several design requirements on the resonant frequencies of the test article. It was desirable to maintain the overall truss frequencies as low as possible to better simulate a generic space structure. The design objective was also to insure that there were at least 3 structural modes below the natural frequencies of the individual truss members. The first bending mode of the tubular aluminum diagonals was estimated to be in the range from 220 to 300 hertz depending on the fixity at the nodes. In this range, the truss exhibits a multitude of closely spaced modes due to the element vibration, Ref. [24]. To avoid interacting with these modes the truss was designed to be as long as space permitted, 5 meters; and tubular elements with low cross sectional area but high bending stiffness were used. Low overall truss frequencies were also obtained by mass loading the truss. This was

accomplished by using steel nodes for the truss construction. The truss frequencies were predicted with a conventional finite element program, NASTRAN, and are presented in Table 4.2 for the baseline aluminum-member truss.

Mode		Frequency, ω_n (Hz)
1	Horizontal Bending	51.11
	Vertical Bending	51.22
	Torsion	73.84
2	Horizontal Bending	116.4
	Vertical Bending	116.9
	Torsion	143.9
3	Horizontal Bending	183.4
	Vertical Bending	185.8
	Torsion	208.7

Table 4.2 Initial Estimates of Experimental Truss Structure Natural Frequencies Based on a Finite Element Model

There were also several requirements on the suspension of the truss. Since data was desired on damping enhancement of a realistic space structure, unconstrained truss vibration was desirable to simulate the isolated environment of space. Since the truss was by nature a three dimensional article, the suspension should allow it to exhibit unconstrained motion in all six rigid-body degrees of freedom. The truss also had to be isolated from the external environment to prevent energy dissipation through the boundaries. To meet these requirements, a suspension system (Fig. 4.3) was constructed. The key design features are:

1) The truss is suspended from 10 locations by .010 inch diameter piano wire.
2) The wires are 2 meters long, giving truss horizontal pendulum modes < 0.35 Hz.

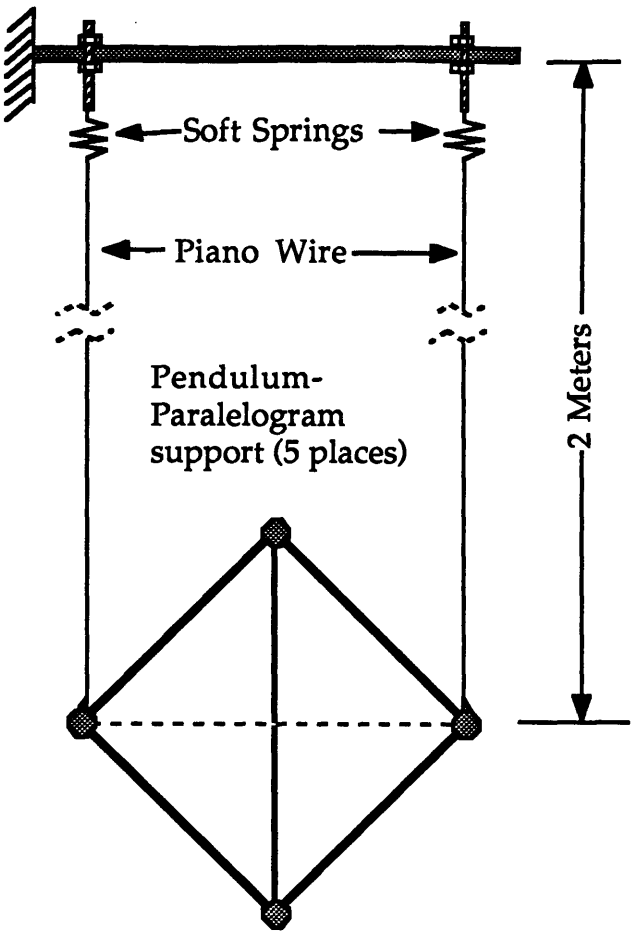

Figure 4.3 Truss Suspension System

3) The wires are connected to soft coil-steel springs to give a 1.2 Hz vertical bounce mode.
4) The support wires are adjustable to evenly distribute the truss weight among themselves, helping to eliminate support deformations and reduce the peak strain in the truss due to the support.

The frequency separation between the truss modes (first bending at 39 Hz) and the low bounce (1.2 Hz) and pendulum support modes (0.35 Hz) helped to dynamically isolate the truss from external interaction. The soft supports also allowed the truss to exhibit essentially free-free behavior in the modes of interest, the first three bending modes.

4.3 Damper/Actuator Design

In the experiments, two types of resonant damper methodologies were implemented. These were the classical Proof Mass Damper (PMD) and the Resonant Shunted Piezoelectric (RSP). Both these devices could also be employed as actuators to produce forces on the system. The PMDs were implemented with an electromechanical DC direct drive motor; and the RSPs were implemented with piezoelectric truss members. In the following sections, the design and implementation of these devices will be reviewed.

4.3.1 Proof Mass Damper Implementation

One of the damping methodologies tested involved the use of the classical proof mass damper. The analysis and conceptual model of this device was presented in Section 3.3. It involves a proof mass connected to a structure via a spring and a dashpot. The parameters of the spring and dashpot can in principle be tuned for maximum energy dissipation. The PMD actually implemented for damping enhancement experiments on the truss was a tunable electromechanical device.

The design of the PMD presented in Fig. 4.4 centers around several important components. The proof mass portion of the damper is made of a large rare-earth magnet and surrounding magnet iron. These components form the magnetic field and slide axially on linear bearings. This proof mass is connected to the structure by steel coil springs which give the entire damper some inherent mechanical stiffness. The stiffness of the mechanical spring is augmented by a position feedback circuit. This feedback circuit is presented in Section 4.4.2. The current passes through a coil located in the magnetic field, and thus produces a force which can be used by the position feedback to create an electrical spring. It is this electrical "spring" which allows the damper to be easily tuned to the structural modes. The dashpot of the classical PMD model is also provided in this implementation by electrical feedback. Velocity is measured by a velocity transducer and fed back to produce a velocity-dependant electrical force adjustable by the velocity feedback gain. This allows easy variation of the damping parameter, r, presented in Equation 3.11.

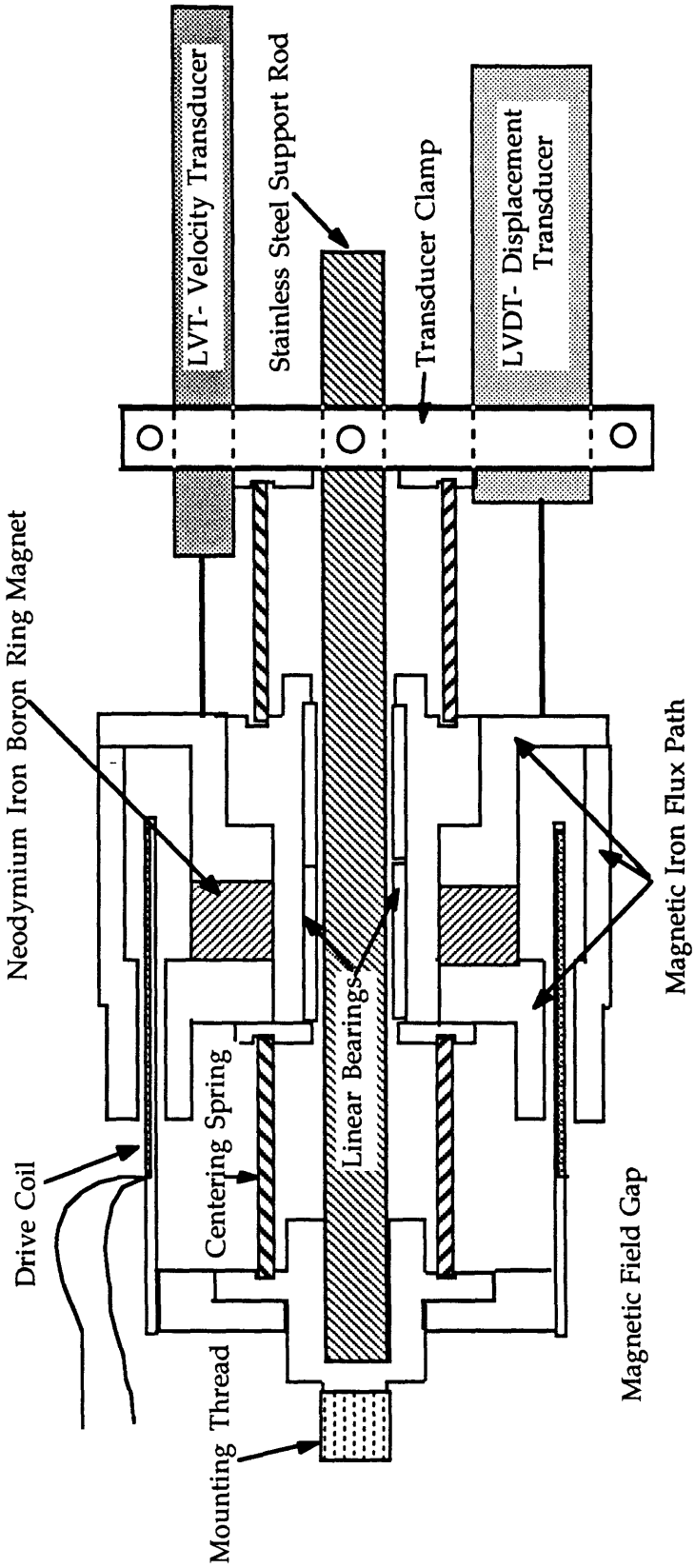

Figure 4.4 Proof Mass Damper Schematic showing Drive Coil, Proof Mass, and Sensors (to scale)

The heart of the PMD was a custom linear DC electric motor. A permanent field, linear drive DC motor consists of two main elements: a permanent magnet and surrounding magnetic material for the production of a uniform magnetic field; and a drive coil through which current passes to produce a reaction force against the magnetic field. The reaction force is proportional to the product of the magnetic field strength in Tesla, the net current flowing through the magnetic field coil, and the total length of coil wire in the field. The direction of this force is defined from the vector relation, Ref. [25]:

$$\vec{F}_{PMD}(\text{newtons}) = L_{tot}(\text{m})\, \vec{I}\,(\text{amperes}) \times \vec{B}_{PMD}(\text{Tesla}) \qquad (4.1)$$

were the cross symbolizes the vector cross product. With the drive coil circumferential and a radial magnetic field, Equation (4.1) results in a force in the axial direction proportional to the sign and magnitude of the drive coil current. This is the same principle of operation as a conventional acoustic speaker or dynamic shaker.

In the linear PMD implementation of Fig. 4.4, the drive coil was attached to the structure and the heavy magnet and magnetic material necessary to produce a radial field served as the proof mass. This use of the magnetic materials for the proof mass increased the PMD's mass efficiency.

The magnetic mass was supported by a stainless steel axial rod. The entire damper (except for the displacement and velocity transducers) was axially symmetric about this rod. The rod kept the magnetic field gap concentric with the drive coil. The proof mass was free to move along the axial rod on a set of precision linear bearings. The bearings were necessary to minimize friction between the moving proof mass and the rod. Both the rod and the matching precision bearings were manufactured by Thompson linear bearings. The bearings were models XA-61014. The precision 60 case stainless steal rod had a diameter of 3/8" with a .5 mil tolerance. This overall damper design is similar to the one used for the Langley inertial actuator, Ref [26].

The control force is produced on the structure by reaction with the proof mass through the spring and the electromagnetic force in the drive coil. The mass efficiency of the actuator hinges on the magnitude and extent of the magnetic field at the drive coil which can be produced for a given proof mass. The proof mass consists almost entirely of the permanent magnet and associated field conduction materials which concentrate the magnetic field

into the gap occupied by the drive coil. The magnet and magnetic conducting system can be thought of as a magnetic circuit conducting the magnetic field from the source, the permanent magnet, to the load, the coil gap. The actuators mass efficiency is optimized by minimizing the mass of this magnetic circuit for a given field in the gap.

An attempt was made to minimize the magnetic circuit mass in the implementation shown in Fig. 4.4 by the use of state-of-the-art magnetic materials and by maximum efficiency design of the magnetic circuit. In the magnetic circuit description, a permanent magnet can be thought of as a power source supplying magnetic power to a load, the gap. Just as an electrical source might have a maximum power output for a specified load, a permanent magnet has an optimum size of the gap to be filled with field. The gap and conducting path represent the load on the permanent magnet. The magnetic field, B, can be compared to the current in an electrical system. If the magnetic resistance is too great, then no magnetic current (B field) will flow to the gap; and thus no force will be produced on the drive coils. Using this circuit description and the properties of the permanent magnet, an optimum gap size and magnetic conduction path can be designed. The design of permanent magnet based magnetic circuits can be found in Ref. [27].

The total mass of the proof mass was minimized by use of high permeability magnetic materials for the conduction path and high energy permanent magnets. A Neodymium-Iron-Boron ring shaped rare earth magnet custom manufactured by Magnet Sales and Manufacturing Company was used as the core of the proof mass because of its high magnetic energy density. The permanent magnet was a ring with 2 inch outer diameter, 1 inch inner diameter, and an axial thickness of 0.5 inches. High permeability magnetic materials were used for the magnetic circuit conduction paths since they allow thinner magnetic field flux paths for a given magnetic resistance. The magnetic flux paths were machined out of CMI-C magnetic iron manufactured by Connecticut Metals Inc.. A comparison of the force to mass ratios for several similar linear actuators and commercially available linear dynamic shakers can be seen in Table 4.3. The present implementation can be seen to be much more mass efficient for producing a force on a structure.

		Hagood	NASA Ref. [26]	Miller Ref. [5]	Ling Model GWV
Actuator/PMD Type		Linear	Linear	Pivoting	Linear [1]
Proof Mass, M_{proof}(Kg)		1.39	0.24	0.17	1.59
Other Mass (Kg)		0.48	0.48	0.55	0.02
Total Mass, M_{tot} (Kg)		1.87	0.72	0.71	1.61
Peak Force, F_{max} (n)		22.24	4.40	1.36	17.60
Peak Current, I_{max} (amp)		5.06	2.00	4.92	2.40
Ratios	F_{max}/I_{max}	4.45	2.22	0.28	7.33
	M_{Proof}/M_{tot}	0.74	0.33	0.23	0.98
	F_{max}/M_{tot}	11.90	6.11	1.90	10.93

1: The Ling dynamic shaker cannot support its own weight in a 1-g environment

Table 4.3 Comparison of the Present Linear PMD Implementation with Similar Actuator Implementations

The gap which held the drive coils was dimensioned using the magnetic design rules referenced above. The gap was designed to be .156 inches wide radially with an average radius of 1.284 inches and a axial length of 1 inch. Once the gap size was set, the coil could be optimized to the parameters of a given drive amplifier so that the actuator produced the desired force with a bandwidth of 300 Hz.. The bandwidth of the force is limited by the amplifier voltage-current characteristics since at high frequency the coil acts as an inductor to limit the current flow. The length of the coil is set by the maximum stroke of the actuator at the peak operating force level at low frequencies. In this case, peak amplitude occurs at the resonance of the proof mass/restraining spring system with the amplitude of the proof mass as high as +/- .75 inches. The coil was set to 2.5 inches long and consisted of 2 layers of 24 gauge magnet wire.

The proof mass was centered on the coil by two steel springs. The springs provided the base stiffness for the PMD, creating a system with

resonance at 11 Hz. The remaining stiffness and viscous damping necessary to tune the PMD to the structural modes from 11 to 120 Hz were provided electrically via position and velocity feedback. The position was measured by a Trans-tek LVDT (linear variable displacement transducer), model 0243-000 mounted at the end of the central support rod and attached to the proof mass. The velocity was measured by a Trans-tek LVT (linear velocity transducer), model 0101-0000, mounted alongside the LVDT. Negative position and velocity feedback to the drive current (and thus force) provided electrical stiffness and damping proportional to their respective gains. The details of this tuning system will be discussed in Section 4.4.2.

The net result of these considerations was to produce a tunable mass efficient PMD which could be bolted to the truss nodes at almost any location in almost any direction. The PMD was simple and fit closely with the impedance model developed in Section 3.3. The device could be be used as both a classical proof mass damper with appropriate tuning or simply as a linear inertial actuator in its untuned state. If the coil current is determined by the position and velocity feedback then the device is operating like a tuned PMD. If, however, the the position and velocity feedback circuits are disabled and the drive coil current is commanded by an externally applied voltage, then the device is operating as an inertial actuator producing a prescribed force upon the structure. The PMD built was used as both a driver and separately as a damper in the experiments on the truss.

4.3.2 Piezoelectric Truss Member

The design and manufacture of the piezoelectric truss members used to implement the Resonant Shunted Piezoelectric (RSP) damping enhancement concept will be presented in this section. The use of piezoelectrics as resonant dampers after the addition of appropriate circuitry has been presented conceptually in Section 3.4.4. The implementation of this concept entailed the construction of piezoelectric strut members which replaced the standard aluminum strut members at key locations.

Four piezoelectric longeron truss members were manufactured to replace four members in the center 2 bays of the truss as shown in Fig. 4.5. The tubes were placed so as to best damp the first and third horizontal

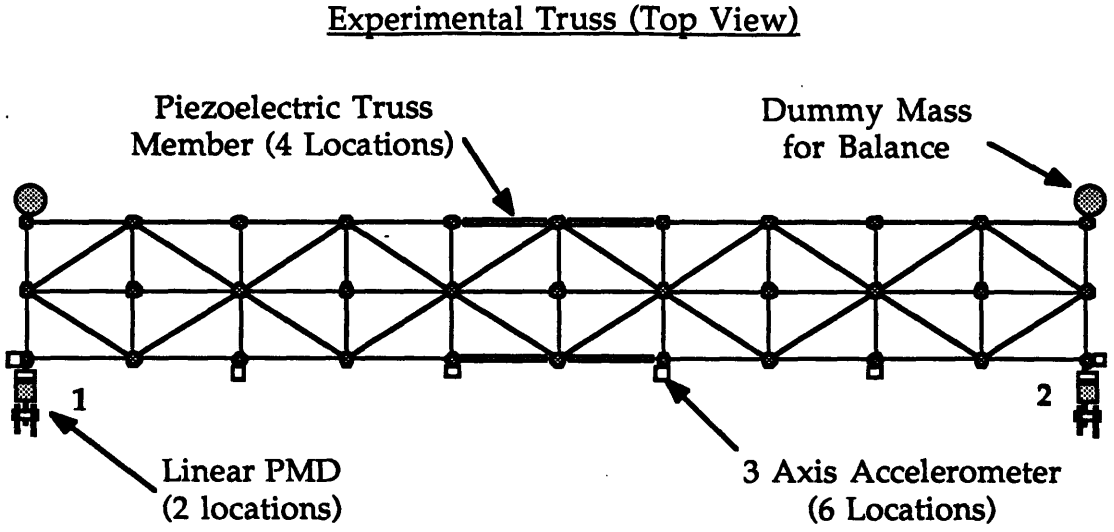

Figure 4.5 Locations of the Driver PMD (1), Damper PMD (2), and Piezoelectric Truss Members on the Truss

bending modes. The dampers would have little effect on the second horizontal bending mode since this mode has little strain energy in the central bays of the truss. The actuators can dissipate only the strain energy which is present in the piezoelectric. For this reason, the piezoelectric truss member was constructed so that most of its strain energy was focussed in the piezoelectric material.

The design of the piezoelectric consisted of three main elements. The first was a hollow piezoceramic tube extending the length of the member. This was the active portion of the member. The second element in the design was the fittings which attached to the ceramic stack and allowed the member to be connected to the truss in the same fashion as the aluminum members. The third element was the composite shell built up around the piezoceramic stack and endpieces to provide continuity and strength to the member. These elements are shown in the layout of the piezoelectric truss member shown in Fig. 4.6.

The active element of the member was the piezoelectric stack. The stack consists of five tubular piezoceramic tubes bonded together. The piezoceramic tubes were made with PZT-5H material from Vernitron Piezoelectric company. The individual piezoelectric tubes were 1.985 inches long with an outer diameter of 1 inch, and a wall thickness of .030 inches.

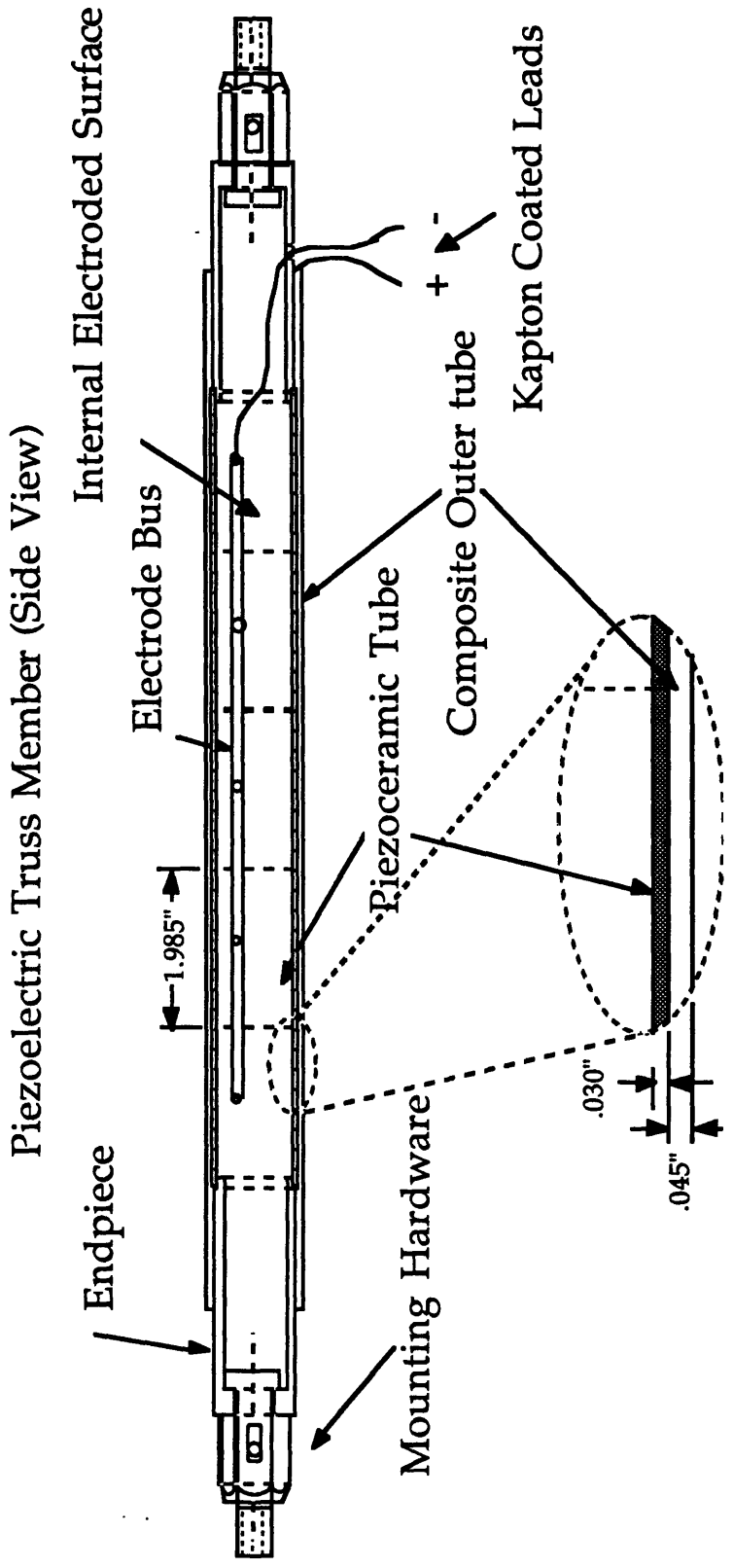

Figure 4.6 Piezoelectric Truss Member Schematic showing the Positioning of the Piezoceramic Tubes, the Composite Shell, and the Endpieces

Five tubular elements were bonded endwise to create a total piezoceramic stack 9.92 inches long. The individual cylinders are shown in Fig. 4.7. The wall thickness (.030 inches) made the individual piezoceramics very fragile. The cylinders were electroded on their interior and exterior surfaces and poled in the radial direction. Thus when a field was applied across the electrodes, the piezoelectric expanded axially in proportion to the d_{31} piezoelectric constant. There were also thickness and diameter changes.

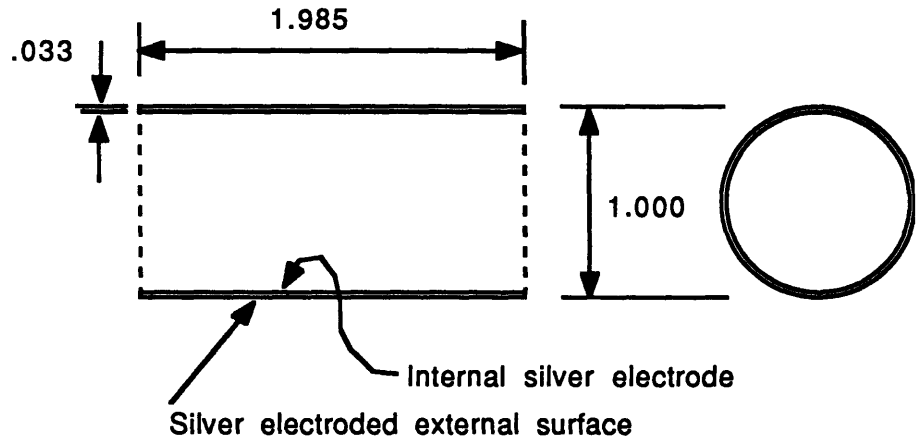

Figure 4.7 Dimensions of Typical Piezoceramic Tube Element

In the stack construction, the individual ceramic elements were aligned and bonded on a close fitting aluminum mandril. The internal and external electrodes were each electrically connected to common internal and external electrical busses. This enabled the entire stack to behave as one large piezoelectric tube electroded on its inside and outside surfaces.

This piezoceramic stack was then fitted with the specially machined aluminum endpieces shown in Fig. 4.8. The endpieces allow the truss member to be inserted in the truss by bolting to the nodes. The connecting hardware was identical to the connectors used in the standard aluminum members from Meroform. The conductive layers on the exterior and interior surfaces of the piezoelectric near the ends of the piezoelectric stack were then removed to avoid shorting to the truss through the aluminum endpieces. The stack and endpieces were then wrapped with a composite shell which coats the piezoceramics and edges of the endpieces. The shell used for the experimental truss members was glass/epoxy consisting of Owens-Corning

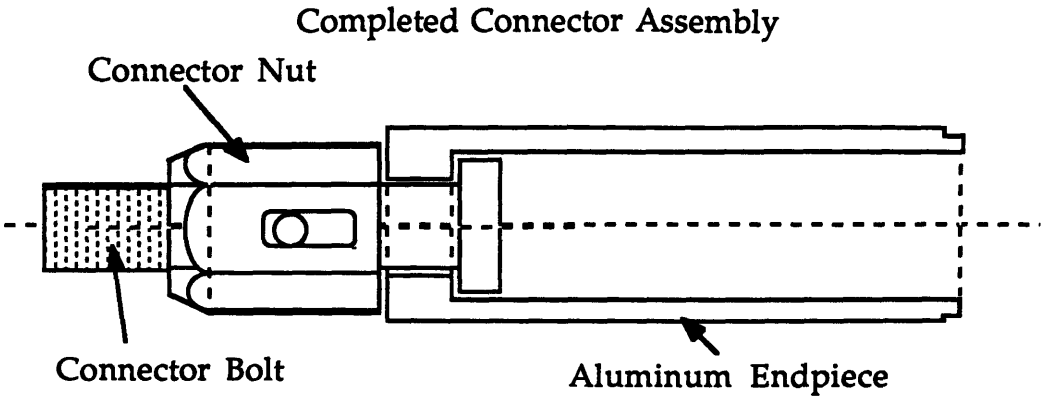

Figure 4.8 Piezoelectric Truss Member Connector Assembly showing the Aluminum Endpiece of the Ceramic Stack and the Bolt which Allows Truss Insertion

type 7781 Volan finish glass cloth with 0-90 fiber direction impregnated with Miller-Stephenson 871 epoxy resin. In the manufacture, a large rectangular piece of glass fiber cloth was cut so that, when the piece was rolled onto the piezoelectric stack, there would be 6 cloth plies with the fibers oriented axially and circumferentially about the piezoelectric tubes. The cloth was then impregnated with the epoxy and rolled onto the stack to a thickness of .045 inches. Glass-epoxy composite material was used for ease of manufacture and to prevent shorting between the truss and the external piezoceramic electrode which graphite fibers would cause. The wrapped member was allowed to cure at room temperature for 24 hours before use. The mass and stiffness properties for the piezoelectric truss member are presented in Table 4. The stiffness of the piezoelectric truss members is very close to the stiffness of the aluminum truss member.

It is important to understand the role that the composite shell plays in the piezoelectric truss member design. It serves primarily to increase the strength of the member but not the stiffness. The piezoelectric material is by nature very stiff and very brittle. On its own, it is unsuitable as a structural material. The addition of the composite tends to increase the fracture toughness of the member and thus make it useful as a structural member. The stiffness of the member is still primarily due to the piezoceramic (80% of the stiffness) since the composite (20% of the stiffness) tends to act only as a shear layer to convey stress across the defects in the piezoelectric material. This was discovered in the validation test for the piezoelectric truss members

	Piezoelectric Cylinder	Composite Shell	Endpieces	Total
Mass (Kg)	0.123	0.049	0.148	0.320
Stiffness, E (GPa)	60.6	9.7	rigid	29.47
Area (m^2)	6.47e-5	1.02e-4	NA	1.66e-4
Total Length (m)	0.252	0.252	0.248	0.500
Eff. Length (m)	0.252	0.252	0.00	0.252

Table 4.4 Breakdown of Piezoelectric Truss Member Properties

presented in the next chapter. The fact that the stiffness is primarily due to the piezoelectric indicates that most of the member strain energy resides in the piezoelectric material, which is important for damper effectiveness. The loss factor that can be achieved with the member is the sum of the loss factors for the ceramic and the composite weighted by the proportion of strain energy in each, Equation (3.1). The fact that most of the strain energy is in he piezoceramic leads to high electromechanical coupling coefficients and damper effectiveness.

These elements act together for an efficient application of piezoelectric elements to a truss structure. The damping is achieved by shunting an electrical impedance across the electrodes of the ceramic stack. In the resonant case this impedance is a resister and inductor which act with the inherent capacitance of the stack to produce a resonant LRC circuit. The parameters of this circuit can be tuned to a mode of the structure. This tuning and the electrical support which enables it is described in the following sections.

4.4 Electronic Measurement and Tuning Systems

In this section, the various electrical systems used in the experiment will be described. These systems include the structural sensing apparatus, the PMD drive and tuning circuitry, and the Resonant Shunted Piezoelectric's

(RSP) support circuitry. The support circuitry for the resonant devices consisted of state feedback circuits with variable gains. The gain calibrations are discussed in Chapter 5. The tuning circuits used for the resonant dampers were critical to damper performance.

4.4.1 Sensors for Truss Response

The truss was outfitted with 18 PCB Model 330A Accelerometers for structural response sensing and modeshape imaging. The accelerometers were organized into six 3 axis sets which were located on the truss as shown in Fig. 4.5. The accelerometers were extremely sensitive with a gain of 0.2 volts/g. With the amplifier system this rises to 1 volt/g. This provided excellent sensitivity for structural measurement.

4.4.2 Proof Mass Damper Electronic Support

There are two major elements to the PMD electronic support system. The first is a voltage controlled current source intended to drive the main PMD coil. The second is a position and velocity feedback loop necessary to provide the electronic "spring" and "damper" to tune the resonant devices. The design and function of these elements will be discussed here. The system architecture is presented in Fig. 4.9.

A voltage controlled current source was designed to drive a controlled current through the PMD coil. A Crown 300-IIA audio amplifier was used as the core of the design. It was converted to a current source by the introduction of high gain current feedback to the amplifier's input. The output current of the amplifier passes through a small (0.1 Ohm) sensing resistor where it creates a voltage proportional to the current. This voltage is amplified and subtracted from the input command signal to produce a negative current feedback loop. The system was marginally stable before a low pass rolloff at 1000 Hz was introduced. High current-feedback gains enabled this circuit to produce current signals which exactly tracked the input voltage with a bandwidth of 500 Hz. The loop gain of the voltage controlled current source was set via the feedback gains to 1.00 amperes per volt. The circuit schematic is shown in Figure 4.9.

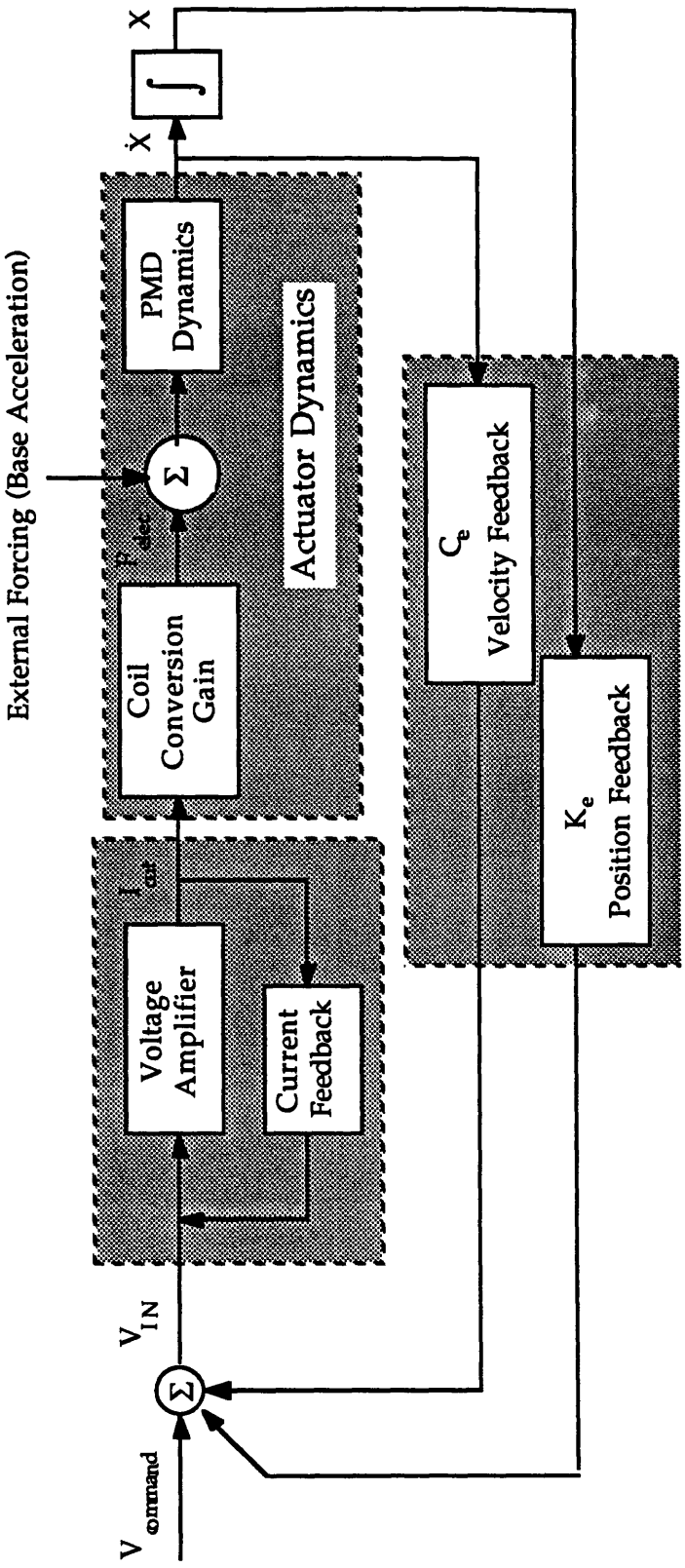

Figure 4.9 PMD Electronic Support Schematic showing the Use of Position and Velocity Feedback to Alter the PMD Dynamics

The purpose of this circuit was to eliminate the need to consider the effects of the coil and actuator dynamics in commanding the force produced by the PMD damper/actuator. The force is a direct function of the coil current. If the current is not controlled it can vary with both back EMF due to proof mass motion and coil impedance. The current servo eliminates the effects of back EMF and coil inductance on the force output and therefore simplifies the system dynamics. The transition from command voltage to applied force can now represented by a simple gain.

The tuning capabilities of the PMD are derived from a position and velocity feedback circuit shown in Figure 4.9. The LVDT and LVT described in Section 4.3.1 measure the position and velocity of the proof mass relative to truss structure. These signals are conditioned with low pass filters and amplified by gains K_e and C_e for the position and velocity respectively. The amplified and negated signal is fed back to the input of the current source. The current source outputs a signal which produces a force within the PMD. Thus a negative force in proportion to the position or velocity differential across the PMD is produced. This electrically derived force has components which have the same position dependance as a mechanical spring and same velocity dependance as a mechanical dashpot. These forces have the same effect as would a spring and dashpot on the dynamics of the PMD. Thus the linear spring and damping constants of the PMD can be tuned by simple variation of the appropriate electrical feedback circuit gain.

The feedback forces due to the electrical stiffness and damping are limited by the current drive capabilities of the Crown amplifier. The undistorted AC current output of the amplifier was limited to ± 10 amperes which translated to an available PMD force of about ±44 newtons. In the feedback scheme described above, this available force was dependant on the position and velocity of the proof mass. If at any gain setting the position of the proof mass dictated an electrical restoring force which was above the 44 newton limit, the current output of the amplifier would saturate; and the PMD would not behave linearly. The amplitude of vibration of the proof mass which would cause this saturation is inversely proportional to the feedback gain used. The electrical stiffness and damping in the PMD and thus the resonant frequency and damping ratio of the PMD were directly proportional to the feedback gains. Thus the current drive limitation places a limitation on the range of available tunings of the PMD in a given vibration

environment. The actuator frequency tuning was limited by this constraint to 120 Hz. The base spring provided the stiffness necessary for a resonance at 11 Hz and the electrical system could provide the electrical stiffness necessary to shift the PMD resonances up to 120 Hertz. Although higher tuning could be obtained, the system was not robust to external excitations since under these excitations the feedback signals would cause drive current saturation. The actuator could be tuned to any structural mode in the range from 11 to 120 Hertz by simply changing the position gain. The damping ratio of the PMD could likewise be varied over a range from 1% to 45% of critical by varying the velocity gain.

These electrical support systems created the damper system flexibility needed for optimal tuning to multiple structural modes and for testing the effects of parameter variation on the global system response. Electrical circuits were also used for tuning RSP and will be described in the next section.

4.4.3 Resonant Shunted Piezoelectric Support Circuitry

The resonant shunted piezoelectric requires external circuitry in addition to the piezoelectric capacitance to achieve the high damping levels afforded by tuning. In the resistive shunting case, this circuitry is simply a variable resistor. In the resonant case, this circuitry contains a variable resistor and a variable inductor in series. The variable inductor is necessary for tuning the electrical resonant frequency to the the vicinity of the truss modes.

The overall shunting circuit architecture is shown in Fig. 4.10. The piezoelectrics are wired together so that a single voltage across the combined electrode causes the two members on one side to contract while the other side expands. In this way the piezoelectrics are arranged to be sensitive to bending modes that have high strain in the central bays. The combined damper can be left open, shorted, shunted with a resistor, or shunted with a resistor-inductor circuit depending on the position of switch A (Figure 4.10). The piezoelectrics were driven by a Crown 300-IIA voltage amplifier with voltages up to ±45 volts. This is far below the total voltage sustainable by the piezoelectric before degradation of the piezoelectric properties.

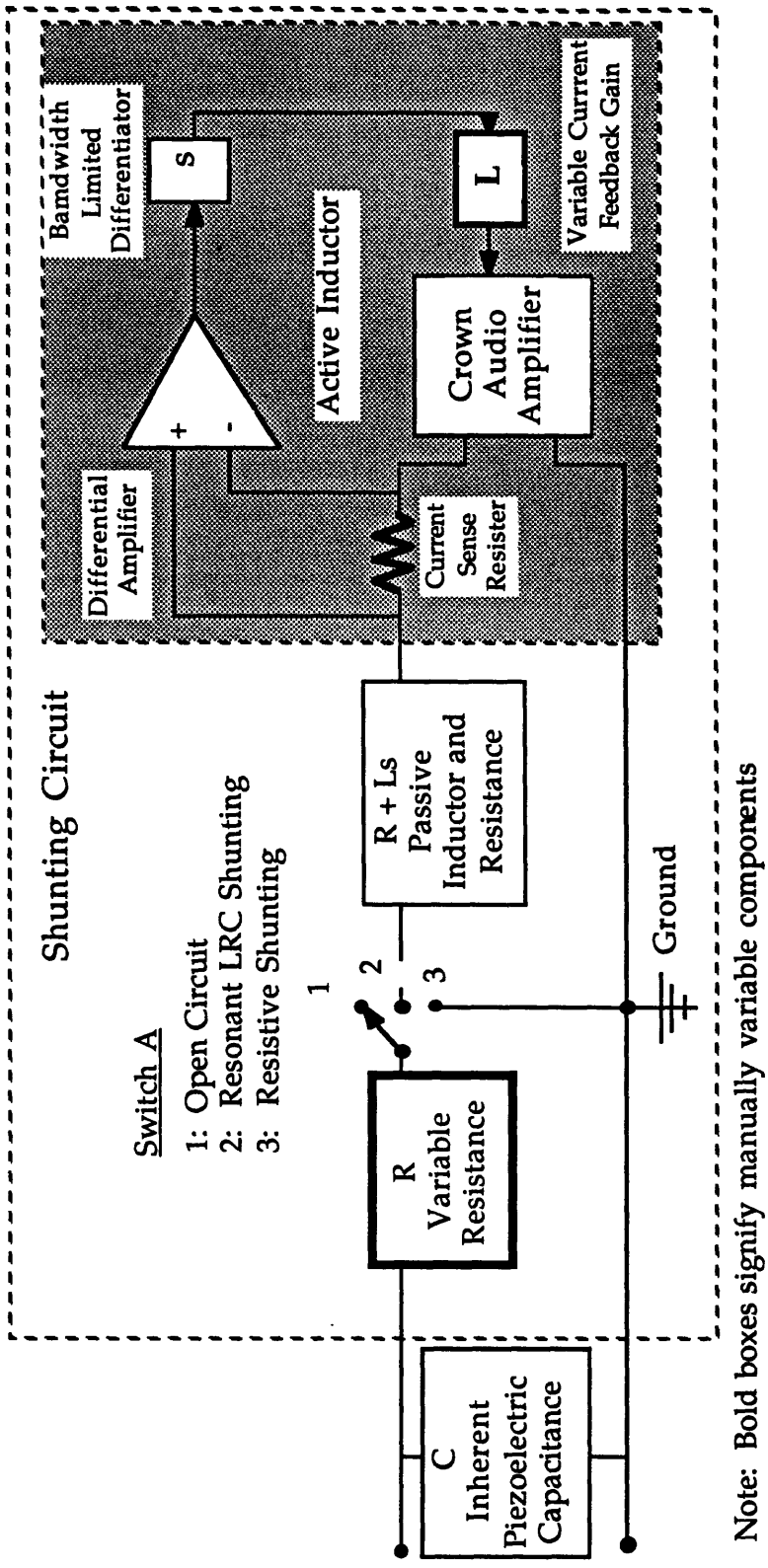

Figure 4.10 Shunted Piezoelectric Support Circuitry showing the Passive and "Active" Inductor as well as the Variable Resistance.

There were stringent criteria placed on the inductance necessary for the construction of the resonant shunted piezoelectric. The low combined piezoelectric capacitance (2.17 μFarads) necessitated the use of large inductances for tuning the piezoelectric to the lower structural modes. To tune to the first structural mode at 39 Hz, a 7.0 Henry inductance was required; while to tune to the third structural mode at 150 Hz, only 0.5 Henries were required. In simple coil inductors, such large inductances are usually associated with high resistances due to the large amount of wire needed to produce the inductance. The optimum tuning results for the RSP presented in Section 3.4.4 require low resistances, however. For a given piezoelectric capacitance lower tuning frequencies require larger inductance while maintaining low electrical resistance. To circumvent this problem high-Q inductors were used in series with an active variable inductor.

The high-Q inductors were copper windings around a toroidal iron core. Seven Henries of inductance was used for the circuit to be tuned to the first structural mode at 40 Hz. This base inductance was in series with an active variable inductance. The active variable inductor used for tuning was constructed using current rate feedback as shown in the Fig. 4.10. The current was measured at the output of the amplifier and differentiated using a stable differentiation circuit that limited the gain at high frequency. The differentiated current signal was then amplified and fed into the input of the inductor amplifier. This amplifier thus commanded a voltage across its output which was proportional to the rate of current going through the output stage of the amplifier. Thus the circuit reproduces the defining relation for an inductor. In the Laplace domain it is:

$$V_I = (Ls)\, I_I \tag{4.2}$$

were V_I is the voltage across the inductor and I_I is the current through the inductor. By varying the gain on the feedback current rate, the inductance for this circuit could be varied. This enabled the resonant electrical circuit to be tuned to the structural modes.

4.5 Summary

In this chapter, the designs of the main experimental components were reviewed. These components were the experimental truss test article, the damping mechanisms, and their supporting electronics. The experimental test article was designed to provide a low damping base structure upon which the damping enhancement could be tested. There were a requirements for dynamic isolation from the surrounding and three dimensional, free-free behavior which lead to the construction of a soft spring support system. A truss was chosen as the experimental article because a complex structure was required to ascertain the practicalities of the damping enhancement implementations.

The designs for both the PMD and the resonant shunted piezoelectric where shown. The PMD consisted of a linear DC motor with the magnetic circuit part of the motor serving as the proof mass. The consideration of the actuator dynamics was eliminated by the use of current drive circuitry. The actuator was made tunable by the addition of negative position and velocity feedback to produce electrical springs and dampers for the system.

The design of a piezoelectric truss member was presented which entailed the use of cylindrical piezoceramics and a fibrous composite outer shell. These members replaced the standard aluminum members in the truss. The electrodes of these members could be wired together and shunted by electrical circuitry to maximize energy dissipation as was explained in Chapter 3. The resonant electrical circuit was implemented with a variable resistor and an variable inductor created by current rate feedback to an amplifier. The resulting circuit allowed the resonant piezoelectric damper to be optimally tuned to the structural modes.

These devices were calibrated and tested for the damping that they could produce in the test truss. These test are presented in the next chapter.

Chapter 5
Experiments and Results

5.1 Overview

In this chapter the experiments that have been conducted for the verification of the damping enhancement methodologies discussed in the earlier chapters will be presented. The experimental setups will be described along with the data collection techniques used. The results of the various experiments will be briefly discussed with reference to their implications for damping enhancement of space structures.

The experiments conducted in this investigation fell into three general categories. The first set entailed the calibrations of the mechanisms used to both drive and damp the structure. Such tests were conducted on the proof mass actuator/damper as well as the piezoelectric truss member. These tests were designed to establish the fundamental parameters such as inherent damping and force sensitivities that would later be used in the system modelling. The second group of tests was designed to measure the structural parameters in the "undamped" baseline trusses. These tests were also conducted to verify the frequency domain modelling technique before more complicated impedances were introduced. Finally, the last set of tests involved adding two types of resonant damping schemes to the truss. Both resonant PMDs and piezoelectrics were added, in order to collect data on their effectiveness as system dampers and sensitivity to tuning parameter variation.

The experiments outlined above were designed as a test of the frequency domain modelling techniques for damping enhancement methodologies. The test were conducted on a realistic 3 dimensional, 10 bay truss suspended in a simulated free-free condition using space-realizable actuators, sensors, and dampers. This realistic implementation of damping techniques gave many useful insights into the practical aspects of damping design and complex structural dynamics in general. This data on the practical implementation of damping methodologies for space structures should hopefully prove valuable for the designer.

5.2 Damper/Driver Calibration Tests

Tests were conducted on the PMD and piezoelectric truss member described in Chapter 4 in order to determine the static and dynamic properties of the devices. These properties included the force levels attainable for a given voltage or current, the damping levels and natural frequencies of the PMD in free vibration, as well as other measurable quantities necessary for the impedance models of the driver/damper elements of the system. These parameters were used in the design of the servo loops to create tunable damping properties as described in Section 4.4. They were also used in the global system models for prediction of the structural behavior.

5.2.1 Proof Mass Actuator/Damper Calibration

The calibration tests on the PMDs can be divided into three classifications. To the first group belong those test which were conducted with the resonant part of the damper fixed. These are called the static tests. The second group contains dynamic tests of the dampers without position or velocity feedback. These tests are called open-loop dynamic tests. The third group contains tests on the PMDs with the position and velocity feedback loops described in Section 4.4 closed to enable the devices to be tuned. These tests are the closed-loop dynamic tests.

The static tests on the PMD calibrated the damper for the force produce for a given driving current while the proof mass was fixed. These test established the manufacturing integrity of the actuator as well as the attainable force output. This information was fundamental to the design of the control systems used for damper tuning.

The setup used in the static tests for the PMD is shown in Figure 5.1. The PMD is mounted vertically, and the drive coil was connected to ground through a PCB force transducer model #208A02. The proof mass is fixed to a rigid cross bar to prevent its motion. The force produced on the transducer is then measured as a function of current over the range from 0.1 to 5 Amperes. The current is provided by a voltage controlled current source as described in Section 4.4.2. The force to current relation is shown by the curve in Fig. 5.2

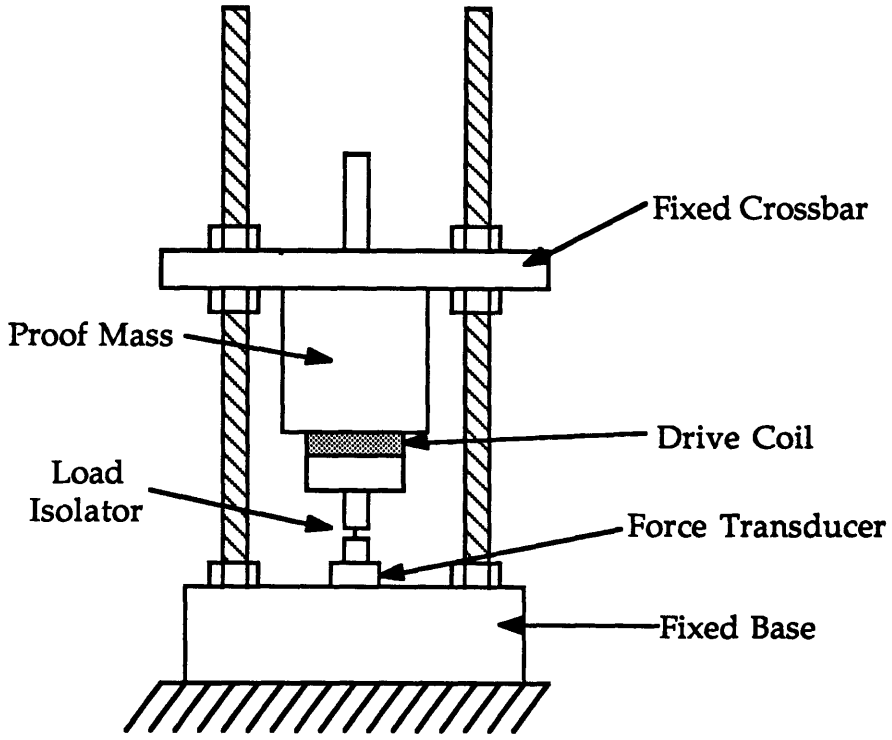

Figure 5.1 Static Test Setup for PMD Force/Current Sensitivities

for actuator #1. This curve is representative of the PMD damper/actuators. It illustrates the linear dependance of actuator force on current. The average ratio of force to current for the proof mass actuators/dampers was 4.64 newtons/ampere with an upper limit of 5.0 amperes imposed by drive circuitry limitations.

The open-loop dynamic properties tests of the proof mass dampers were conducted to determine the devices' natural frequencies and damping. The setup for this experiment is shown in Figure 5.3. The proof mass was free to vibrate in the vertical direction. The amplitude and velocity of the proof mass relative to the base was measured with the LVDT and LVT described in Section 4.4.2. In these tests, the device was excited with a pulse current and the ringdown of the proof mass was recorded using a Nicolet digital oscilloscope. The ringdown traces were then analyzed to determine the device's natural frequencies and damping. The linear decay envelop of the ringdown response indicated that the primary source of inherent damping in the device was friction. The measured natural frequencies and the Coulomb friction forces of the devices are presented in Table 5.1 along with the force/current sensitivities of the devices measured in the static tests.

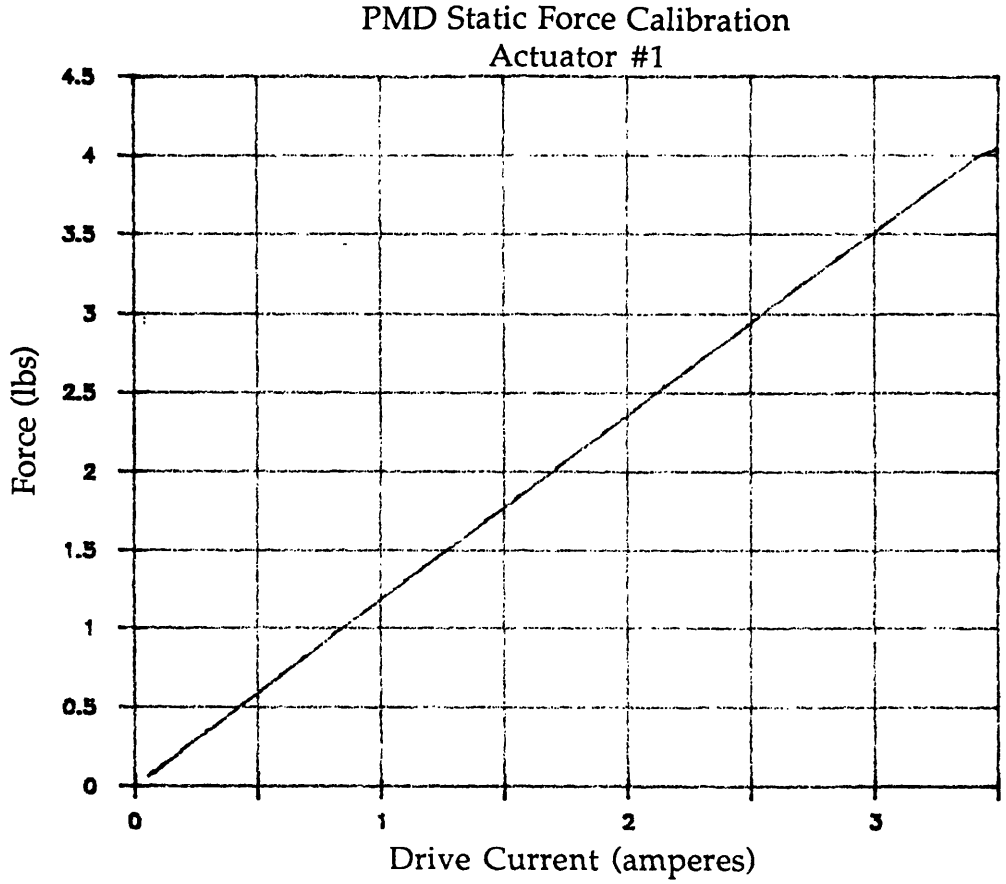

Figure 5.2 Static Force vs. Drive Current for PMD-1

PMD Damper/Actuator Properties

PMD	Force Sensitivity (N/Amp)	Natural Frequency (Hz)	Friction Force (N)
1	4.72	11.11	0.55
2	4.82	11.07	1.17
3	4.41	11.52	0.33
4	4.73	11.20	0.47

Table 5.1 Properties of PMD Actuator/Dampers Including Force to Current Conversion Factors, Inherent Natural Frequencies and Sliding Friction Forces

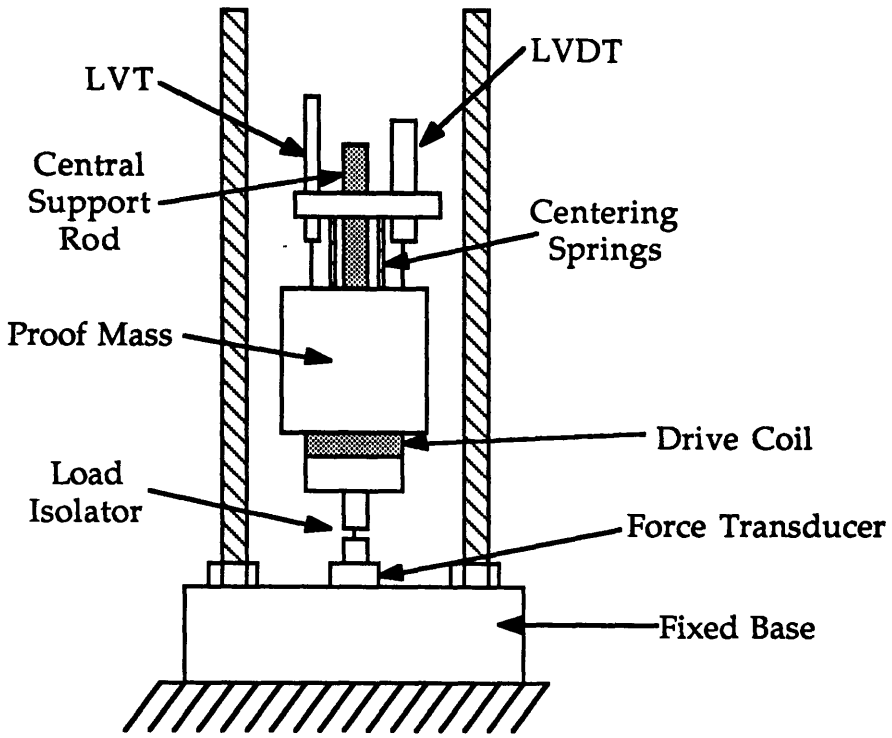

Figure 5.3 PMD Dynamic Test Setup for Determining Device Natural Frequencies and Damping Ratios

In the closed-loop dynamic tests, the resonant frequencies and damping of the device were measured with the position and velocity feedback loops closed. The dependance of the PMD's resonant frequency and damping ratio on both the position and velocity feedback gains was quantified. The designs for these feedback systems were presented in Section 4.4.2. The setup was the same as that used for the open-loop dynamic calibration tests shown in Figure 5.3 with the exception that the feedback electronics were active in the closed-loop dynamics tests. The position feedback gain was varied to produce device natural frequencies and damping which varied from 20 to 120 Hz for the natural frequencies and from 45.0% to 2.0% of critical for the damping ratios.

The data from the closed-loop dynamic tests consisted of position and velocity gain pairs and the corresponding PMD natural frequency and damping ratios. These data points were used to determine the PMD's frequency and damping at arbitrary feedback gain settings via interpolation. Within the gain space noted above, the natural frequencies and damping of the device which resulted from known position and velocity feedback gains

could be found by bilinear interpolation with the experimental data from dynamic tests at nearby gain settings. Figure 5.4 illustrates this concept of bilinear interpolation to determine the dynamic properties of the PMD device at gain settings which did not correspond to the tested points. An analytical model was used to determine the rough values of the feedback gains necessary for actuator tuning. The actual behavior of the feedback circuits was sufficiently complicated to warrant the use of the database gathered in the closed loop dynamic tests to predict actuator tuning rather than an inaccurate and complex analytical model.

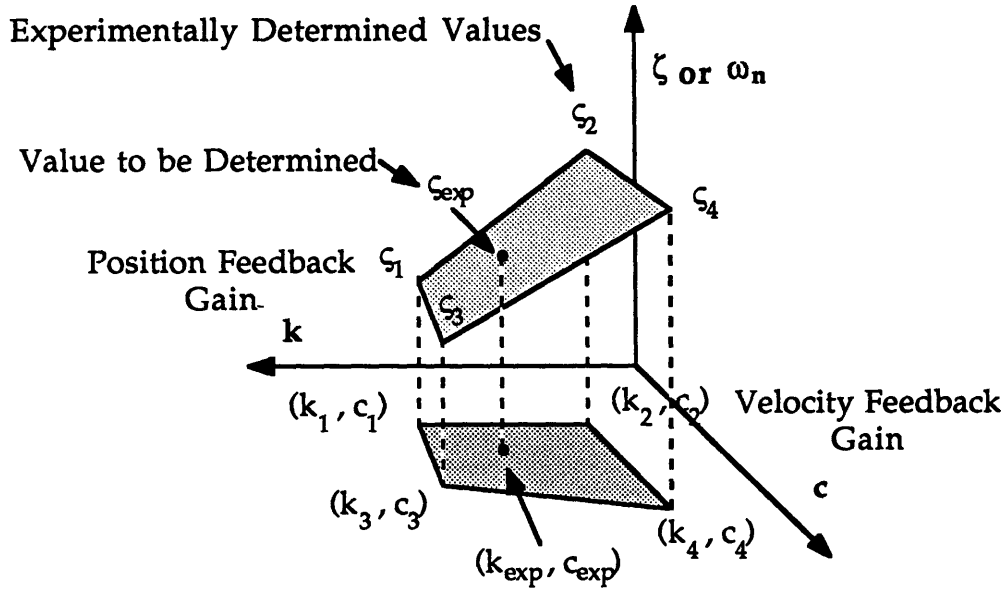

Figure 5.4 Determination of PMD Natural Frequency or Damping Ratio as a Function of Position and Velocity Feedback Gain by Interpolation from Experimentally Determined Nearby Points

5.2.2 Piezoelectric Truss Member Calibration

Several tests were preformed on the piezoelectric truss members to determine their static and dynamic properties. The first was a static test to determine the amount of force that the member could exert against a fixed boundary as a function of the driving voltage. The second was a dynamic test to determine the performance of the resonant circuit used in the resonant shunted piezoelectric application described in Section 4.4.3. Specifically, this

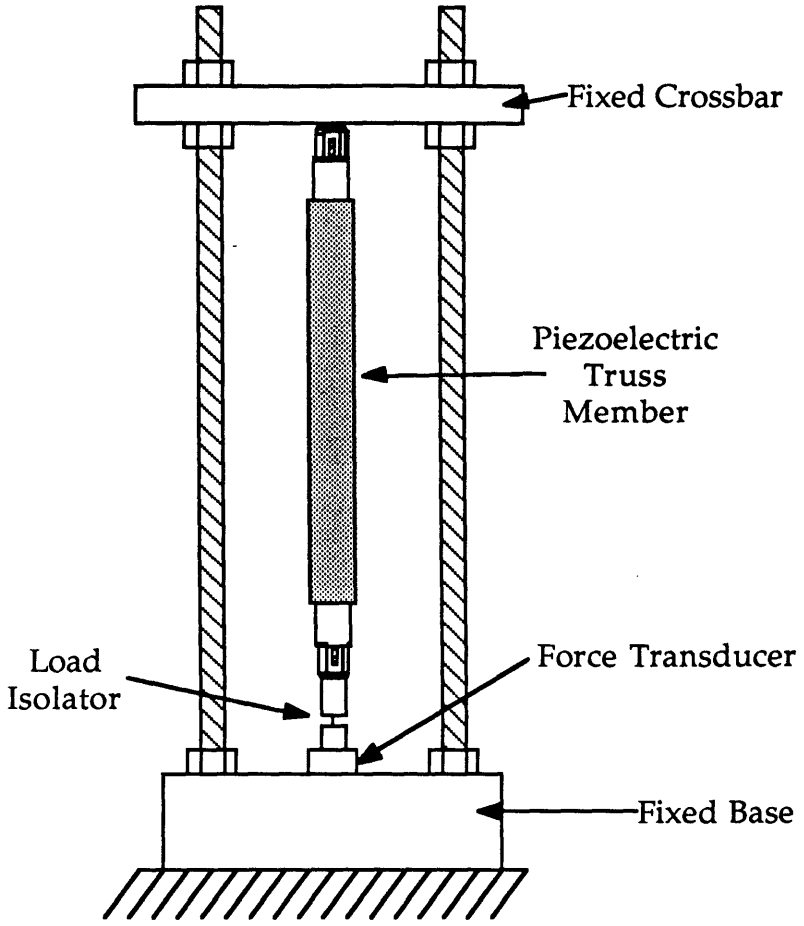

Figure 5.5 Static Force Sensitivity Test Setup for Piezoelectric Truss Member

second test was used to calibrate the performance of the active inductor part of the shunting circuit presented in Figure 4.10 of Section 4.4.3.

The experimental setup used in the static test of the piezoelectric truss member is shown in Figure 5.5. Just as in the PMD static tests, the piezoelectric truss member is mounted vertically onto a force transducer attached to a rigid base. The top of the device was then attached to a rigid cross bar to constrain axial expansion of the piezoelectric truss member. The force generated by the member was then measured as a function of a sinusoidal voltage applied across the piezoelectric electrodes. The voltage was supplied by a Crown DC-300IIA audio amplifier in the range from 0.1 to 40 volts RMS. The results for this test, shown in Figure 5.6 for the first piezoelectric truss member, demonstrate the linearity of the piezoelectric truss member performance. On average, a piezoelectric truss member was

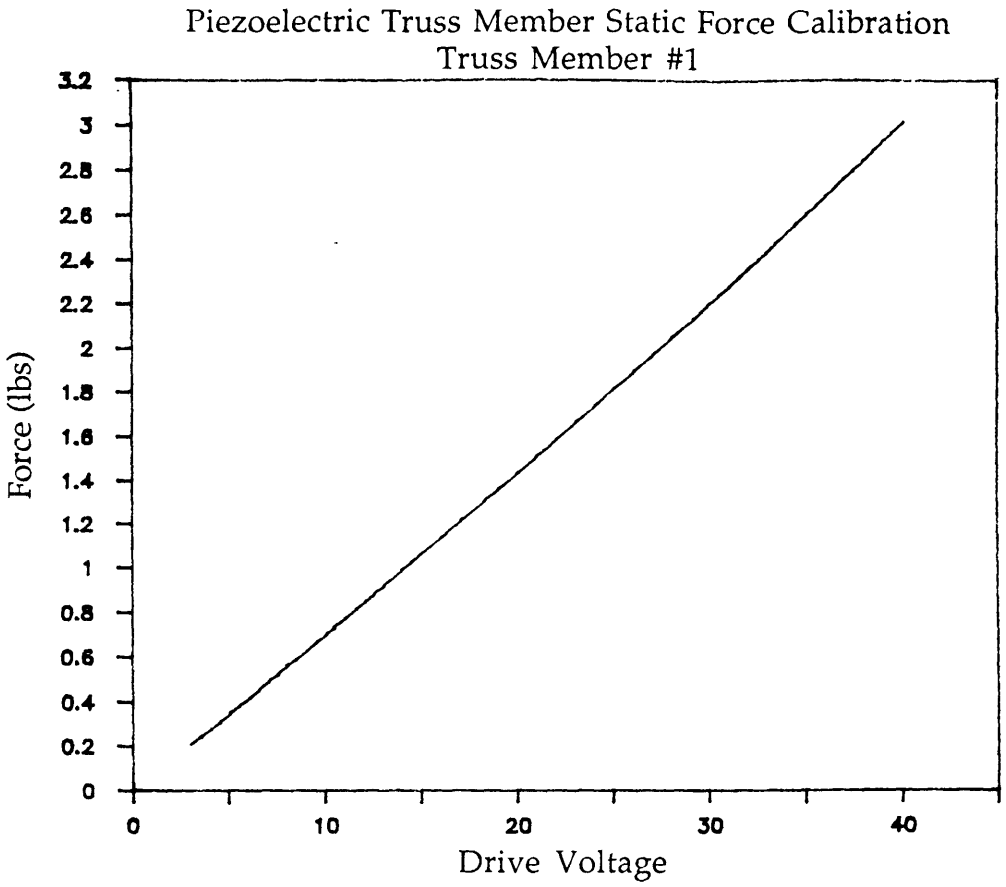

Figure 5.6 Piezoelectric Truss Member Static Force/Applied Voltage Curve for Truss Member #1

Piezoelectric Truss Member Force Sensitivities

Piezoelectric Member	Force Sensitivity (N/Volt)
1	0.319
2	0.293
3	0.331
4	0.291

Table 5.2 Comparison of Piezoelectric Truss Member Force Sensitivities

found to produce about 0.3 newtons/volt in these tests. The actual sensitivities for each of the four members is shown in Table 5.2.

Dynamic tests were conducted on the piezoelectric truss members to calibrate the shunting impedance used in the resonant shunted piezoelectric application for the members. In this application, presented in Section 4.4.3, an inductor and resistor shunt the inherent capacitance of the piezoelectric to produce a resonant LRC circuit. The inductor consists of a fixed passive inductor and a variable "active" inductor to allow variable tuning of the LRC circuit's resonant frequency. The tests were designed to provide data on the actual inductance of the "active" inductor as a function of the variable current feedback gain used to adjust that inductance as described in Section 4.4.3.

In these dynamic calibration tests, the piezoelectric members are installed in the experimental truss structure as shown in Figure 5.7c. The members are wired together so that the capacitances of the individual members appear in parallel to each other creating an total capacitance which is the sum of the member capacitances. This total capacitance is shunted by a variable resistor in series with a passive and active inductor as shown in Figure 4.10. This circuit was driven by a voltage applied across the capacitor via a Crown DC-300IIA amplifier. The ratio of the drive voltage to the drive current was measured as a function of frequency to produce a transfer function for the LRC circuit. This transfer function was then identified to find the natural frequency and damping of the LRC circuit. This test was preformed at several values of the gain of the current feedback loop of the active inductor to produce a formula for the effective circuit inductance as a function of gain

$$L_{tot} = L_{pas} + 0.0021 \cdot (\text{gain setting})$$

where the gain was variable from 0 to 600. The total capacitance of the circuit was measured with a Continental Specialties Corporation model 3001 capacitance meter to be 2.17 μfarads. These experimentally determined values were necessary to provide effective tuning of the electrical resonance to the structural modes of the truss to achieve damping in a manner described in Section 3.4.4.

5.3 Truss Model Validation Tests

5.3.1 Overview

Several tests were preformed to establish the dynamic properties of the unenhanced truss structure, and also to verify the system modelling techniques described in Chapters 2 and 3. These tests involved the identification of the first 3 bending modes of a truss structure in three configurations. The experimental truss structure is described in Chapter 4, Section 4.2. The first configuration was a truss composed entirely of aluminum members. The second configuration was the baseline aluminum truss with four aluminum members of the center two bays replaced by plastic members. The third configuration was the aluminum truss with four aluminum members of the central two bays replaced by the piezoelectric truss members described in Section 4.3.2. Only those tests with the piezoelectric members' electrodes shorted or resistively shunted are included in this section. Resonant damping enhancement schemes such as the proof mass damper or resonant shunted piezoelectric are covered in Section 5.4.

The modal frequencies and damping ratios for the first 3 bending modes of the experimental article in the various configurations were measured in the tests on the structures. The data for the tests consisted of time domain signals and frequency domain transfer functions between the driver current and the accelerometer signals at 18 locations throughout the truss. The truss was excited by pulsed psuedo-random white noise centered around the particular mode being investigated. In all structural experiments, the excitation signal was produced and the data was collected by a Signology SP-20 digital data logger. The structural modal frequencies and damping ratios were calculated from the time domain signals using a Recursive Lattice Least Squares (RLLS) identification algorithm, Ref. [28].

The results from the structural tests are compared to the natural frequencies and damping ratios produced by the frequency domain system analysis. The techniques for frequency domain system modelling described in Chapter 2 have been implemented in a computer program. The program allows complete frequency domain modelling of complex structural systems including calculation of approximate or exact frequencies and damping ratios

using equations 2.45 and 2.50, respectively. The techniques implemented for calculating both the "exact" and approximate system eigenvalues are presented in Appendix A. The model used for experimental comparison comprised 44 network nodes and 256 DOF. This model was then reduced exactly to an 18 by 18 system impedance matrix via a static condensation of certain unforced nodes. The retained DOF corresponded to the locations of the accelerometers on the test specimen.

The approximate and exact values of the system natural frequencies and damping as well as analytical modeshapes were calculated for the first 3 structural bending modes for comparison to the experimental data. In the aluminum, plastic, and piezoelectric model validation tests, unknown parameters in the truss model, such as the unenhanced truss' base structural damping or the effective length of the aluminum members, were varied so as to fit the frequency and damping of the model's first mode to the experimental data. This "calibrated" the unenhanced baseline models to the experiment test article in the first bending modes. The remainder of the model modes were not so adjusted and therefore represent the actual deviation of the model from the experimental article. Once the parameters such as base damping and effective length were calibrated for the first modes of these model validation tests, they were included unchanged in the enhanced damping truss models.

5.3.2 All Aluminum Truss Tests

The purpose of the tests on the unenhanced all-aluminum member truss was to provide information on the baseline truss dynamic properties for comparison with the enhanced damping cases. As a second consideration, the data gathered on the undamped truss was used to fine tune the impedance models for the truss elements and the driving mechanism.

The experimental setup used in all the truss model validation tests is shown in Figure 5.7a. For the model validation tests the end masses shown in this figure were dummy masses place to give the truss symmetry. The truss was excited using the PMD/driver #4 at node 1. The inherent resonance of the PMD actuator was tuned to 11 hertz, far below the first structural mode at 39 hertz. The 3 bending modes examined throughout the experiment were

Figure 5.7a: All-Aluminum Truss Dynamic Test Setup (Top View)

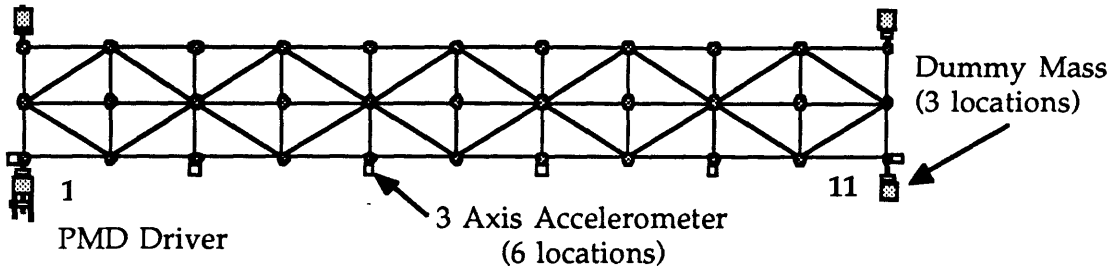

Figure 5.7b: Model Validation Tests for Truss With Plastic Members

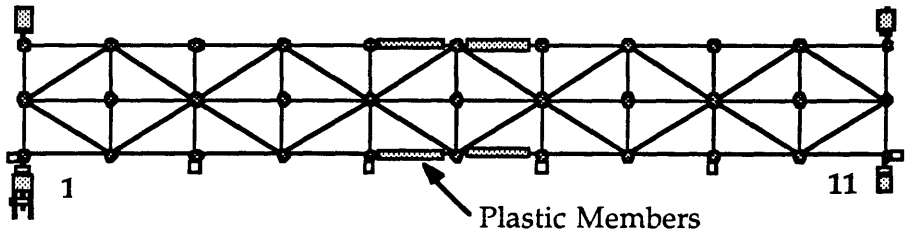

Figure 5.7c: Truss Setup for All Tests with Piezoelectric Truss Members

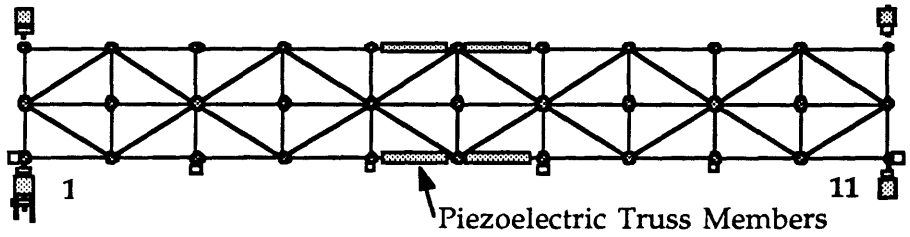

Figure 5.7d: PMD Damping Test Setup

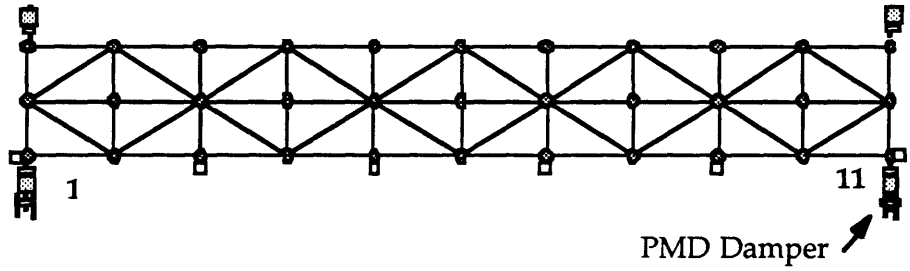

Figure 5.7 Setups for Truss Dynamics Experiments showing the All-aluminum Truss Setup (a), the Truss with Plastic Members in the Center Bays (b), the Truss with Piezoelectric Members in the Center Bays such as in the Shorted Piezoelectric or RSP Damping Experiments (c), and the Truss for PMD Damping Experiments (d)

primarily in the plane horizontal to the ground although in the higher modes some coupling appeared to the modes in the vertical plane.

The natural frequencies and damping ratios for the undamped aluminum truss are presented and compared with the analytical prediction in Table 5.3. The truss has bending modes at 39, 99, and 149 hertz with 0.6%, 0.5%, and 0.3% critical damping respectively. These low damping ratios enabled the measurement of small changes in the damping levels as damping mechanisms were tested.

All-aluminum Truss

Frequencies (Hz)			
Mode	Experimental	Analytical model	
		Approximate	Exact
1	39.23	39.90	39.23
2	99.42	91.35	91.10
3	149.01	145.60	146.58
Damping Ratios (ζ)			
Mode	Experimental	Analytical model	
		Approximate	Exact
1	.00632	.00632	.00613
2	.00482	.00530	.00400
3	.00304	.00723	.00364

Table 5.3 Comparison of the Experimental Frequencies and Damping Ratios with the Model Values for the First Three All-aluminum Truss Bending Modes

As can be seen in Table 5.3, the approximate analytical formulas can give good estimates for the global system frequency and damping levels. The approximate values were calculated using the technique described in Appendix A. The analytical mode shapes (1st, 2nd, and 3rd bending) from a completely undamped finite element model were used in the Rayleigh Quotient analysis for the approximate frequency and damping.

The approximate first mode frequency and damping fit the experimental data well. This was expected since the model parameters were

adjusted so that the *exact* algorithm frequencies and damping agreed with the data in the first mode. This implies that the approximate algorithms can reproduce the performance of the exact algorithms in determining a model's frequency and damping. The second mode frequency is 8.1% lower than the experimental value while the analytical damping coefficient is 8.4% higher than the experimental. The approximate value for the frequency of the third mode is 2.3% lower than the experimental, while the damping is 138% higher. In general, the errors in the approximate method are due to modelling errors. The results obtained using the approximate techniques correlate very well with the results obtained from the exact analysis but not as well with the experiment data as shown in Table 5.3. This implies that the approximate technique accurately reflects the model poles but that the model poles themselves are inaccurate.

The exact values were found by searching for the zeros of the determinant of the system impedance matrix. This entails a numerical search in two dimensions and is implemented using a gradient search method as described in Appendix A. The results of the search represent the true poles of the model in the s-plane and reflect the accuracy of the model to this extent.

The model first mode frequencies and damping were roughly fit to the experimental results by varying certain model parameters such as aluminum tube stiffness and structural damping. The error between the calibration tests first mode predictions and the experimental values were thereby maintained to within 0.1 Hz difference in natural frequency and 0.05% of critical in the damping ratios. The model exhibited slight variation from the test results for the upper two modes. The differences in frequency predicted and measured can probably be attributed to interaction of the horizontal and vertical bending modes. Since the truss is a true three dimensional structure, it contains nearly identical modes at the same frequencies in the horizontal and vertical planes. Ideally, only the horizontal ones are excited in this test setup. In a real structure with dimensional irregularities and suspension loading effects these modes couple. This interaction causes one of the modes to be at a higher frequency while the other is at a lower frequency than would be expected. This effect causes the actual frequencies to vary from the expected natural frequencies. The effect can be seen in several of the global transfer functions seen in Figure 5.8, most notably the 3rd bending for the plastic truss.

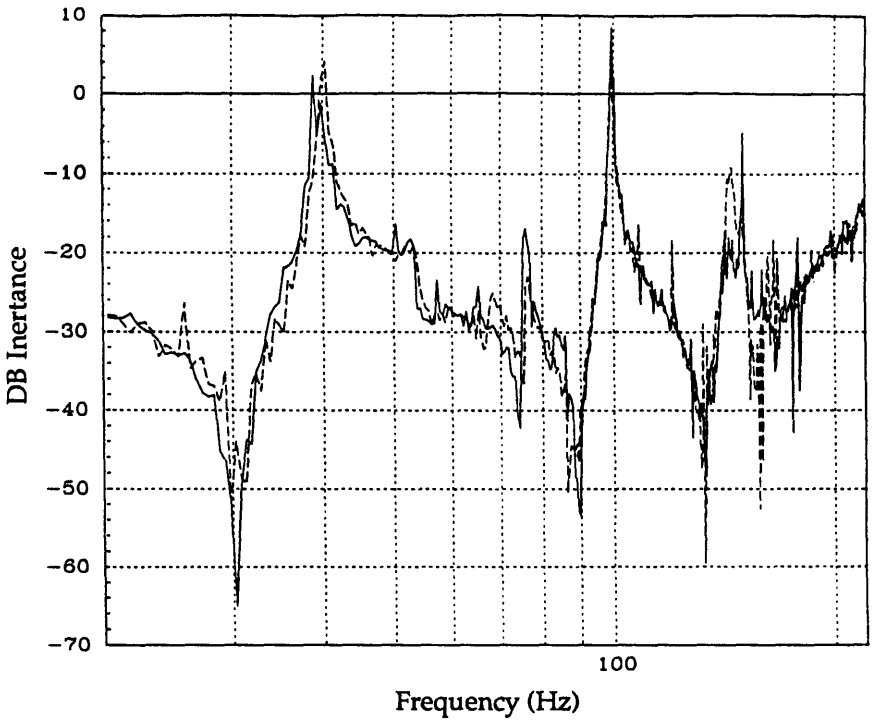

A) Global Transfer Function for All-aluminum (solid) and Shorted Piezoelectric (dash) Trusses

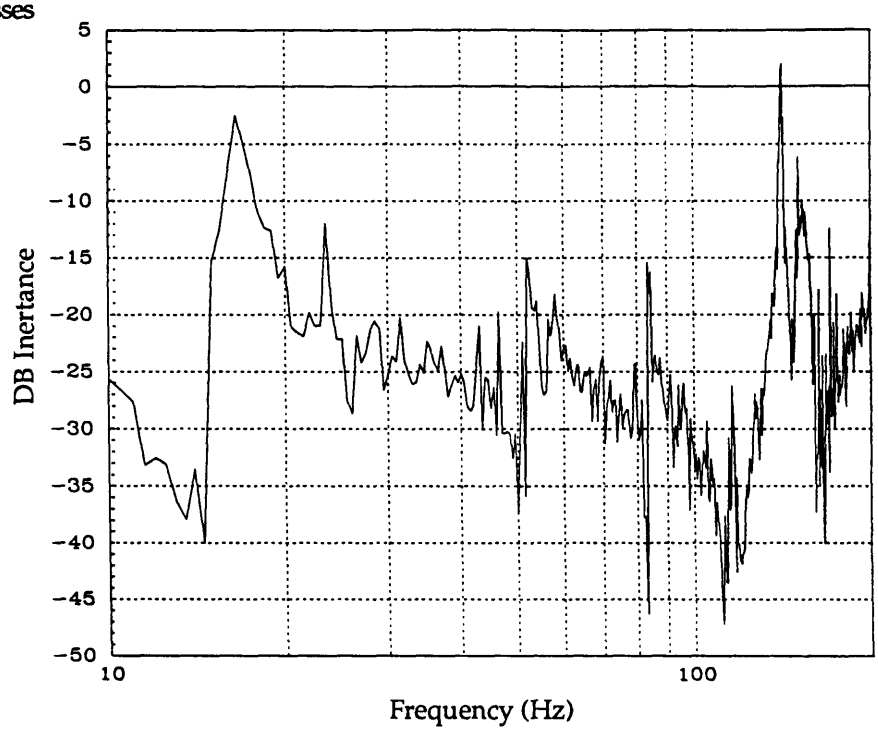

B) Global Transfer Function for Truss With Plastic Members in Central Bays

Figure 5.8 Global Transfer Functions of the Three Validation Test Setups: The All-aluminum and Shorted Piezoelectric Trusses (A) and the Plastic Truss (B)

In conclusion, after the model had been calibrated to the experimental first bending, the frequency domain modelling technique modelled the natural frequency and damping in the higher two modes very well. The exact pole locations in the model matched the experimental pole locations very closely. The approximate techniques for determining the structures pole natural frequencies and damping predicted the truss's pole locations less accurately but with far less effort than the exact pole search.

5.3.3 Tests on Truss With Plastic Central Bay Members

Tests were next conducted on the aluminum truss with 4 members of the central 2 bays replaced by plastic members as shown in Fig. 5.7b. The tests were conducted in the same manner as the all-aluminum truss tests described above. The purpose of the tests was to validate the frequency-dependant analytical model's capability to analyze structures with diverse impedances and high loss members. This provides information on the frequency domain modeling methods ability to assimilate the damping from discrete devices into the global system damping.

The plastic tubes were constructed from General Electric Lexan Polycarbonate, a structural plastic with stiffness of 2.4 GPa and a material loss factor of about 0.02. The tube cross sectional area was 112 square millimeters with an effective length the same as for the aluminum members. The insertion of plastic members greatly effected the truss's dynamic properties.

The results from the dynamic experiments can be seen in Table 5.4 compared to the analytical model, and in Table 5.5 where they are compared to the other validation tests. Several effects are evident. The first mode of the truss experienced a large frequency reduction (57% less than the all aluminum truss) and a large increase in modal damping (102% higher than the all aluminum truss) as a result of the inclusion of the softer, lossy members. The higher modal frequencies experienced less of a frequency reduction with the 3rd mode shifting only 6% from the aluminum truss. This decrease in effect can be attributed to the fact that the strain energy is more evenly distributed throughout the truss in the higher bending modes as opposed to being concentrated in the central bays as in the first mode. For the same reason, the damping increase attainable by the damped element

Truss with Plastic Members

Frequencies (Hz)			
Mode	Experimental	Analytical model	
		Approximate	Exact
1	17.00	18.27	16.35
2	58.10	54.30	53.94
3	141.85	146.59	139.08
Damping Ratios (ζ)			
Mode	Experimental	Analytical model	
		Approximate	Exact
1	.0126	.0115	.0126
2	.0089	.0066	.0057
3	.0052	.0060	.0036

Table 5.4 Comparison of Experimental and Analytical Modal Frequencies and Damping for the Truss with 4 Plastic Members in the Central Bays

Model Validation Tests Experimental Results

Frequencies (Hz)			
Mode	All-aluminum	Plastic Members	Shorted Piezoelectrics
1	39.23	17.00	39.41
2	99.42	58.10	99.05
3a	149.01	141.85	145.47
3b			152.76
Damping Ratios (ζ)			
Mode	All-aluminum	Plastic Members	Shorted Piezoelectrics
1	.0063	.0126	.0119
2	.0048	.0089	.0062
3a	.0030	.0052	.0095
3b			.0115

Table 5.5 Comparison of the Experimental Frequencies and Damping Ratios for the Three Model Validation Configurations

inclusion decreases with the higher modes from a damping increase of 100% over the aluminum in the first mode to only 68% in the third.

The analytical model can be seen to handle simple changes of material loss factor or stiffness fairly well with the major discrepancies corresponding to the original modelling errors for the aluminum truss. No frequency dependance was assumed for either the loss factor or stiffness of the plastic material since it was in its stable glassy region.

One interesting point was the difficulty experienced in experimentally determining the frequency of the second bending mode from visual inspection of the transfer function data. The transfer function from the forcing at node 1 to the acceleration in the z direction at node 1 for the all-aluminum, plastic, and shorted piezoelectric configurations can be seen in Figure 5.8. The difficulty in identifying the second bending mode can be attributed to two causes. First, the large frequency shift associated with the inclusion of the plastic members placed the second bending mode in the vicinity of a torsional mode making it hard to differentiate between the two. Secondly, a change in the second mode shape decreased the second mode response at node 1. The mode was identified by looking at the acceleration signals coming from other locations on the truss and by comparison with the model.

5.3.4 Tests on Trusses with Shorted and Resistively Shunted Piezoelectrics

Tests were conducted on the aluminum truss with piezoelectric truss members replacing 4 aluminum members in the central bays of the truss in the same configuration as the plastic members. The configuration used in these tests is shown in Figure 5.7c. Two tests will be discussed in this section. Those with the piezoelectric member's electrodes shorted and those with a resistor placed across the electrodes as described in Section 3.4.3.

The purpose of the tests with shorted electrodes was to provide a baseline "undamped" comparison for the resistive and resonant shunted piezoelectric tests to follow. The shorted electrode tests also provide needed information on the stiffness and inherent damping levels of the piezoelectric actuators, data that was not obtained in the previously discused calibration tests. By finding the values of the piezoelectric truss member parameters,

such as total stiffness and material loss factor, which enabled the model to best fit the tests in the first bending mode, an accurate model could be developed for the truss members. Thus the tests provided data on the base structure for the piezoelectric damping tests to follow and helped complete the piezoelectric truss member model.

At this point the wiring of the piezoelectrics used in both the resistive and resonant shunted piezoelectric experiments will be discussed. The electrodes for the four piezoelectric truss members were wired together to achieve a single bending actuator or damper. They were electrically connected so that a voltage placed across the combined damper would apply opposite polarity voltage to the members on opposite sides of the truss. Thus, the two members on one side would contract while the other two on the opposite side would expand. The total piezoelectric damper was only sensitive to bending stresses and strains; and, in this configuration, was suitable as a damper only in regions of high curvature.

The dynamic properties of the shorted piezoelectric truss are shown along with the model results in Table 5.6 and in comparison to the other validation tests in Table 5.5. The first mode frequency of the experimental truss with the piezoelectric truss members substituted into the central bays is 39.41 Hz as compared to 39.23 for the all-aluminum truss. This small shift in the resonant frequency implied that the piezoelectric members had been manufactured with approximately the same stiffness as the aluminum members. As shown in Table 4.4 in Chapter 4, this stiffness is almost entirely due to the piezoelectrics inside the composite member rather than the composite itself. Thus, more of the member strain energy is located in the piezoelectric for conversion to electrical energy.

The third bending mode splits into two closely spaced modes at separate frequencies as a result of the coupling caused by the insertion of the slightly-more-stiff piezoelectric members, as was described in Section 5.3.2. Both the third horizontal and vertical bending modes are now partially observable from the accelerometer located at node 1 measuring acceleration in the z direction. This partial observability is reflected in the increase of measured damping in this mode since it is difficult for the RLLS identification routine to distinguish damping from unobservability. As a result, the discrepancies between the experimental and analytical prediction of the third mode damping are understandable in terms of the artificial

Truss with Shorted Piezoelectric Members

Frequencies (Hz)			
Mode	Experimental	Analytical model	
		Approximate	Exact
1	39.41	40.62	40.01
2	99.05	91.70	91.46
3a	145.47	144.48	145.48
3b	152.76	136.15	not found
Damping Ratios (ζ)			
Mode	Experimental	Analytical model	
		Approximate	Exact
1	.0119	.0125	.0117
2	.0062	.0073	.0056
3a	.0095	.0079	.0044
3b	.0115	.0094	not found

Table 5.6 Comparison of Experimental and Analytical Modal Frequencies and Damping Ratios for the Truss with Shorted Piezoelectric Members in the Center 2 Bays

damping inserted into the experimental measurement by the identification algorithm as well as the fact that the model, being completely symmetric, would naturally not reflect the coupling of the two bending modes.

Tests were also conducted on the truss when the electrodes of the piezoelectric members were shunted by a variable resistor. These tests were only conducted on the first mode. Their purpose was to validate the concept of shunted piezoelectric damping. By comparing the increase in damping afforded by the shunting resistor, the value of the Generalized Electromechanical Coupling Coefficient (GECC) for the first mode could be found. The GECC, described in Equation 3.5.1, is the fundamental constant determining the effectiveness of the shunted piezoelectric on the structure.

The tests were conducted by measuring the first mode natural frequencies and damping at various shunting resistances. This data can be represented as a curve of damping in the first mode versus nondimensionalized resistance. This experimental curve can be compared to

the curve generated by Equation 3.42a, the material loss factor for a resistive shunted piezoelectric.

There are several difficulties in this comparison, however. Equation 3.42a represents the material loss factor of just the resistive shunted piezoelectric and not the total loss factor of a structure incorporating the piezoelectric. As shown by Equation 3.1, the total structural loss factor is the average of the loss factor of the structures constitutive materials weighted by the proportion of the strain energy in the material. The problem can be circumvented by using the generalized piezoelectric coupling coefficient in Equation 3.42a rather than the coupling coefficient for the material. The generalized coupling coefficient includes the ratio of the total structural stiffness to the stiffness of the piezoelectric and thus compensates for the fact that not all of the structure's strain energy is in the piezoelectric material. Another problem in the comparison between the theoretical curve and the experimental data is the fact that the structure has energy loss which is not due to the piezoelectric. This component of the total system loss factor must be removed from the experimental data before comparison with the theoretical curves for resistive shunted piezoelectrics. Fortunately, the base system loss factor was previously identified in the shorted piezoelectric tests.

The experimental and analytical model damping curves can be seen compared in Fig. 5.9. The base damping of the shorted piezoelectric test structure has been subtracted from the data for the resistive shunting case to leave only the damping increase due to the resistive shunting. The form of the experimental damping increase shows remarkable correlation with the shunted piezoelectric model lending credence to the analysis technique used for shunted piezoelectrics in Chapter 3. The resistively shunted piezoelectrics contribute about 0.01 to the loss factor of the truss which is the value that would be expected if 14.3% of the strain energy in the first mode was resident in the piezoelectric truss member. As predicted by theory, the loss factor afforded by the resistively shunted piezoelectrics rolls off for values of the shunting resister either smaller or larger than optimal. In this case the optimal resistance value for the first bending mode at 40 HZ was 1963 Ohms. The exact value of the GECC for the first mode was found from the data by fitting the theoretical curve to the data. This fitted value, $K_{31} = 0.146$ (shown in Figure 5.9), was used in subsequent modelling of the resonant shunted piezoelectrics.

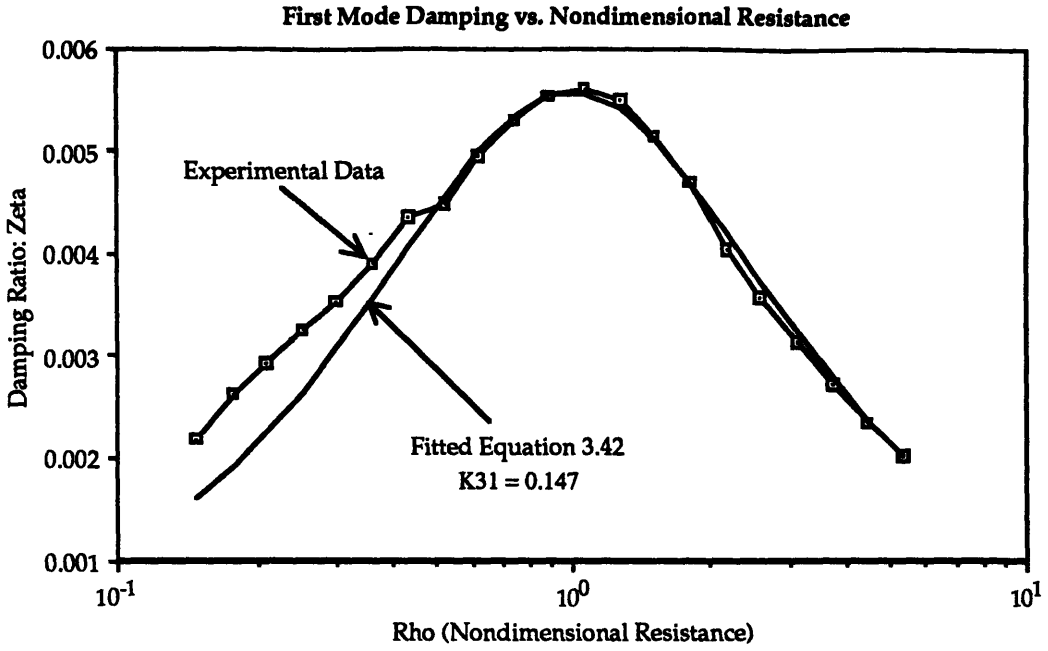

Figure 5.9 First Mode Damping Experimental Results for Resistively Shunted Piezoelectrics Fitted with the Analytical Model in Equation 3.42a

5.4 System Damping Enhancement Tests Using Resonant Dampers

5.4.1 Overview

At this point, the tests on the damping enhancement mechanisms implemented on the experimental truss will be discussed. Two types of resonant damping devices were implemented on the truss for damping enhancement. The two devices considered were proof mass dampers and resonant shunted piezoelectric truss members. Both devices relied on electrical state feedback systems to give them the capability of easily variable tuning as described in Section 4.4.

The tests conducted with these damping mechanisms were twofold. The first involved optimally tuning the damper to the structural mode of interest and measuring the resultant modal frequencies and damping of the truss. This type of test was directly comparable to the validation test procedure presented in the previous section. The second type of test on the resonant dampers entailed varying the tuning and internal damping parameters of the devices in the vicinity of the optimal tuning conditions and recording the resulting variation of the global system frequencies and damping. This type of test provides sensitivity information useful in damping enhancement system design and verification.

The purposes for the resonant damper tests were:

1) to gain insight on the system damping enhancement afforded by resonant dampers.
2) to investigate the problems associated with realistic implementation of these schemes on complex structural systems.
3) to investigate the fundamental factors common to resonant damping schemes with particular emphasis on providing a common framework for comparison of the PMD and the resonant shunted piezoelectric.

The following sections will attempt to address these goals in the light of practical damping enhancement.

5.4.2 System Damping Tests with Proof Mass Dampers

5.4.2.1 Tests with Optimally Tuned Proof Mass Dampers

For the optimally tuned PMD tests, the damper described in Section 4.3.1 was placed at node 11 in Figure 5.7d replacing the dummy mass used in the calibration tests. The PMD #1 was connected to the truss with the main axis oriented in the z direction in a position to damp the horizontal bending modes. As described in Section 4.4.2 and Figure 4.10, the mechanical PMD was embedded within an electrical state feedback scheme which provided electronic stiffness and damping to the inherent mechanical stiffness and damping of the device. This enabled the device to be easily tuned to the first two horizontal bending modes of the truss. The PMD could not be tuned to the third mode because of power limitations of the electrical drive system.

The first test in this series was to tune the damper to the first bending mode of the all-aluminum truss at 39 Hz. The optimal tuning of the damper to the test structure was found by visual inspection of the experimental transfer function. The transfer function from forcing at node 1 to acceleration in the z direction at node 1 was recorded and displayed by the Signology data acquisition system. The peak value of the displayed transfer function was minimized by comparing successive transfer functions while varying the feedback gains. The following PMD tuning parameters were obtained:

$$\delta_{opt\text{-}exp} = \frac{\omega_d}{\omega_h} = .955$$

$$r_{opt\text{-}exp} = \frac{C_d}{M_d \omega_d} = .2962$$

which compares favorably to the theoretical values obtained with a mass ratio, β, of 4.7%. This mass ratio implies an optimal tuning, δ = .955, and an optimal damping, r = 0.4238. The optimal damping is lower than expected. Beta is the ratio of damper mass to system modal mass not system total mass.

The results from the damping enhancement tests with the PMD tuned to the first mode are shown in Table 5.7 with comparisons to theory and in Table 5.8 with comparisons to the all-aluminum truss dynamic tests. As expected the PMD replaces the structural mode with two highly damped modes. The PMD is very effective on the mode to which it is tuned, giving

Truss with PMD Tuned to Mode 1

Frequencies (Hz)			
Mode	Experimental	Analytical model	
		Approximate	Exact
1a	35.71	38.09	36.49
1b	43.46	40.14	42.95
2	99.90	92.70	92.42
3	151.58	146.93	147.43
Damping Ratios (ζ)			
Mode	Experimental	Analytical model	
		Approximate	Exact
1a	.0619	.0819	.0727
1b	.0642	.0915	.0885
2	.0065	.0087	.0063
3	.0101	.0086	.0035

Table 5.7 Comparison of Experimental and Analytical Modal Frequencies and Damping Ratios for Truss with PMD Damper at Node 11 Tuned to the First Mode

Experimental Results for Baseline and PMD Damped Trusses

Frequencies (Hz)			
Mode	All-Aluminum	PMD tuned to Mode 1	PMD tuned to Mode 2
1a	39.23	35.71	38.60
1b		43.46	
2a	99.42	99.90	95.05
2b			106.58
3	149.01	151.58	150.82
Damping Ratios (ζ)			
Mode	All-Aluminum	PMD tuned to Mode 1	PMD tuned to Mode 2
1a	.0063	.0619	.0090
1b		.0642	
2a	.0048	.0065	.0413
2b			.0562
3	.0030	.0101	.0085

Table 5.8 Comparison of Experimental Frequencies and Damping Ratios for the Undamped All-aluminum Truss, the Truss with PMD Tuned to the First Mode, and the Truss with the PMD Tuned to the Second Mode

damping levels as high as 6.4% of critical. It does not provide this high level of damping to all the modes. There is almost no spillover of damping into the second mode. The third mode damping is the result of damper rattle at that high frequency and cannot be attributed to conventional PMD residual damping.

The experimental results can be seen compared to both the exact and approximate analytical pole locations in Table 5.7. The model modes reflect the presence of two modes at first bending due to the PMD, but these modes are more highly damped than the experimental modes identified by the RLLS algorithm. The exact model frequencies for the first mode are within 2.1% of the experimental frequencies. The frequencies for the higher modes reflect the errors present in the initial modelling of the all-aluminum truss from the previous section. The damping predicted from the pole locations is slightly higher than the experimental damping but correctly predicts the large increase in first mode damping due to the PMD. The errors in the damping in the lower and upper branches of the first mode, 17.4% error between the model and the experiment for the lower branch and 37.5% for the upper, could be manifestations of the RLLS identification algorithm since the modes are so closely spaced. The errors in damping represent a small absolute change in pole location, less than 2.5% in either branch.

Another point of interest is the "fallout" damping afforded to the second bending mode by the damper tuned to the first mode. The experimental second mode damping rose from 0.49% critical in the all-aluminum truss to 0.65% in the PMD damped truss in the second mode. The model correctly predicts this increase in the second mode damping as shown in Tables 5.3 and 5.7. The model damping rises from 0.40% of critical to 0.63% representing a 2.6% error from the experimental for the damping in the second mode of the PMD damped truss.

The approximate technique for estimating the frequencies and damping of the structural modes reproduced the frequencies found from the exact model pole locations very well. The maximum deviation from the frequencies of the model poles occurred in the upper branch of the first mode with a 6.5% error. The predictions for the modal damping ratios was consistently higher than the the damping associated with the model pole locations as it was in the all-aluminum truss tests. The predictions for the first mode damping compare well with the exact pole locations, however.

The maximum relative error between the exact and approximate damping coefficients occurs in the third mode with a relative error of 145% and an absolute increase from the exact to the approximate of 0.50% of critical.

The system transfer function for the first mode from the forcing point to the z direction acceleration at node 1 can be seen compared to the equivalent all-aluminum truss transfer function and the analytical model results in Figures 5.10a & b. The PMD decreases the amplitude of structural response in the first mode by over 22 db with a total system mass increase of only 3.2%. This damping efficiency is what makes PMDs so attractive as structural dampers.

The analytical transfer function for the damped and undamped first mode compares very well with the test results. The analytical model is consistently 2.5 DB below the corresponding test result which is well within the experimental error encountered in characterizing either the driver or the accelerometers. The close correlation between the experimental and theoretical transfer functions implies that the frequency domain modelling technique accurately models the PMD damped structure.

The PMD in node 11 was also tuned to the second structural mode via the feedback circuitry previously described. The damper parameters at optimal tuning were found as before by visual inspection of the experimental transfer function to be:

$$\delta_{opt\text{-}exp} = .977$$

$$r_{opt\text{-}exp} = .2720$$

which compares favorably to the theoretical values obtained if a modal mass ratio, β, of 2.4% is assumed. This mas ratio implies an optimal tuning, δ = .977, and an optimal damping , r = 0.306. The slightly lower value of the experimentally determined optimal r could be due to errors in the interpolation for the experimental values.

The results for the dynamic characteristics of the truss test modes are presented compared to the analytical model results in Table 5.9 and the all aluminum truss test results in Table 5.8. From this data, the effectiveness of the PMD in damping the second mode is evident. The damper tuned to the second mode increased the second mode damping from 0.49% of critical in the all-aluminum truss experiments to 4.1% and 5.6% for the upper and

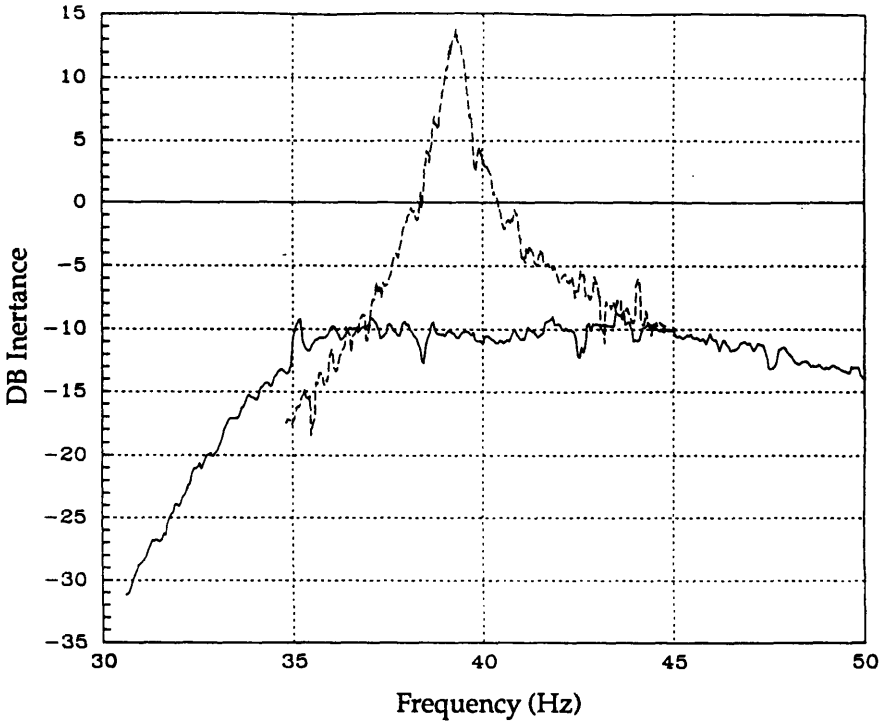

A) Experimental First Mode Transfer Functions, damped (solid) and undamped (dash)

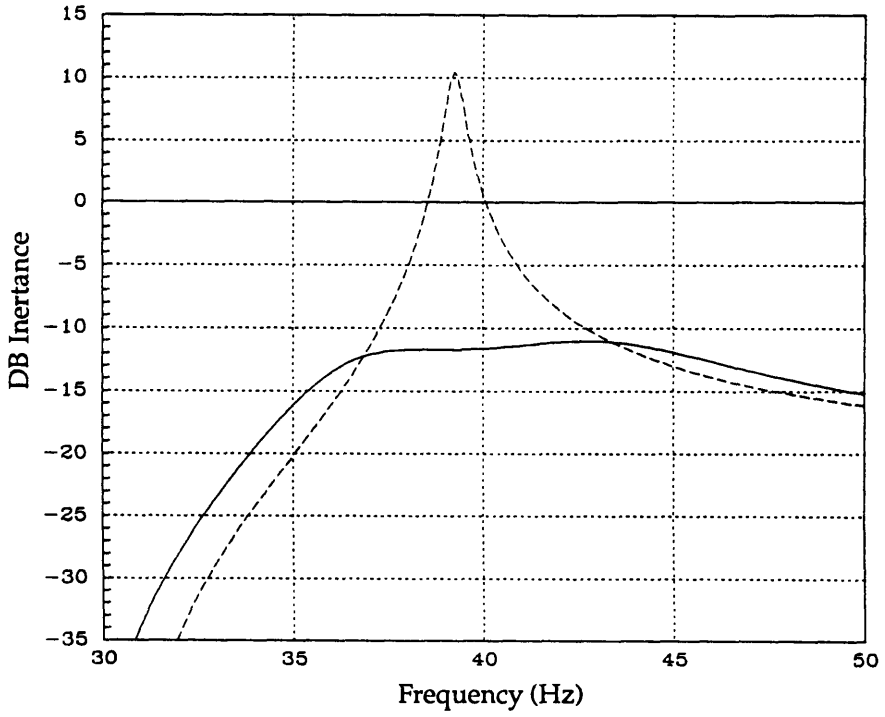

B) Analytical First Mode Transfer Functions, damped (solid) and undamped (dash)

Figure 5.10 Comparisons between the All-aluminum Truss and the Truss Damped by a PMD Tuned to Mode 1: Experimental (A) and Analytical (B) First Mode Responses

Truss with PMD Tuned to Mode 2

Frequencies (Hz)			
Mode	Experimental	Analytical model	
		Approximate	Exact
1	38.60	39.74	39.08
2a	95.05	89.31	89.19
2b	106.58	83.04	not found
3	150.82	147.12	147.42
Damping Ratios (ζ)			
Mode	Experimental	Analytical model	
		Approximate	Exact
1	.0090	.0070	.0066
2a	.0414	.0323	.0210
2b	.0562	.0590	not found
3	.0085	.0132	.0035

Table 5.9 Experimental and Analytical Modal Frequencies and Damping Ratios for the Truss with PMD Tuned to the Second Mode

lower branches of the second mode of the PMD damped truss, respectively. The damper has little effect on the first and third modes of the truss.

The experimental results for the truss frequencies and damping are compared to the model in Table 5.9. The model does not reflect the splitting of the second truss bending mode due to the tuning of the PMD. The model contains only one mode at second bending with a frequency approximately equal to the model frequency of the undamped truss. Although the PMD is optimally tuned to the *experimental* second bending mode, it is not optimally tuned to the *model* second mode because the model mode has a frequency different from the experimental mode. As a result, the PMD is tuned far above the second model mode and does not influence the global structural dynamics other than to increase the second mode damping by a small amount. In resonant damper applications where the damping device is tuned to a structural mode, the mode must be well modelled for the analysis to accurately predict the global damping. This is due to the relatively narrow

frequency range of the effectiveness of the resonant devices for providing damping.

The system transfer function from the driver to the horizontal acceleration at node 1 can be seen compared to the analytical model and the all-aluminum truss results in Figures 5.11a & b. The experimental transfer function depicts the 20db reduction in modal amplitude from the undamped to the PMD damped truss. The model mode is 10 Hz below the actual mode so a PMD tuned optimally to the experimental second mode gives only secondary effects for the model second mode.

These tests on the effectiveness of proof mass dampers at optimal tuning yield some interesting insights into some practical aspects of damping enhancement for space structures. First, the proof mass dampers are mass efficient contributing an average of 6.3% critical damping for a total system mass ratio of about 2.7% with little variation of the base structures modes. This mass did not include amplifier and feedback circuitry masses. Secondly, it is difficult to tune the resonant dampers accurately to the truss using the analytical model alone since small variations in the model produce large variations in the damping levels realized on the truss. This necessitates some sort of manual tuning scheme to get the most out of the dampers. More on the sensitivity of the system damping levels to parameter variation will be presented in the next section.

5.4.2.2 Frequency and Damping Sensitivities to PMD Parameter Variation

Tests were conducted on the truss structure with the PMD parameters tuned in the vicinity of but not at optimum tuning for the first truss bending mode. Once the optimal tuning parameters had been determined in the previous test, the tuning parameters of the PMD were varied in a pattern about this optimum. The purpose of the test was to determine the effect of mistuning on the damping afforded by the resonant device. Since tuning is required with resonant devices and the structural parameters can vary from the model used in analysis, it is useful to determine the sensitivity of the truss damping levels to mistuning.

These tests where conducted using the techniques described for the optimum tuning experiments. The feedback tuning circuit was used for the

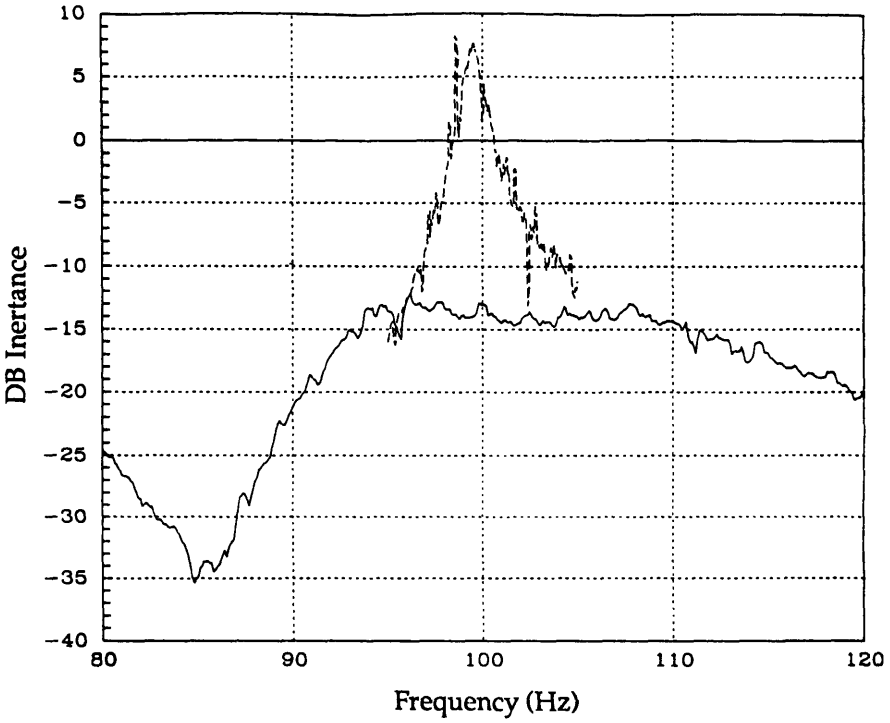

A) Experimental Second Mode Transfer Functions, damped (solid) and undamped (dash)

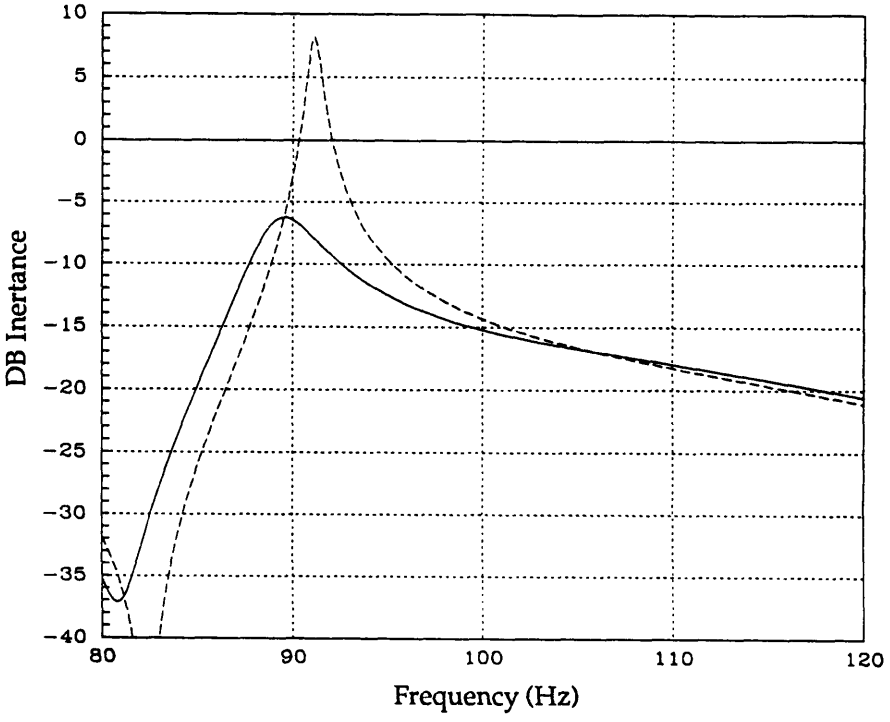

B) Analytical Second Mode Transfer Functions, damped (solid) and undamped (dash)

Figure 5.11 Comparisons between the All-aluminum Truss and the Truss Damped by a PMD Tuned to Mode 2: Experimental (A) and Analytical (B) Second Mode Responses

parameter variation. This test was only conducted for parameter variation about the first mode. In one variation series, the damper was set to the optimum frequency tuning, δ, and the damper's internal dissipation, r, was varied from underdamped to overdamped. In the other series, the damper was set to the optimum internal dissipation and the frequency tuning was varied from below to above optimal.

The series of transfer functions associated with the first series of damper dissipation parameter, r, variations is presented in Fig. 5.12a and the second series with frequency tuning variation is shown in Fig. 5.13a. Several trends are apparent. First, at optimal frequency tuning, the transfer function changes with increasing r from two undamped modes through optimal damping to one undamped mode as the damper internal dissipation rises. The root locus for the identified system modes for r variation is shown in Figure 5.12b alongside the theoretical root locus calculated from the denominator of Equation (3.50). A mass ratio of 4.7% was used in this calculation. The experimental roots were identified using a Recursive Lattice Least Squares (RLLS) routine on the data from the first parameter variation test. As can be seen the RLLS routine has a difficult time tracking the damped root after frequency coalescence, preferring to fit the visible mode with two lightly damped poles rather than a heavily damped mode superimposed upon a lighter damped one. This is a common problem for identification schemes.

Some interesting trends are also visible in the frequency tuning variation tests at optimal damper internal dissipation levels. The transfer functions and root locus associated with this test are shown in Figures 5.13a and 5.13b, respectively. As the tuning goes from below optimal to above optimal the system transfer function lowers on the right to the optimal value then rises on the left. The primarily structural mode moves out from the imaginary axis and becomes more highly damped as the PMD mode becomes less damped and eventually replaces it. The experimental modes loosely follow this trend since there is a difficulty in the identification of the modes from the experimental data. As seen in the transfer functions, a small variation in the tuning parameters can result in a large increase of system response for PMDs.

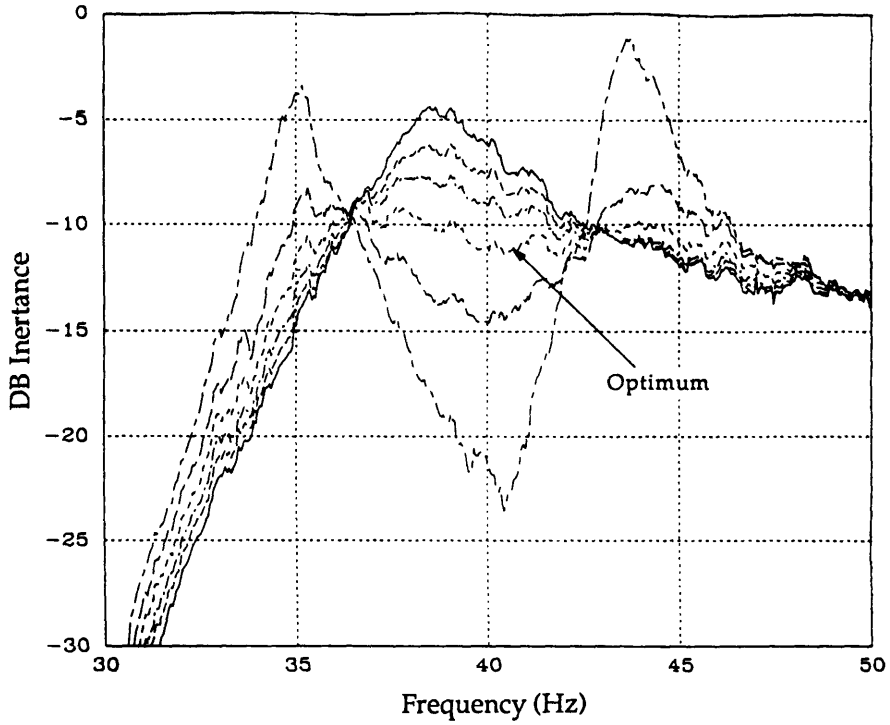

A) First Mode Transfer Functions at Various Values of the Dissipation Parameter, r

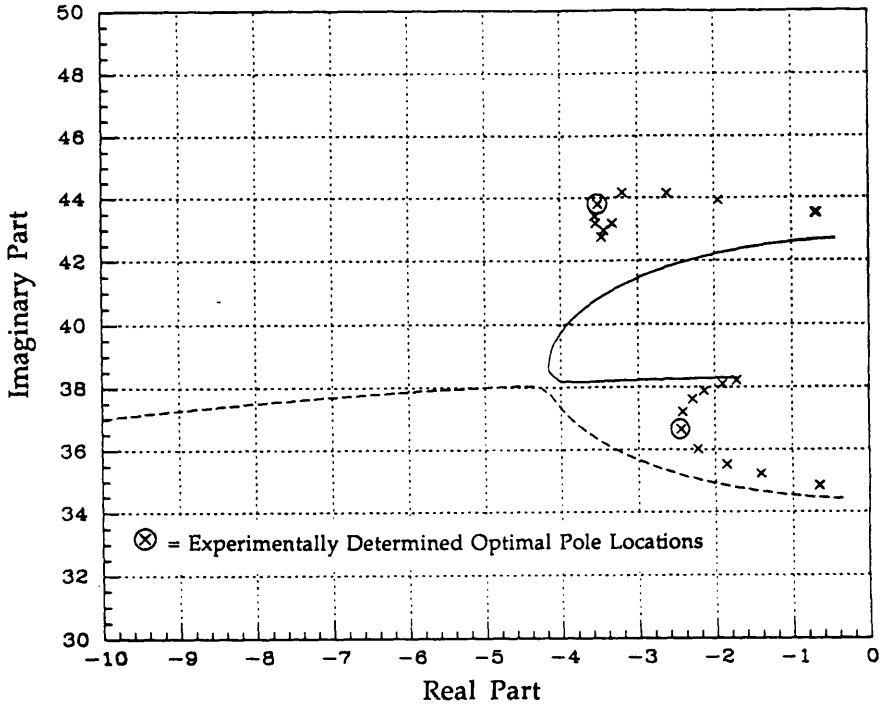

B) First Mode Root Locus: Experimental (symbol) and Analytical (line) Poles at Various Values of the Dissipation Parameter, r

Figure 5.12 First Mode PMD Dissipation Parameter Variation from r = 0.04 (widely spaced modes) to r = 0.60 (single mode)

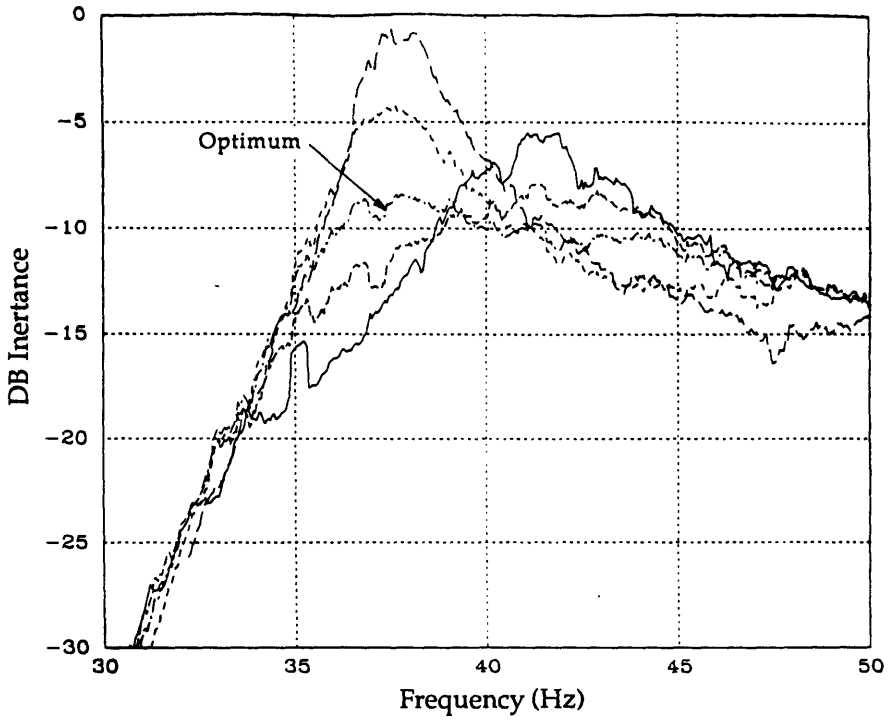

A) First Mode Transfer Functions at Various Values of the Frequency Tuning Parameter, δ

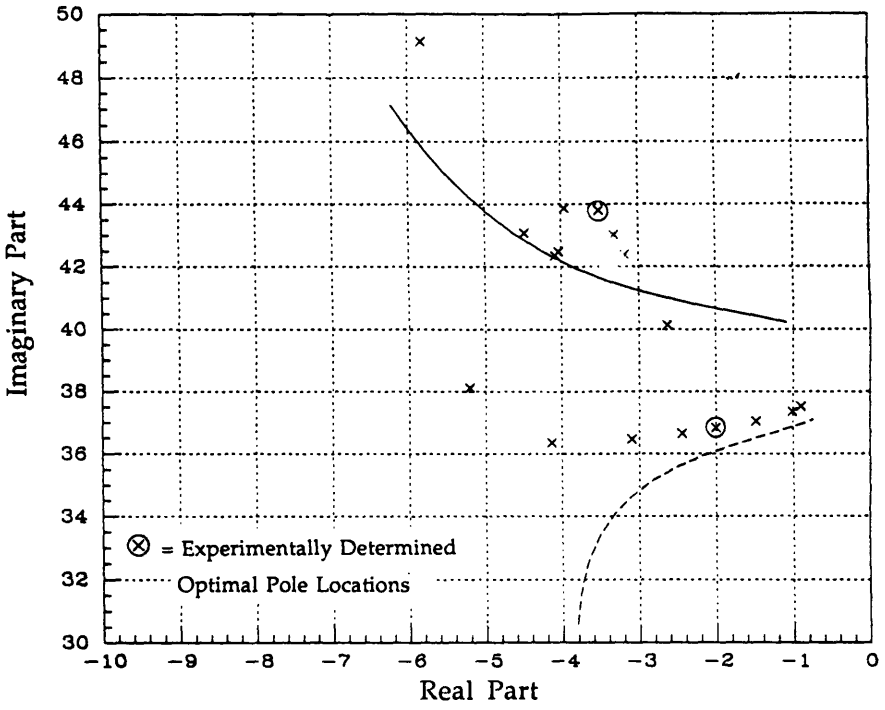

B) First Mode Root Locus: Experimental (symbol) and Analytical (line) Poles at Various Values of the Frequency Tuning Parameter, δ

Figure 5.13 First Mode PMD Frequency Tuning Parameter Variation from $\delta = 0.806$ (single mode above 40 Hz) to $\delta = 1.159$ (single mode below 40 Hz)

5.4.3 System Damping Tests with Resonant Shunted Piezoelectrics

5.4.3.1 Tests with Optimally Tuned Resonant Shunted Piezoelectrics

The piezoelectric truss members described in Section 4.3.2 were used as elements of a resonant damping enhancement scheme for space structures. Four piezoelectric truss members replaced 4 members in the central bays of the all-aluminum truss in the exact configuration used in the shorted piezoelectric experiments described in Section 5.3.4 and Fig. 5.7c. The truss was otherwise undamped and driven by a PMD driver at node 1. The piezoelectrics where shorted with an electrical circuit which, when combined with the inherent capacitance of the piezoelectric, produced a resonance which could be tuned to a structural mode as described in Chapter 3, Section 3.4.4.

The electrodes of the piezoelectrics were arranged as for the resistive shunting case. The truss members on opposite sides of the truss were wired with opposite polarity so as to cause the members on one side to expand as the others contracted. The four piezoelectric members were thus wired to create one combined piezoelectric damper which was sensitive to bending. This total damper was shunted with a variable resistor and variable inductor in series to create, along with the total inherent capacitance of the piezoelectric, a resonant circuit coupled to the structure through the energy transformation properties of the piezoelectric. Experiments were conducted to determine the natural frequencies and damping ratios of the truss when the piezoelectric damper had been optimally tuned to the truss structure's first or third bending modes. Tests were not preformed on the second structural mode since in this mode there is little bending strain energy in the central 2 bays of the structure. The tuning was done in accordance with the guidelines given in Section 3.4.4 .

The first resonant piezoelectric experiment entailed tuning the damper to the first structural bending mode for the shorted-piezoelectric structure at 40 Hz. The shorted piezoelectric structure is the comparable undamped system for these tests since it reflects the piezoelectrics inherent stiffness and damping without the electrical interaction under study. The electrical tuning which was found to give the lowest amplitude of structural response was at an inductance of 7.29 Henries and resistance of 248.7 Ohms along with the

inherent capacitance of the 4 piezoelectric members of 2.17 μFarads. The resulting parameters are:

$$\delta_{opt\text{-}EXP} = 1.0149$$

$$r_{opt\text{-}EXP} = .1336$$

Since δ is found to be larger than 1, these results verify the contention made in Chapter 3 that the optimum condition is to tune the shunted piezoelectric resonance above the resonant frequency of the structure. These tuning criteria correspond to the optimum tuning conditions for a system with a coupling coefficient, K_{31}, of 0.173. This is in fair correlation with the value of K_{31} presented in the resistive shunting case (Section 5.3.4). In that experiment, the value of K_{31} was determined to be 0.146. The experimentally determined damping parameter is lower than the optimum value expected with a K_{31} of 0.173 determined from the experimental tuning ratio. The expected value of the optimal dissipation parameter, r, is 0.24. The damping parameter is very sensitive to changes in the frequency tuning ratio. Since the tuning can only be pinpointed to within a few tenths of a hertz this can lead to large variations in $r_{opt.}$ The lower experimental value of r implies a smaller coupling coefficient and less damping capability than would be expected from the experimental value of the frequency tuning parameter, δ.

The results for the truss structure frequency and damping ratios can be seen compared to the other piezoelectric tests in Table 5.10 and compared to the analytical model, both exact and approximate methods, in Table 5.11. The resonant shunted piezoelectrics increase the first mode system damping from 1.1% critical in the shorted case to an average of 5.5%. This damping increase is only apparent in the first mode just as in the PMD case. The third mode damping ratios have increased due to interaction between the two modes shifting the third mode toward unobservability. Consequently, the identification routine attributes this lessened amplitude response to a virtual damping which doesn't really exist in the structure.

The experimental results are compared with the model results in Table 5.11. The model reflects well the changes in the dynamic characteristics of the truss caused by tuning the RSP to the first truss mode. In the experiments, the piezoelectrics are optimally tuned to minimize the amplitude of the system transfer function. The experimentally determined tuning parameters were then used in the analytical model. Since the analytical model

Experimental Results for Baseline and RSP Damped Trusses

Frequencies (Hz)			
Mode	Shorted Piezoelectrics	RSP tuned to Mode 1	RSP tuned to Mode 3
1a	39.41	38.31	39.49
1b		43.66	
2	99.05	99.28	99.15
3a	145.47	145.15	144.41
3b	152.76	151.98	151.99
Damping Ratios (ζ)			
Mode	Shorted Piezoelectrics	RSP tuned to Mode 1	RSP tuned to Mode 3
1a	.0119	.0418	.0108
1b		.0599	
2	.0062	.0056	.0057
3a	.0095	.0113	.0132
3b	.0115	.0100	.0121

Table 5.10 Comparison of the Experimentally Determined Modal Frequencies and Damping Ratios between the Baseline Shorted-piezoelectric Truss and the Trusses with Resonant Shunted Piezoelectrics (RSPs) Tuned to the First or Third Mode

Truss with RSP Tuned to Mode 1

Frequencies (Hz)			
Mode	Experimental	Analytical model	
		Approximate	Exact
1a	38.31	35.99	34.72
1b	43.66	43.57	43.43
2	99.28	92.39	92.16
3a	145.15	145.75	145.99
3b	151.98	138.48	not found
Damping Ratios (ζ)			
Mode	Experimental	Analytical model	
		Approximate	Exact
1a	.0418	.0889	.0580
1b	.0599	.0401	.0252
2	.0056	.0071	.0054
3a	.0113	.0077	.0044
3b	.0100	.0091	not found

Table 5.11 Experimental and Analytical Modal Frequencies and Damping Ratios for Truss with RSP Tuned to the First Mode

frequencies do not necessarily match the experimental truss frequencies, the tuning parameters which produces optimal results on the experimental truss will not necessarily produce optimal results in the model. This accounts for the discrepancies between the actual and the model first mode frequencies and damping. The model predicts higher damping in the lower branch of the first mode as opposed to the experimentally obtained result of higher damping in the upper branch, 6.0% of critical. There was little damping "spillover" to the second and third truss bending modes in either the model or the experiment. This lack of spillover is typical for resonant dampers.

The system transfer functions of the first mode can be seen for the shorted and resonant shunted piezoelectrics compared to the analytical results in Figures 5.14a & b. The 15 db reduction in system response can be clearly seen in Fig. 5.14a. The optimally tuned piezoelectric damper can thus be used as a modal damper with performances comparable to a PMD's. While there is good agreement between the experimental and analytical undamped truss transfer functions, the damped transfer functions differed greatly. The appearance of two widely spaced modes in the damped analytical transfer function implies that the model demonstrates a higher coupling coefficient and hence more damper authority than does the experiment. Since the optimum tuning depends on the value of the coupling coefficient, this mismodelling leads to inaccurate tuning in the model as opposed to the optimal tuning demonstrated by the experimental transfer function. In all, the resonant shunted piezoelectrics were clearly effective as modal dampers. More work needs to be done on modelling the structural aspects of the piezoelectric truss members.

Experiments were also conducted with the piezoelectric truss members tuned to the third bending mode of the truss. All arrangements were as before for the first mode tuning. The variable inductor and resistor described in Section 4.4.3 were employed to obtain the optimum tuning conditions. These were found to occur with the inductance at 0.51 Henries, the resistance at 19.5 Ohms, and the capacitance as before. The damping parameters are difficult to calculate since there are two modes in the vicinity of 150 hertz which were simultaneously damped.

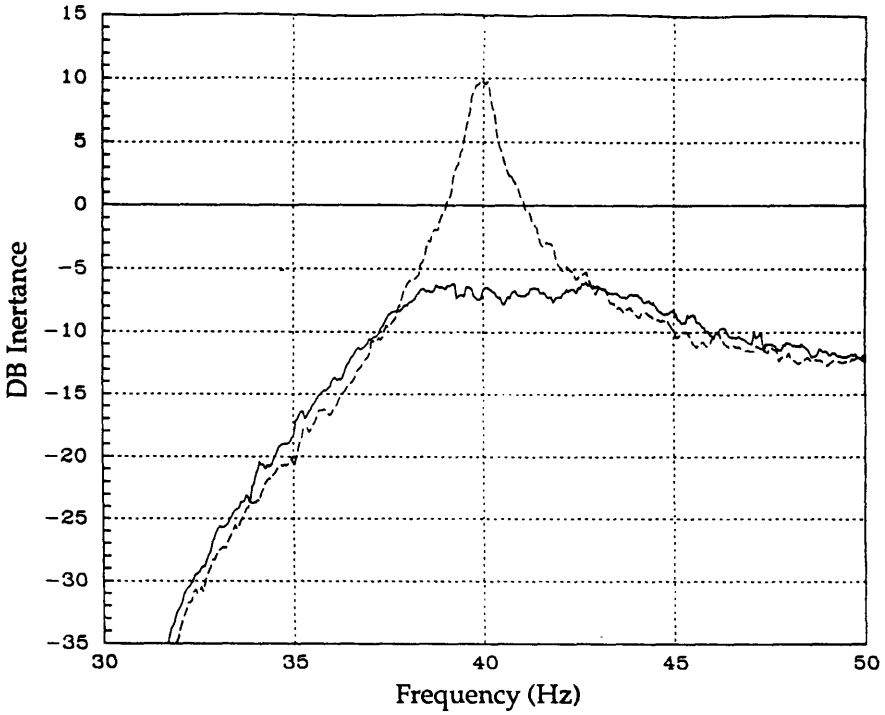

A) Experimental First Mode Transfer Functions, damped (solid) and undamped (dash)

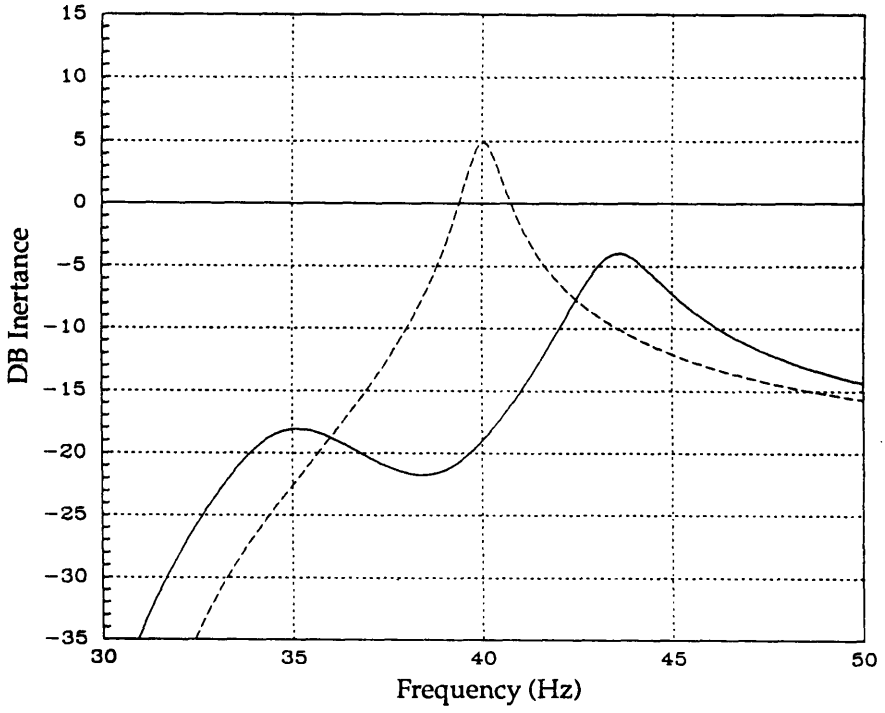

B) Analytical First Mode Transfer Functions, damped (solid) and undamped (dash)

Figure 5.14 First Mode Transfer Functions for Truss with Resonant Shunted Piezoelectric (RSP) Damper tuned to Mode 1 compared to Baseline Shorted Piezoelectric Truss: Experimental (A) and Analytical (B)

If we use the highest mode as a reference:

$$\delta_{opt\text{-}EXP} = 0.993$$

$$r_{opt\text{-}EXP} = 0.0402$$

These values reflect the fact that the electromechanical coupling coefficient is low for the third mode. This is so for two reasons. First, the third mode has relatively less strain energy in the central 2 bays of the truss than the first mode. Secondly, the modeshapes for the third bending modes in the vertical and horizontal directions have shifted toward unobservability from the piezoelectric truss members making the coupling coefficient even smaller than would be expected.

The experimental results can be seen compared to the other piezoelectric cases in Table 5.10 and with the analytical model in Table 5.12. Although the third mode split makes it hard for the analytical model to track the damping, a few points are clear. The shunted piezoelectric does increase the damping in the experimental truss in the third modes by about 0.4% of critical for the lower mode and about 0.1% for the upper. This is probably because the piezoelectric is more strongly coupled to the lower mode. It is interesting to note that the optimum internal damping level, r, was very low in this case, implying, from Equation (3.60), a low coupling between the piezoelectric and the structure.

The model for the RSP tuning to the third truss bending mode suffers, as does the second mode PMD tuning, from inaccurate modelling of the mode to which the RSP was to be tuned. As a consequence, the experiment exhibits two modes where the model exhibits only one. The model does predict an increase in the damping of the third mode from 0.4% in the shorted piezoelectric calibration test presented in Section 5.3.4 to 2.07% for the RSP tuned to the third mode. Thus, although the double mode typical of resonant dampers does not appear, the increase in damping afforded by a mistuned damper does.

The experimental and analytical system transfer functions for the third mode can be seen in Figures 5.15a & b. The 5 db reduction in third mode amplitude is clearly visible in Fig. 5.15a. As expected the model does not reflect the coupling of the horizontal and vertical third bending modes which result in a much broader experimental transfer function. The location and amplitude of the lower of the two modes is reflected accurately in the model.

Truss with RSP Tuned to Mode 3

Frequencies (Hz)			
Mode	Experimental	Analytical model	
		Approximate	Exact
1	39.49	40.54	39.93
2	99.15	91.26	91.02
3a	144.41	132.37	139.55
3b	151.99	147.29	150.54
Damping Ratios (ζ)			
Mode	Experimental	Analytical model	
		Approximate	Exact
1	.0108	.0128	.0121
2	.0057	.0082	.0062
3a	.0132	.0852	.0207
3b	.0121	.0250	.0155

Table 5.12 Experimental and Analytical Modal Frequencies and Damping Ratios for the Truss with RSP Tuned to the Third Mode

As was evident in the first mode test, the model exhibits a higher coupling coefficient. The damped model therefore exhibits the mode splitting associated with higher authority resonant dampers.

The low damping authority of the experimental RSPs in the third mode can be explained by two factors. First, the stain energy in the third mode is not as concentrated into the central 2 bays as it is in the first mode. Secondly, in the experimental truss the horizontal bending modes in the vertical and horizontal planes coupled to produce two modes shifted from these. These shifted modes were not as observable from the piezoelectrics as a pure horizontal mode would have been.

In the course of the resonant piezoelectric experiments, several lessons were learned for the practical implementation of this damping scheme. There were several difficulties associated with the tuning process. Since the native piezoelectric capacitance is so low, a very large inductance must be used to get an electrical resonance in the range of the structural modes.

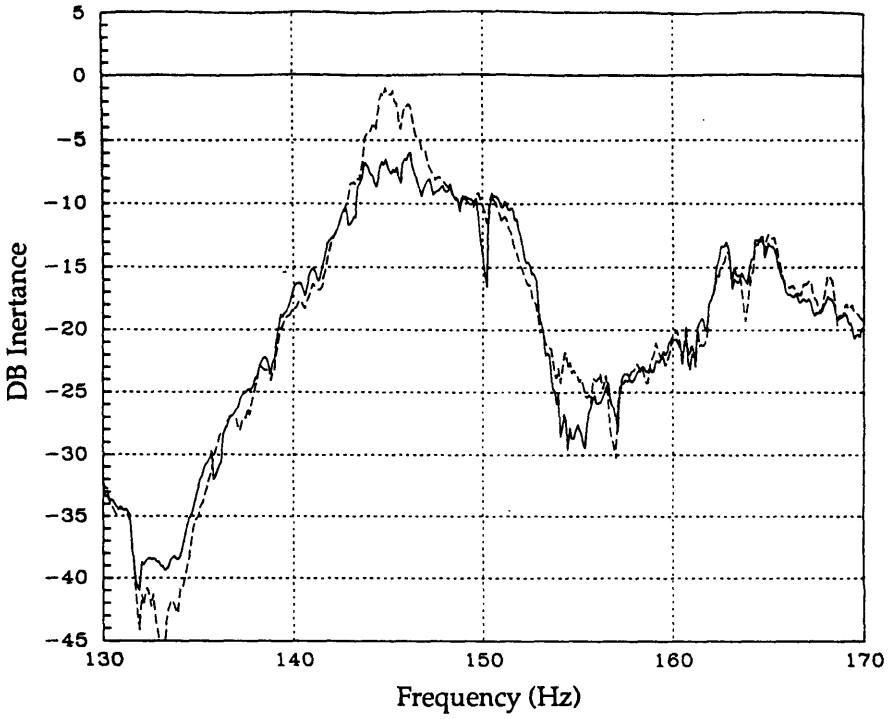

A) Experimental Third Mode Transfer Functions ,damped (solid) and undamped (dash)

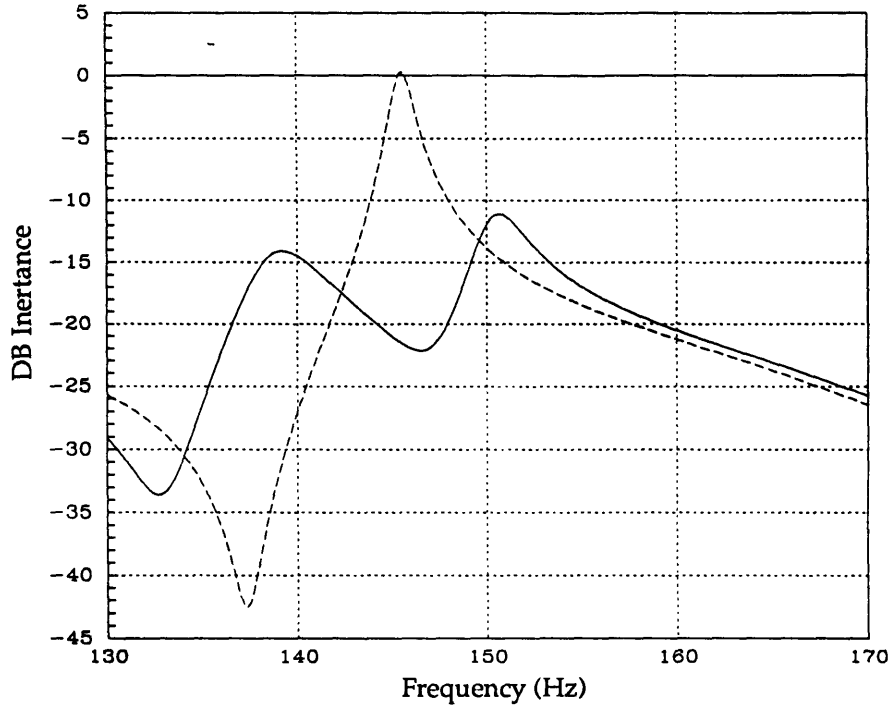

B) Analytical Third Mode Transfer Functions, damped (solid) and undamped (dash)

Figure 5.15 Third Mode Transfer Functions for Truss with Resonant Shunted Piezoelectric (RSP) Damper tuned to Mode 3 compared to Baseline Shorted Piezoelectric Truss: Experimental (A) and Analytical (B)

Putting more capacitance in the electrical circuit cuts the performance. Large inductors (greater than 5 Henries) are commercially available. These inductors usually posses inherent resistance which is above the optimum value. The solution is to use high-q (low resistance) inductors to get the inductance while preserving low resistance. Another option which was partially employed is to use active inductor circuits based on high voltage amplifiers. This method was employed to make the variable part of the inductor used in the tuning experiments. In the experiments, there was a large high-q inductor with a small variable active inductor in series. Since active inductors ideally posses no resistance, this helped meet the tuning requirements for the damping parameter, r.

The next step in the investigation of shunted piezoelectrics as damping elements in space structures is to determine the sensitivities of the global system damping to mistuning.

5.4.3.2 Sensitivities to Resonant Shunted Piezoelectric Parameter Variations

Test were conducted with the resonant shunted piezoelectric tuned at various values in the vicinity of the optimum tuning for the first bending mode. The variable tuning was achieved using the tuning electronics described in Section 4.4.3 using the testing techniques common to all piezoelectric tests. The purpose of the test was to determine the sensitivity of the truss first mode damping level to variations in the resonant shunted piezoelectric's tuning parameters away from optimum. This information is important since optimum tuning can rarely be accomplished from the model alone; and deviations from optimum values can result in great losses in damper performance.

Two variation tests were conducted. The first involved setting the inductor to obtain the optimum δ value and then varying the resonant circuit resistance, R. The second test entailed setting the damper to the optimum value of the electrical circuit resistance and varying the inductor value from below to above optimum, thus varying the frequency tuning ratio. The results from these experiments are thus comparable to the results for the parameter variation of the PMD.

The system transfer functions which resulted from the first variation of the damper resistance can be seen in Fig. 5.16a. The poles corresponding to these systems can be seen plotted against the theoretical root locus obtained from the denominator of Equation (3.50) in Figure 5.16b. The value of the coupling coefficient used in the root locus was found in the resistive shunted truss tests to be $K_{31} = .1466$. The resonant piezoelectric exhibits the same mode coalescence present in the PMD variation. Increasing damping from below optimum to above results in the convergence of two relatively undamped modes into a single damped mode and finally into an single undamped mode. As explained before in Section 5.4.2.2, the experimental poles do not track the damped mode after coalescence due to inaccuracies in the RLLS identification routine. Just as with the PMD, the single undamped mode is fitted with two undamped poles side by side resulting in a good fit to the transfer function data but not reflecting the actual dynamics.

The transfer functions and system poles which result from the frequency tuning variation at optimal resistance are shown in Figures 5.17a and b respectively. As the damper frequency is changed from below to above optimal, the system mode drops on the right then rises on the left. The system main structural pole moves out from the imaginary axis while the lower damper pole moves up to replace it just as for the equivalent variation of the PMD. Thus although the tuning requirements for the RSP are different from the proof mass damper, the resonant shunted piezoelectric shares some some fundamental properties with it. Among these are the sensitivities to parameter variations and dependance on a single parameter for determination of the damper performance. For PMDs, this is the mass ratio, β; for piezoelectrics, it is the generalized electromechanical coupling coefficient, K_{31}.

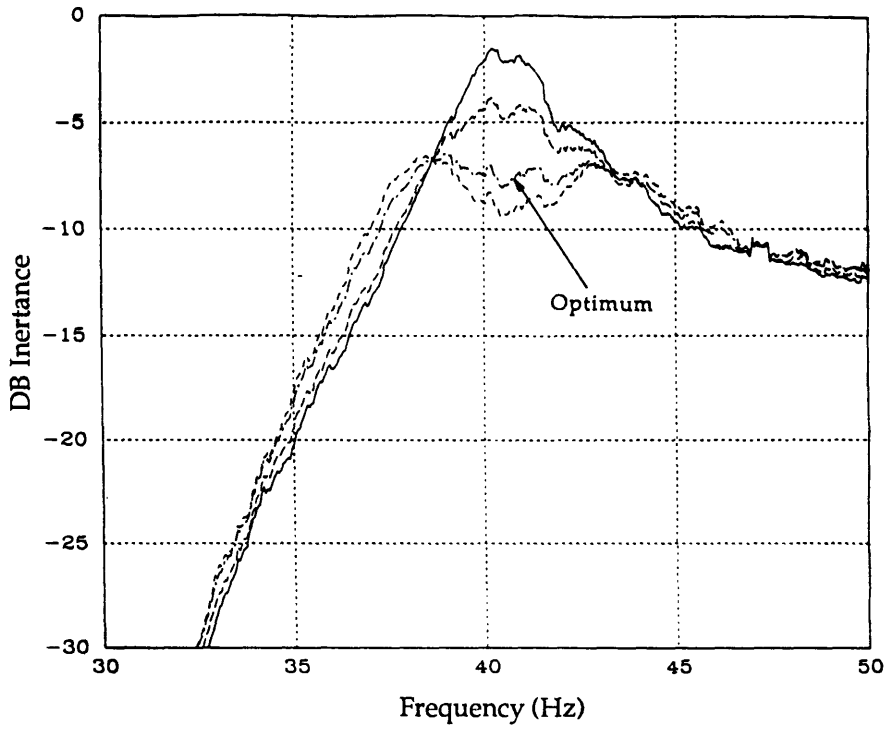

A) First Mode Transfer Functions at Various Values of the Dissipation Parameter, r

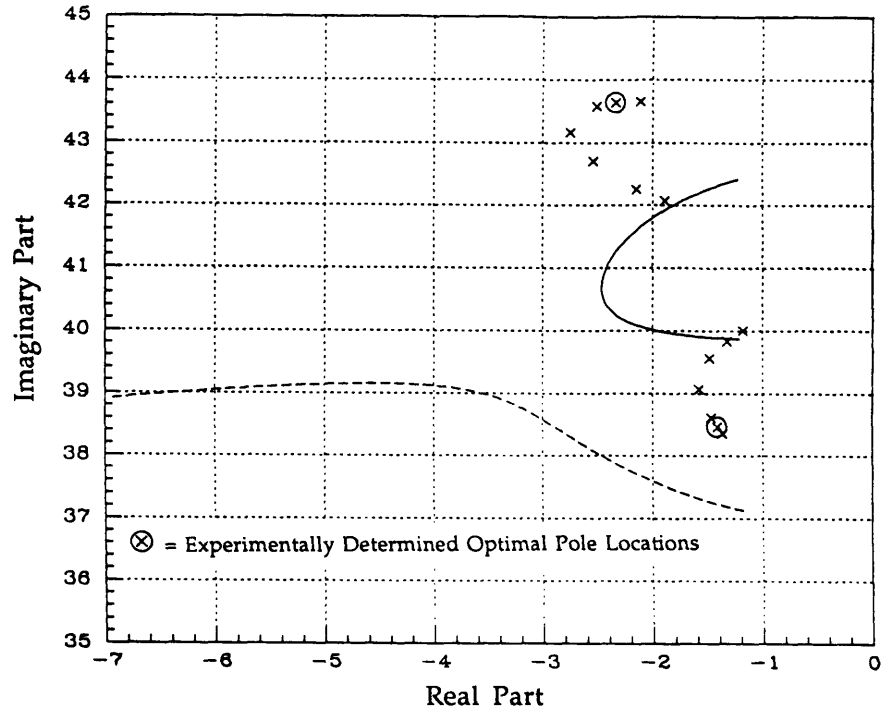

B) First Mode Root Locus: Experimental (symbol) and Analytical (line) Poles at Various Values of the Dissipation Parameter, r

Figure 5.12 First Mode RSP Dissipation Parameter Variation from r = 0.12 (widely spaced modes) to r = 0.41 (single mode)

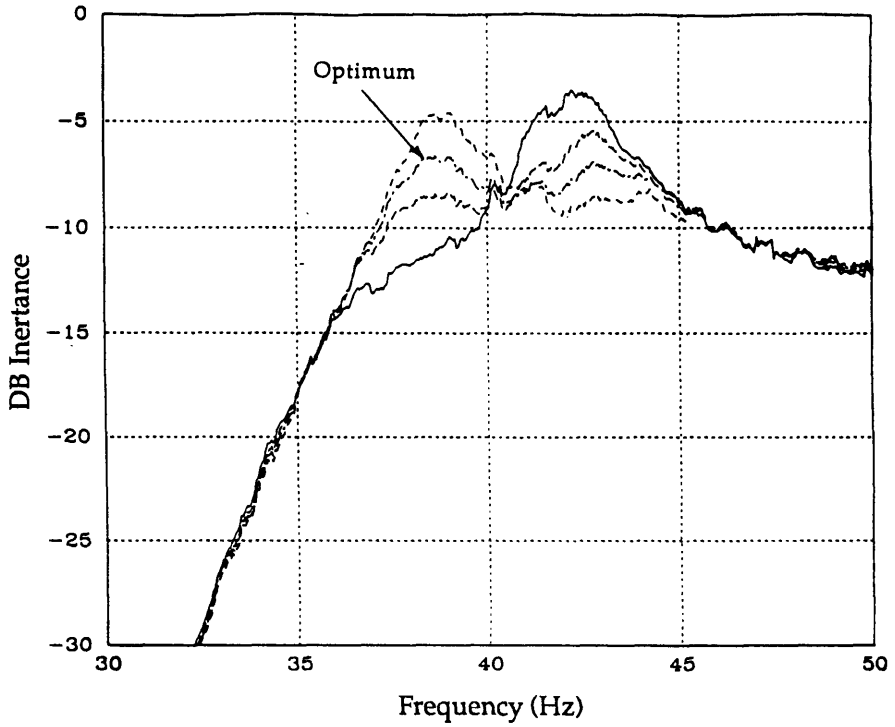

A) First Mode Transfer Functions at Various Values of the Frequency Tuning Parameter, δ

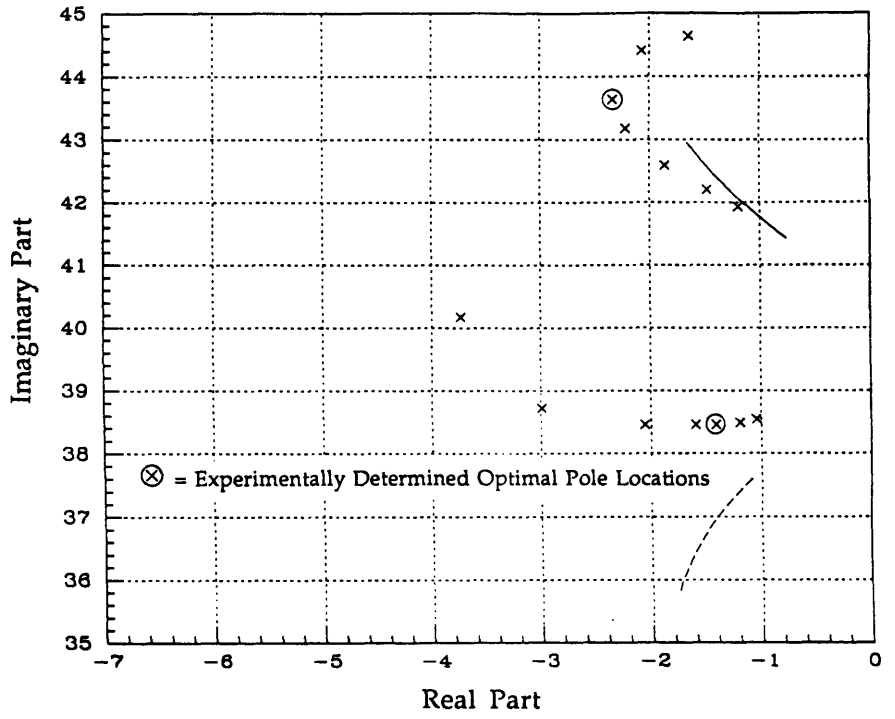

B) First Mode Root Locus: Experimental (symbol) and Analytical (line) Poles at Various Values of the Frequency Tuning Parameter, δ

Figure 5.13 First Mode RSP Frequency Tuning Parameter Variation from δ = 0.96 (single mode above 40 Hz) to δ = 1.041 (single mode below 40 Hz)

5.5 Conclusions

A complete testing plan has been executed with the purpose of investigating damping enhancement schemes on a realistic 10 bay truss structure. Various calibrations were preformed on the damping enhancement devices to ensure the accuracy and comparability of the system results. The nominally undamped systems were characterized for their frequencies and damping to serve as comparisons with the damped cases and to validate the frequency domain modelling technique presented in Chapter 2. Finally, two resonant damping schemes were implemented on the experimental truss. The first scheme implemented entailed a space realizable classical proof mass damper; the second employed the resonant shunted piezoelectric truss member.

Several effects were noticed for the base truss structure. This first was a phenomena referred to as mode splitting which involved the interaction between the two identical modes in vertical and horizontal directions. This effect occurred at the higher frequencies. Another effect was that introducing softness in a limited section of the truss (as with the inclusion of plastic members) has lessoning effects on the higher modal frequencies. Any material damping introduced in such a way will also contribute less to the higher structural modes.

The PMD and resonant shunted piezoelectric were shown to be effective single-mode dampers. The PMD implementation was shown to be able to achieve 6.5% critical damping in the first mode with a mass ratio of only 2.7% (not including tuning circuitry and amplifiers). The resonant shunted piezoelectric implementation was shown to be comparable with the PMD in terms of achieving system damping. The piezoelectrics raised the first mode system damping to 6.0%. Since this incurred a mass ratio of only 2.7% of the total system mass, the resonant piezoelectrics are competitive with PMDs in mass efficiency and much simpler mechanically.

Finally, the experiments conducted with mistuned resonant dampers revealed the sensitivities of the system total damping to variations of the damper parameters. The damping enhancement obtainable was found to decrease sharply with deviation from the optimal tuning parameters. The system trends associated with a given mistuning were found to be the same

for both the PMD and the RSP. The trends provide useful clues in how to correct the tuning toward optimum.

The concept of piezoelectric damping was verified for both resistive and resonant shunting. The shunted piezoelectric schemes were implemented on the truss and shown to be a viable alternative to either viscoelastic material damping methods in the resistive shunting case or PMDs in the resonant shunting case.

Chapter 6
Conclusions and Recommendations

6.1 Summary

The intent of the research presented is to further advance the area of passive damping augmentation for space structures. Toward this goal, a framework for the analysis of damped systems with frequency dependant properties has been developed along with models for the most promising damping augmentation schemes. These schemes have been implemented on a realistic three dimensional structure in a space realizable fashion to illuminate the key difficulties associated with passive damping augmentation on complex structures.

The first step towards the development of a passive damping methodology is consolidation of the sundry and disparate damping enhancement mechanisms into a common analytical framework. This framework for damped systems is provided by Tellegen's Theorem which has been adapted to structural systems in this research. The framework is specialized to the frequency domain to accommodate the frequency varying impedances of common structural elements such as beams, viscoelastic materials, proof mass dampers, and shunted piezoelectrics. Simple techniques for calculating the damping and frequencies of complex damped structures were developed to aid in damping design.

Models for three general types of damping augmentation devices were presented. These devices were complex modulus viscoelastic materials, the classical proof mass damper, and a new technique referred to as shunted piezoelectrics. Shunted piezoelectrics involved shunting a complex impedance across the electrodes of a piezoelectric material to achieve energy dissipation. If a resistor is the shunting element, then the material is comparable to a viscoelastic; and if the shunting impedance is resonant, the device is conceptually similar to a resonant proof mass damper.

An experiment was designed to test these damping enhancement concepts on a representative structure. The experiment involved dynamic tests for frequency and structural damping of a 10 bay box truss. Preceding the

primary structural tests, a series of calibration tests were performed on the actuators and undamped truss to provide information on the initial dynamic properties of these items. Following these tests, the damping of the truss was augmented by two resonant damping schemes: proof mass dampers and resonant shunted piezoelectrics.

The proof mass damper (PMD) implementation produced significant increases in structural damping in the two cases of the PMD tuned to the first and second mode. The frequency domain analytical model predicted the PMD performance accurately for the fist mode tuning. The effects of damper mistuning were measured and found to agree with analytically predicted trends.

Finally, experiments were conducted with the resonant shunted piezoelectric (RSP) truss members tuned to the first and third structural bending modes. The tuning of the members was also varied in the vicinity of the first mode as with the PMD. The tests validated the ability of resonant shunted piezoelectrics to damp the structure. The performance of the RSP depended strongly on the coupling between the shunted piezoelectrics and the mode shape to be damped. The RSPs were found to exhibit tendencies comparable to those of PMDs in the experiments on damper mistuning.

6.2 Conclusions Pertinent to Tellegen's Theorem and Frequency Domain Modelling

In the second chapter of this report, a framework was presented within which to analyze the dynamics of mechanical systems. The framework, known as Tellegen's Theorem, has been previously applied to nonlinear, frequency dependant dissipative electrical systems. It was here applied to mechanical systems exhibiting these qualities by virtue of the analogy between Kirchoff's voltage and current laws and their mechanical equivalents, displacement compatibility and force equilibrium. The general form of this theorem can be specialized to the frequency domain where the structure is represented as a network of frequency dependant mechanical impedances.

This framework is general enough to incorporate most of the popular damping enhancement mechanisms such as viscoelastic materials or

resonant dampers which exhibit frequency dependant behavior. This behavior is encapsulated in the components complex impedance. These component impedances can be assembled into a global system impedance matrix which can be analyzed for its dynamic properties. The energy dissipation in a system was found to be dependant on two factors:

1) The real components of the elements of the global impedance matrix define in Chapter 2.

2) The motion at the nodes to which the real portions contribute.

These factors are most obvious in the approximate method for finding the loss factor of a general frequency dependant mechanical system presented in Equation (2.50). The energy dissipation is dependant on the real part of the quadratic product of the impedance matrix and the complex velocity modeshape. This product can be maximized by choosing elements with large real parts or by placing these elements in locations which contribute to the total by virtue of the large velocities present. For instance, if a damper which can be represented by a point impedance is chosen, it should be placed in a location of maximum absolute velocity since this will maximize the product. On the other hand if a device which spans two nodes is chosen, it should be placed in a location of maximum relative velocity between the nodes to maximize the quadratic product.

These two generic types of dampers were employed on the experimental truss. The implementation of the generic point damper was the PMD and the across damper was the piezoelectric truss member. In both cases, internal resonances in the damper were used to increase the real part of the impedance at the frequency which corresponded to a structural mode thus increasing the modal damping. The devices were also placed in positions so as to maximize the quadratic product with the modeshape. The PMD was placed at the tip which is the point of maximum amplitude vibration for a free-free structure, while the RSPs where placed in the location of maximum strain or relative velocity for the first mode, the central bays of the truss.

The approximate formula for the system loss factor can be used to calculate the contributions made to the system loss factor by a component without solving an eigenvalue problem. Just as in the case of the Rayleigh

Quotient for structural frequencies, the approximate formula for system loss factor is expressed as a ratio of two quadratic products depending on the assumed modeshapes. If the exact modeshapes are used the loss factor will be exact while if approximate modeshapes are employed an approximate value of the system loss factor will result. Just as the Rayleigh quotient, the formula for loss factor is insensitive to first order variations in the assumed modeshape. This leads to flexibility in the choice of modeshapes used in the initial stages of analysis.

6.3 Conclusions Pertinent to the Damper Models

Several frequency domain models for common dampers were developed in Chapter 3 to complement the frequency domain framework presented in Chapter 2. These models were for viscoelastic materials, proof mass dampers, and shunted piezoelectrics. The models were developed to show how elements of a damping system could be advantageously incorporated into the frequency domain framework.

The first damping method presented was viscoelastic materials. The general model for these materials, taken from Ref. [17], employs fractional powers of the Laplace parameter, s, to give the viscoelastic material properties complicated frequency dependance. These fractional powers of the Laplace parameter, while difficult to incorporate into time domain models, are simply incorporated into the mechanical impedance of the viscoelastic structural element.

The second damping device considered was the proof mass damper. This device can also be represented by a frequency domain impedance, in this case a point impedance. Parameters such as the natural frequency and internal damping of the PMD resonator can be tuned to a structural mode to minimize the modal response. The tuning parameters depend only on the value of the mass ratio, β, between the damper proof mass and the structural modal mass. In Chapter 3 a method was presented for representing the complex impedance of the PMD in terms of a simple dashpot which dissipated a equivalent amount of energy. This analysis illustrated the narrow frequency range of the damping afforded by the PMD as well as the damping afforded to modes to which it is not tuned.

The final damper model presented was for the shunted piezoelectric. In this damping device, the electrodes of a piezoelectric material are shunted by an electrical impedance designed to increase the structural damping by dissipating structural energy which is converted into electrical energy by virtue of the piezoelectric effect. The model developed for the arbitrarily shunted piezoelectric illustrated some important properties of these damping devices. The shunted piezoelectric material can be represented as having the impedance of the shorted electrode piezoelectric, a pure stiffness, modified by a nondimensional electrical term. The electrical term modifies the stiffness of the piezoelectric through the effect of the piezoelectric electromechanical coupling coefficient. This coupling coefficient is a material property of the piezoelectric.

Two cases of the shunting impedance were modelled in detail. The first involved a resister shunting the inherent capacitance of the piezoelectric. This resistive shunting creates a material with high loss factor as well as high stiffness, a combination of properties which make the resistive shunted piezoelectric potentially more effective as a damper than viscoelastic materials which suffer from their low stiffness. The material loss factor of the resistive shunted piezoelectric can be optimized at a certain frequency by appropriate choice of the shunting resister.

The second application of shunted piezoelectrics is the resonant shunted piezoelectric (RSP), where an inductor and resister are placed in parallel to the inherent piezoelectric capacitance to produce a resonant circuit which can be tuned to the structural resonance to minimize the modal response in a manner similar to the PMD. The frequency and internal damping parameters which minimize the structural response are only dependant on a quantity known as the Generalized Electromechanical Coupling Coefficient (GECC). This coefficient depends on the material coupling coefficient of the piezoelectric as well as the ratio of the modal strain energy which is present in the piezoelectric material. Two methods for tuning the RSP were presented. The first was based on minimizing the system steady state modal response, while the second was base on maximizing the magnitude of the real part of the system poles. In general, the first method produces slightly superior system steady state and transient response.

6.4 Damper Implementation and Experimental Design

Discreet damping devices were developed for experiments on a representative space structure. A 10 bay truss structure was designed and suspended in such a way as to exhibit free-free behavior in 3 dimensions with low damping. The damping devices implemented were the PMD and the Resonant Shunted Piezoelectric (RSP). The dampers were designed to be space realizable with no mechanical interface to the laboratory frame.

A linear proof mass damper/actuator was designed using electrical principles similar to those employed in loudspeaker design to produce a force linear with the current supplied to the devices drive coil. This linear PMD was manufactured with the magnetic portion of the device used as the proof mass to produce a high ratio of proof mass to total device mass. This ensured that the device was mass efficient. The actuator also possessed a high ratio of achievable force to total mass which is another measure of actuator mass efficiency.

Piezoelectric truss members were designed to replace the standard aluminum members of the truss. These piezoelectric truss members consisted of 3 components: the active piezoelectric cylinder, the mounting endpieces for truss inclusion, and a composite outer shell surrounding the piezoelectrics to increase the devices strength. The piezoelectrics enabled the member to expand or contract axially in response to an applied voltage. Four members were manufactured and placed in the central bays of the truss in order to actuate the bending modes of the truss.

Both the PMD and the RSP were augmented with feedback electronics to enable the tuning of the devices internal resonances. Position and velocity feedback was provide for the PMD to enable the device to be tuned to the structural model from 20 th 120 Hertz. The position and velocity feedback created an electric "spring" and "dashpot" which where dependant on the feedback gains.

The RSPs were equipped with an active variable inductor in series with the base inductance and a variable resister as the shunting impedance. The active inductor could be varied to effect the frequency tuning of the members while the variable resister could be changed to effect the damping of the internal electrical resonance.

In general for these resonant dampers, it was important to have the ability to tune the dampers to the structural modes after they have been installed since the dynamic properties of the structure are not known *a priori.*

6.5 Experimental Damper Performance and Comparison to Analysis

Tests were preformed on both the PMD and the piezoelectric truss members to ascertain the static forces which could be produced by the dampers/actuators and to calibrate the performance of the tuning circuitry described in Chapter 4. Calibration tests were also preformed upon the baseline truss structure in configurations containing all aluminum members and plastic or shorted piezoelectric central bay members. These tests were preformed to calibrate the model results to the undamped experimental results in the first bending mode. This was done in order to isolate the effect of the damping enhancement devices on the dynamics of the structure.

The frequency domain model for the baseline truss structures well predicted the truss dynamic properties even before the fine tuning to the first mode. There was difficulty in modelling the frequencies of the second truss bending mode. The approximate method based on Rayleigh's Quotient for finding the truss structures natural frequencies and damping was employed using the nominally undamped modeshapes of the all-aluminum truss model. This approximate analysis predicted well the natural frequencies and damping in the baseline truss configurations.

The PMD tuned to the first truss mode produced dramatic increases in modal damping, from 0.6% to 7-8% of critical, with a total system mass increase of only 2.7%. The frequency domain model correlated very well with these results leading to confidence in the ability to represent PMDs as frequency dependant point impedances. The first mode test also proved the efficiency of the PMD as a structural damping device. The experiments with the PMD tuned to the second truss mode also produced dramatic increases in the system second mode damping but with poorer agreement between the analysis and the experiment.

The system response of a structure damped by a PMD was found to be very sensitive to variations of either the frequency or internal damping parameters of the PMD. Since tuning to the structural frequencies predicted *a*

priori by a model does not provide the accuracy necessary to minimize the structural response, some provisions must be made for variable tuning when using these resonant dampers.

The Resonant Shunted Piezoelectrics were also tested for their ability to increase the energy dissipation in the truss over the dissipation found in the shorted piezoelectric case. The RSPs proved very effective in damping the truss, producing a increase in the damping of the first mode to 5.0% of critical with a system mass increase of only 2.0%. This test validated the concept of tuning the resonant electrical part of the RSP to the structural mode to achieve structural damping. The RSP's response to both frequency and damping parameter mistuning was nearly identical to the mistuned PMD. This leads to the need for variable tuning resonant circuits to achieve the minimum structural response.

Tests on the third mode tuning of the RSP demonstrated the importance of the degree to which the piezoelectric materials "participate" in the modeshape to be damped. Low participation leads to low effectiveness for the RSP.

The frequency domain analytical model for the truss and the RSP accurately predicted the shunted piezoelectric effect but with a much higher electromechanical coupling than exhibited by the experiments. This is attributed to inaccuracies in the structural modelling of the piezoelectric truss member rather than to the modelling of the shunted piezoelectric elements.

In all, the experiments preformed demonstrated the usefulness of resonant devices such as the PMD or the RSP for providing damping to a complicated structure. The experiments also illustrated the importance of proper resonance tuning as well as the effects of damper mistuning. This information can prove valuable for the subsequent tuning of resonant dampers.

6.6 Recommendations for Future Work

The results of the previously presented research suggest some possibilities for topics of future research. These topics are in the areas of more accurate frequency domain modelling, further technology development for

shunted piezoelectrics, and the generalization of optimal control strategies to the frequency domain.

The frequency domain framework for system analysis was implemented for only simple masses, stiffnesses, and damping models. There exists the possibility of developing exact frequency domain models for beams or plates which exhibit the behavior of continuous bodies with internal resonances as opposed to discrete masses or stiffnesses. The frequency dependance of the compliances of these elements could be easily incorporated into the frequency domain framework presented in this report.

Another avenue of interest is the further generalization of the frequency domain framework to non-linear systems. This would involve the development of state dependant impedances and the associated analysis techniques, but it could be a powerful tool for the analysis of nonlinear contributions to damping.

The model for shunted piezoelectrics was applied to only two cases, those of resistive and resonant circuit shunting. There could be benefit in using shunting circuits with multiple resonances for simultaneous damping in multiple structural modes. This multimode tuning could present problems with decreased effectiveness for any single mode but would increase the flexibility of the shunted piezoelectric. There is also the possibility of using active shunting circuits to produce shunted piezoelectrics with specially tailored frequency responses.

Finally, the principles of optimal multivariable control can be applied to systems in the frequency domain. Frequency domain optimizations have been presented previously in Ref. [29] as a generalization of time domain optimal control and in Ref. [30] in the area of wave control. The control problem could be formulated with the system represented by the global impedance matrix and the costs associated with the energy dissipation or input to the system using the quadratic forms presented in Section 2.6. In this framework, an optimal feedback impedance matrix from the system velocity vector to the forces could be defined. The constraint of causality must be placed on the problem formulation since the feedback impedance must not be allowed of used future velocity information. This constraint can be difficult to apply in the frequency domain framework. The potential for control of systems with frequency varying properties makes this topic of keen interest.

References

1. Ashley, Holt; Edberg, Donald L., "On the Virtues and Prospects for Passive Damping in Large Space Structures," Presented at the Air Force Vibration Damping Workshop II, April 1985.

2. Sarver, George L., "A Novel Method of Friction Damping for Large Space Structures," S.M. Thesis, Dept. of Aeronautics and Astronautics, MIT, 1982

3. Crawley, Edward F.; Sigler, Jonathan L.; Schoor, Martinius C. von, "Prediction and Measurement of Damping in Hybrid Scaled Space Structure Models," MIT Space Systems Laboratory Report No. 7-88, July 1988

4. Chen, Gun-Shing; Wada, Ben K., "Passive Damping for Space Truss Structures," 29th AIAA/ASME/ASCE/AHS Structures Structural Dynamics and Materials Conference, May 1988, AIAA Paper 88-2469

5. Miller, David W.; Crawley, Edward F., "Developmnet of Finite Active Control Elements for Large Flexible Space Structures," MIT Space Systems Laboratory Report No. 6-85, June 1985

6. Penfield, Paul Jr.; Spence, Robert; and Buinker, Simon, *Tellegen's Theorem and Electrical Networks*, Research Monograph No. 58, MIT Press, Cambridge, Mass., 1970

7. Cannon, Robert H., *Dynamics of Physical Systems*, McGraw-Hill, New York, NY, 1967, pp. 32

8. Church, Austin H., *Mechanical Vibrations*, Second Edition, John Wiley & Sons, New York, NY, 1963, pp. 187-218

9. Paynter, Henry Martin, *Analysis and Design of Engineering Systems*, MIT Press, Cambridge, Mass.,1961

10. Crandall, Stephen H.; Dahl, Norman C.; Lardner, Thomas J., *An Introduction to the Mechanics of Solids*, Second Edition, McGraw-Hill, New York, NY., 1978, pp. 72-119

11. Penfield, P., *Frequency-power Formulas*, Technology Press of MIT, Cambridge, Mass., 1960

12. Ewins, D.J., *Modal Testing: Theory and Practice* , John Wiley & Sons, New York, NY, 1986, pp. 27

13. Clough, R. W.; Penzien, J., *Dynamics of Structures*, McGraw Hill, New York, NY, 1975

14. Anderson, Melvin S., "Vibration of Prestressed Periodic Lattice Structures," *AIAA Journal*, Vol. 20, No. 4, April 1982, pp. 551-555

15. Wittrick, W. H., Williams, F.W., "A General Algorithm for Computing Natural Frequencies of Elastic Structures," *J. Mechanics and Applied Math*, Vol. XXIV, Pt. 3, 1971, pp. 263-284

16. Rayleigh, J. W. S., *Theory of Sound*, Vol 1, Dover, New York, 1945, p. 119

17. Nasif, Ahid D.; Jones, David I. G.; Henderson, John P., *Vibration Damping*, John Wiley & Sons, New York, 1985, pp.69-73

18. Timoshenko, Stephen; Young, D.H.; Weaver, W., Jr., *Vibration Problems in Engineering*, 4th Ed., John Wiley and Sons, New York, 1974.

19. Hartog, J. P. Den, Mechanical Vibrations, Fourth Edition, McGraw-Hill, New York, 1956, pp. 93-106

20. Juang, J., "Optimal Design of a Passive Vibration Absorber for a Truss Beam," *J. Guidance, Control, and Dynamics*, Nov. - Dec. 1984, p. 733

21. Jaffe, B.; Cook, R.; Jaffe, H., *Piezoelectric Ceramics*, Academic Press, New York, NY., 1971

22. Edwards, R. H., Miyakawa, R. H., *Large Structure Damping Task Report*, Hughes Aircraft Co. Report No. 4132.22/1408, May 1980

23. "Components Catalogue Construction M12," MERO-Raumstruktur GMBH & Co., Wuerzburg, P.O. Box 6169 D-8700 Wurzburg 1, 1985

24. Mills, Raymond A., "Natural Vibrations of Beam-Like Trusses," S.M. Thesis, Dept. of Aeronautics and Astronautics, MIT, June 1985.

25. Purcell, Edward M., *Electricity and Magnetism,* Berkeley Physics Course, Vol. 2, McGraw-Hill, New York, 1965. pp 184

26. Zimmerman, David C.; Inman, Daniel J.; Horner, Garnett C., "Dynamic Characterization and Microprocessor Control of the NASA/UVA Proof Mass Actuator," 25th AIAA/ASME/ASCE/AHS Structures Structural Dynamics and Materials Conference, May 1984, AIAA Paper 84-1077, pp. 573-577

27. Slemon, Gordon R., *Magnetoelectric Devices: Transducers, Transformers, and Machines,* John Wiley & Sons, New York, 1966

28. Lee, Daniel T.L.; Morf, Martin; Friedlander, Benjamin, "Recursive Least Squares Ladder Estimation Algorithms" IEEE Transactions on Acoustics, Speech and Signal Processing, Vol. ASSP 29, No. 3, June 1981, pp. 627-641

29. Gupta, N. K., "Frequency-Shaped Cost Functionals: Extensions of Linear-Quadratic-Gaussian Design Methods," *J. Guidance and Control,* Vol. 3, No. 6, Nov.-Dec. 1980, pp. 529-535

30. Miller, David W.; Flotow, Andreas von; and Hall, Stephen R., "Active Modification of Wave Reflection and Transmission in Flexible Structures," Proceedings American Control Conference, Vol. 2, June 1987, pp. 1318-1324

Appendix A
Implementation of Frequency Domain Analysis

A.1 Overview

The frequency domain analysis techniques for structural systems presented in Chapter 2 can be implemented numerically on a digital computer. In this appendix, some aspects of that implementation will be discussed. The general technique used to represent frequency dependant materials will be discussed as well as the actual implementation of the techniques for finding approximate and exact model frequencies and damping.

The implementations of the formulae presented for calculating the approximate or exact model frequencies and damping were used to provide the comparison with the data from the experimental truss structure. An understanding of the techniques used to derive these comparisons is necessary for interpreting the validity of the analytical results.

A.2 Program Organization

A computer program was written in Fortran to model structures using the frequency dependant impedances of the elements. In form, the program resembles a conventional finite element program. The impedance matrices of the elements are evaluated at a certain frequency, rotated into the global coordinate frame and assembled into a global impedance matrix just as are the element stiffness matrices in conventional finite element programs. The restrained degrees of freedom are then eliminated and the global impedance matrix is reduced to contain only the retained set of degrees of freedom (DOF) using static condensation. The velocities at the retained DOF can then be solved for by inverting the reduced impedance matrix and solving for the velocities which result from a given forcing vector using linear algebra.

This process is essentially identical to static displacement solutions using finite element procedures with the exception that the element

stiffnesses are replaced by the element impedances evaluated at a single frequency. The result is the system response for the retained DOF set at a single frequency. The system responses as a function of frequency are created by looping through the above solution procedure for multiple frequencies within the desired range of the frequency response. The repetitive assembly, reduction and inversion of the global impedance matrix can be quite time consuming for large order systems. The analytical transfer functions presented in Chapter 5 were calculated in this manner.

A.3 Algorithms for Approximate Frequencies and Damping

There are several difficulties associated with the implementation of the approximate formula for frequencies and damping presented in Equations 2.45 and 2.50 respectively. These problems stem from the fact that the matrices used in the approximate formula for frequencies and damping are themselves dependant on the frequencies at which they are evaluated. This creates a problem in the choice of the appropriate frequencies at which to evaluate the approximate stiffness and mass matrices derived from Equations 2.48a and b.

In the computer implementation of the approximate formulae, this problem was overcome by using successively more accurate estimates of the frequencies. The algorithm for determining the approximate estimates follows the following steps:

1) The initial estimate for the natural frequency of the system is found by visual inspection of the analytical transfer function derived in the manner described in Section A.2. The transfer function can be computed over a broad frequency range and visually inspected for local maxima which may correspond to the structural mode for which an estimate of the natural frequency or loss factor is desired.
2) The initial estimate for the natural frequency is used to form the imaginary part (real part remains zero) of an initial estimate of the Laplace parameter, s. This Laplace parameter is in turn used in the calculation of the global impedance matrix (GIM).
3) The initial estimate for the frequency is also used to form the real part (imaginary part remains zero) of the Laplace parameter which is used

in the calculation of the second impedance matrix needed for Equation 2.48 (The first is evaluated at $i\omega$ while the second is evaluated at ω).

4) These two impedance matrices are used in Equation 2.48 a & b to calculate a first guess at the approximate global stiffness and mass matrices.
5) These stiffness and mass matrices are used along with an assumed approximate modeshape in Rayleigh's Quotient [Equation (2.45)] to create a more accurate estimate of the modal natural frequency. In the implementation for the truss experiment, the vector of nodal velocities for the all aluminum truss which resulted from forcing at node 1 was used for the assumed modeshape. This vector was calculated at the frequencies found from Step 1 above for the 3 bending modes.
6) This more accurate estimate of the frequency is used in another calculation of the global impedance matrix which is then used in Equation 2.50 for the calculation of the modal loss factor.
7) These final estimates of the modal loss factor and frequency can then be used to compute the approximate pole locations. The approximate pole locations are used as an initial guess for the exact pole search.

This procedure was used in the calculation of the approximate natural frequencies and damping ratios presented along with the experimental data in Chapter 5. Since it required only three executions of the assembly and reduction loop for the GIM, it is a less time intensive method of finding the system poles than the numerical search for the zero of the determinant of the GIM used in determining the exact pole locations.

A.4 Algorithm for Determining the Exact Model Pole Locations

The exact model pole locations correspond to values of the Laplace parameter,s, for which the determinant of the global impedance matrix is equal to zero. This is expressed in Equation 2.43. As described in Section A.2 the impedance matrix can be evaluated for any given value of s. The determinant at that value of s can also be calculated from the GIM. The technique used to find that value of the Laplace parameter which zeros the determinant involves a numerical search over the complex plane.

The determinant of the GIM possesses several properties which make this numerical search difficult. First, the determinant is a complex quantity. It has real and imaginary parts which must both be identically zero at a system pole. The determinant can be though of as a complex valued function over the complex plane. The numerical search can be simplified by dealing with only the magnitude of the determinant in the zero search since the magnitude of the determinant will only equal zero if both the real and imaginary parts of the determinant are equal to zero. Secondly, the complicated nature of the elemental impedances, which can contain transcendental functions of s, leads to highly nonlinear behavior for the determinant function. The determinant can exhibit abrupt changes and other phenomena which can seriously impede a numerical search. Finally, for large systems, the determinant of the GIM can be quite large at higher frequencies. Numerical problems can arise due to limitations of the size of numbers representable by the computer. For the truss structure model, the determinant overflowed the limitations placed in Fortran for double precision representations of real numbers at only 20 Hertz. Within this array of large numbers the poles appear as extremely sharp spikes to zero, further confounding the search algorithm.

The problems of size where overcome by converting the search for the zero of the determinant into a search over the natural log of the magnitude of the determinant. This made the problem more amenable to traditional numerical search routines. The problem of finding a zero of a complex valued function was thus converted to one of finding a minimum of a real valued function with two variables: the real and imaginary part of the assumed pole locations.

This two dimension search for a minimum can be implemented in a variety of ways. For the calculation of the exact pole locations presented in Chapter 5, a simple gradient search in two dimensions was preformed using as an initial estimate the pole location derived from the approximate formulae described in Section A.3. While probably not the most computationally efficient algorithm for finding minima in two dimensions, it preformed satisfactorily for the relatively simple truss model.